Supplementary Information

Synergistic versatile bistriflimide salts in light-accelerated spiro-OMeTAD oxidation and perovskite module photovoltaics engineering

Jiahao Zhang[1], Xiaomin Liu[2], Haifei Wang[2], Penghui Ji[1], Shuai Yuan[1,3], Hengyuan Wang[1,4], Ting Guo[1,5], Silvia Mariotti[1], Ilhem Nadia Rabehi[1], Xiaomin Huo[1,6], Tianhao Wu[1,7], Congyang Zhang[1,8], Chenfeng Ding[1], Liliia Moshniaha[9], Kirill Mitrofanov[9], Dominik Madea[9], Ryota Kabe[9], Dandan Song[6], Zheng Xu[6], Zhuangzhi Wu[5], Yun Li[4], Yixin Zhao[2], Tongle Bu[10], Guoqing Tong*[,11], Luis K. Ono*[,1], Yabing Qi*[,1,12,13]

*Corresponding authors: Guoqing Tong. E-mail: guoqing.tong@hfut.edu.cn; Luis K. Ono, E-mail: katsuya.ono@oist.jp; Yabing Qi, E-mail: yabingqi@sjtu.edu.cn

The PDF file includes:

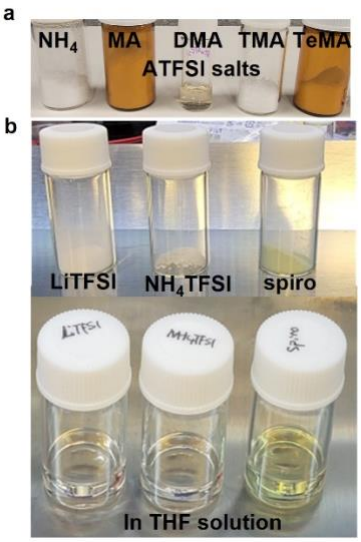

Supplementary Fig. 1. Photos of the synthesized ATFSI salts and their solutions in THF.

a As-synthesized ATFSI salts. NH_4TFSI, MATFSI, and TMATFSI are white solids, whereas DMATFSI appears as an ionic liquid. **b** Solutions after dissolving LiTFSI, NH_4TFSI and spiro-OMeTAD in THF.

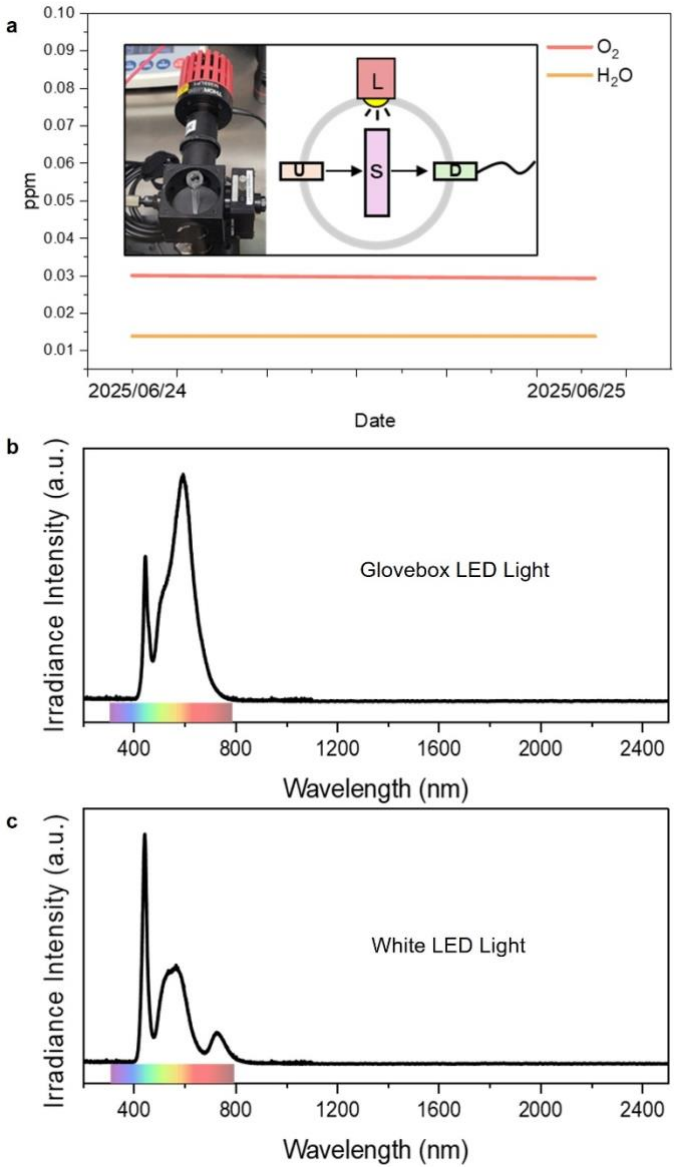

Supplementary Fig. 2. Setup and operating conditions for *in situ* ultraviolet-visible-near-infrared (UV-Vis-NIR) absorption measurements. a, Variation of H_2O and O_2 concentrations inside the glovebox (< 0.1 ppm). The inset shows the custom-built *in situ* UV-Vis-NIR measurement setup, where U is the spectrometer's light source with bandpass filter, D is the detector, S is the sample, and L is the external, variable-wavelength LED for sample illumination. **b,** Full-range emission spectrum of the LED lights used for general illumination within the glovebox. **c,** Emission spectrum of the white LED lights used for the LODT tests.

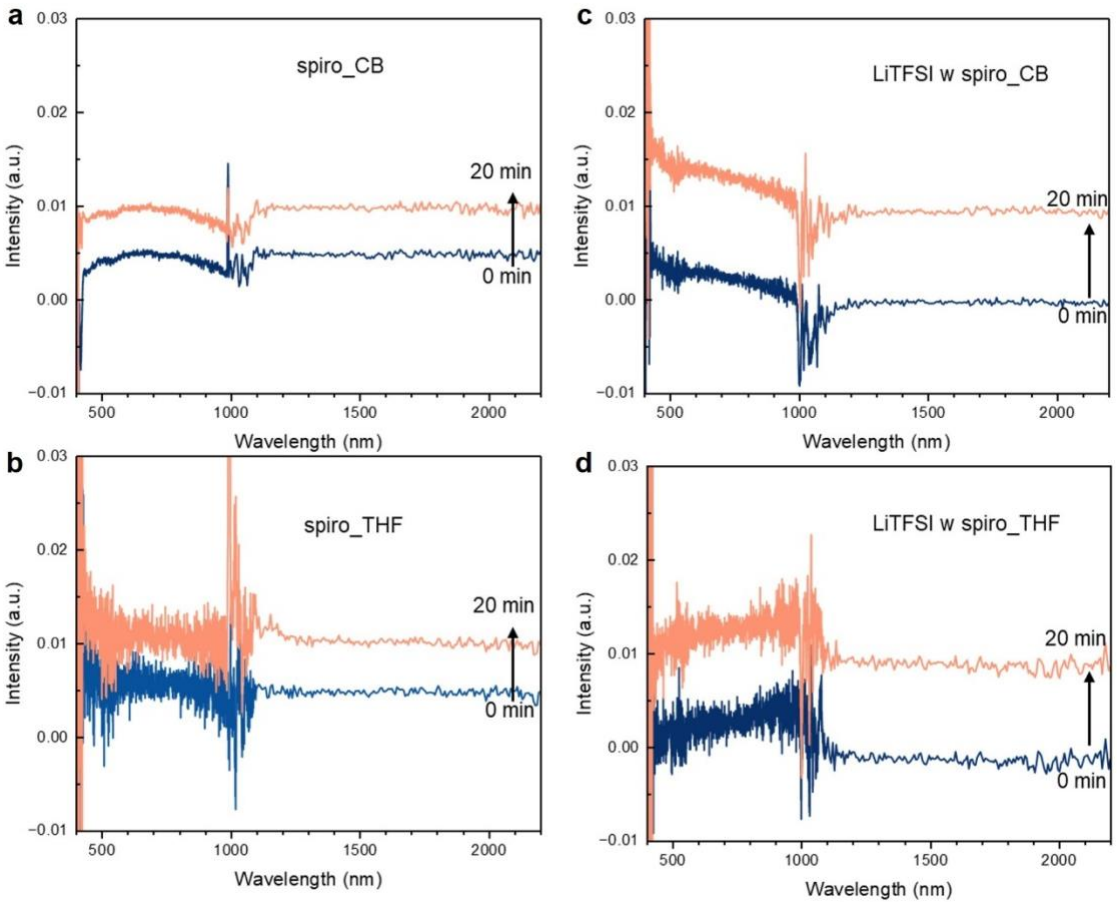

Supplementary Fig. 3. UV-Vis-NIR absorption of pristine spiro-OMeTAD and spiro-OMeTAD doped with LiTFSI. The absorption spectra for pristine spiro-OMeTAD solutions using **a,** chlorobenzene (CB) and **b,** THF as the solvent, respectively; spiro-OMeTAD with LiTFSI in **c,** CB and **d,** THF under white LED illumination for 20 min.

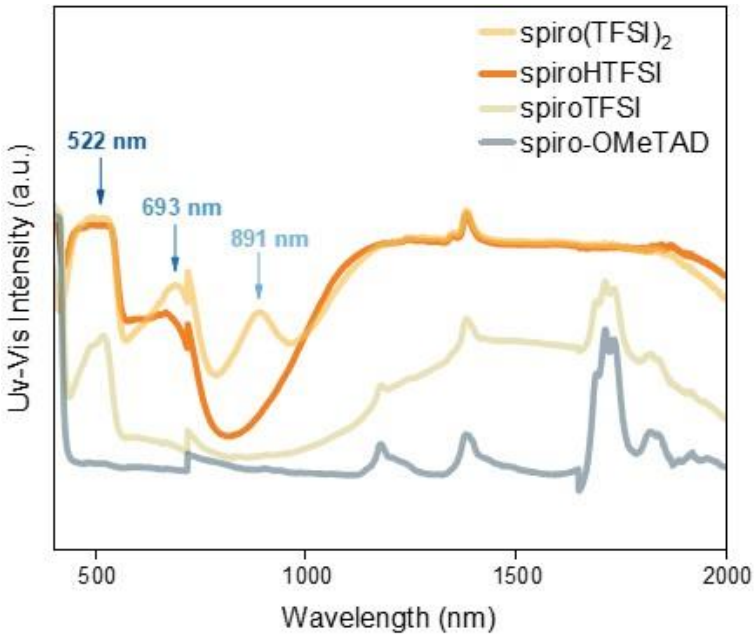

Supplementary Fig. 4. UV-Vis-NIR absorption spectra of different oxidized spiro species solutions. Probing of different oxidized spiro species in pristine spiro-OMeTAD, spiroHTFSI, spiroTFSI and spiro(TFSI)2. The sharp peaks are due to the switching of different light sources from instrument during tests.

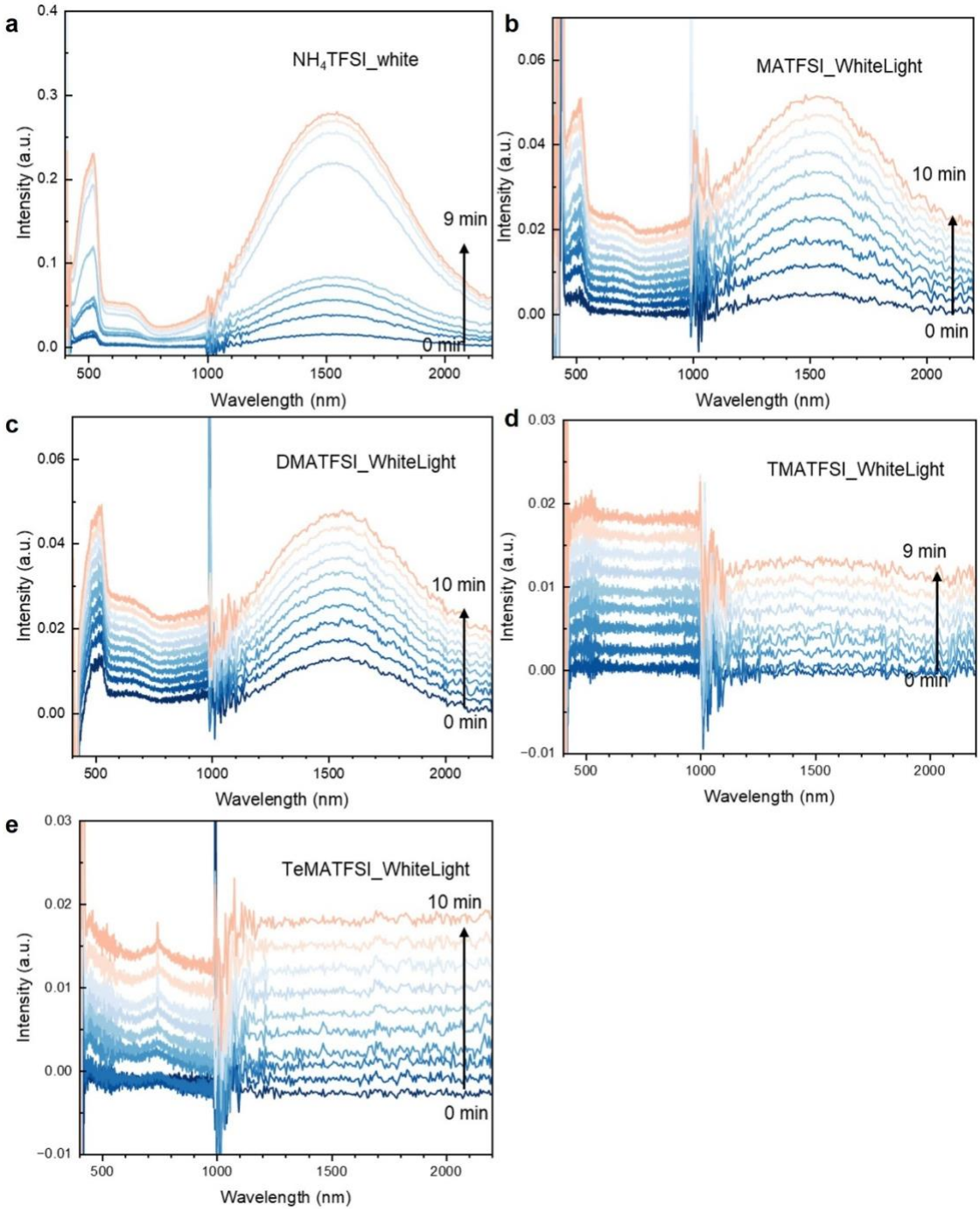

Supplementary Fig. 5. Photoresponsivity absorption of spiro-OMeTAD solutions doped with various ATFSI salts. Time-resolved UV-Vis-NIR absorption spectra of spiro-OMeTAD solutions doped with **a,** NH_4TFSI, **b,** MATFSI, **c,** DMATFSI, **d,** TMATFSI, and **e,** TeMATFSI, measured under continuous white LED illumination for 10 min. The sharp spikes are due to the switching of different light sources in the measurement setup during the test.

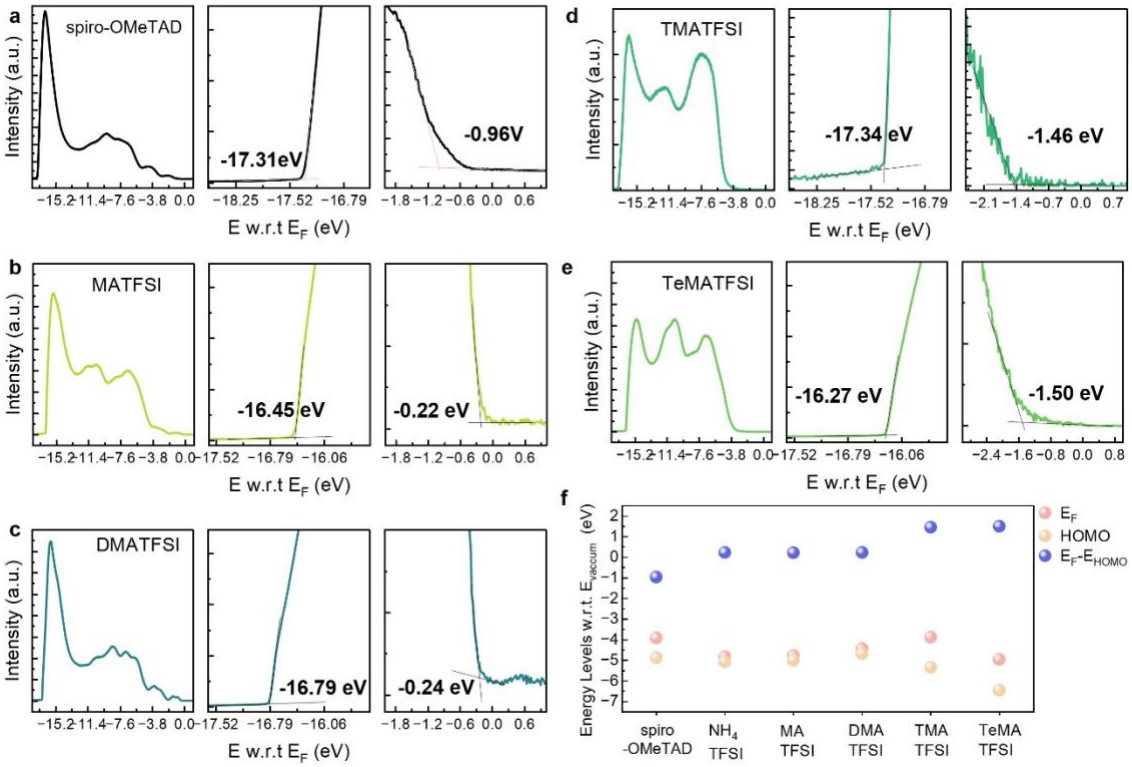

Supplementary Fig. 6. UPS results of the LODT-HTL films doped with ATFSI salts. **a-e,** Ultraviolet photoemission spectroscopy (UPS) spectra for the LODT-HTL films doped with **a,** NH_4TFSI, **b,** MATFSI, **c,** DMATFSI, **d,** TMATFSI, and **e,** TeMATFSI. **f,** Summary plot of the energy positions of the corresponding Fermi level (E_F), the highest occupied molecular orbital (E_{HOMO}), and the energy difference between them (E_F-E_{HOMO}) as extracted from the UPS data. More information can be found from **Supplementary Table 1.**

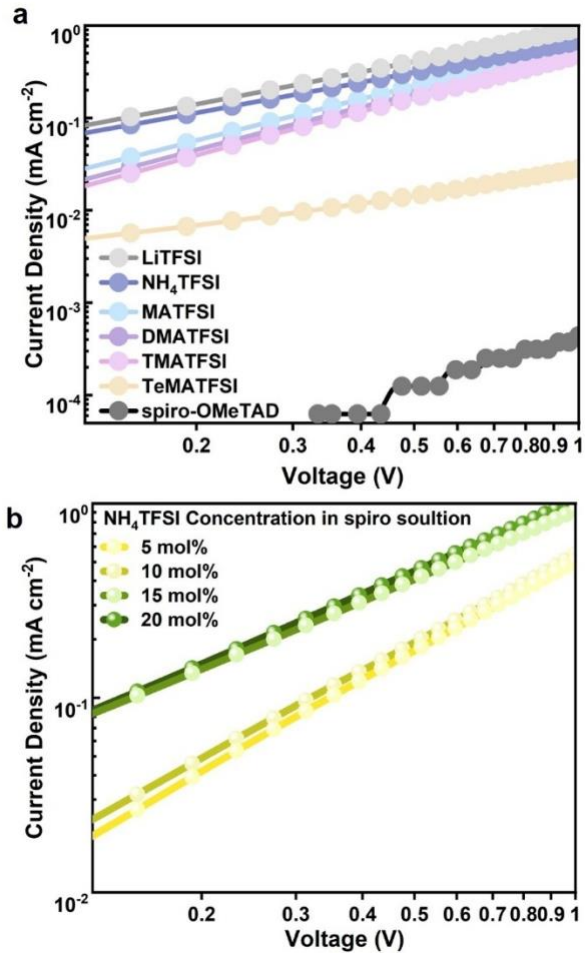

Supplementary Fig. 7. Conductivity of the different LODT-spiro HTL. Dark current density as a function of applied voltage. The device structure is ITO / LODT spiro with different TFSI salts / Au. The relative vertical position of the curves directly reflects the conductivity differences as a function of **a,** different cations and **b,** NH_4TFSI concentration.

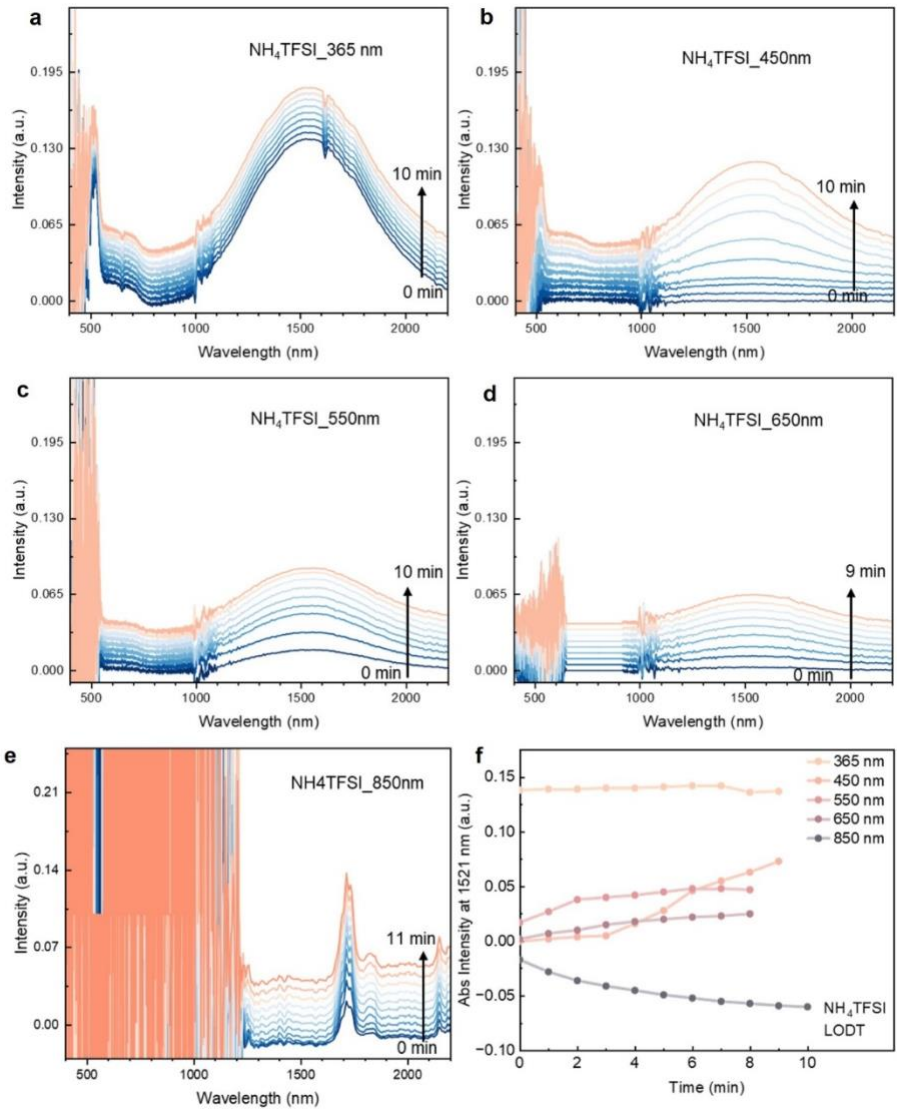

Supplementary Fig. 8. UV-Vis-NIR spectra of the NH_4TFSI-doped spiro-OMeTAD solution under illumination at different wavelengths. Evolution of the absorption spectra for an NH_4TFSI-doped spiro-OMeTAD solution in THF under monochromatic LED light source illumination. The illumination wavelengths for the respective panels correspond to **a,** 365 nm, **b,** 450 nm, **c,** 550 nm, **d,** 650 nm, and **e,** 850 nm. **f,** Absorbance intensity changes at 1521 nm under different light illumination. The sharp peak around 1700 nm in (**e**) can be attributed to the two low-lying transitions of $spiro^{+}$.[1]

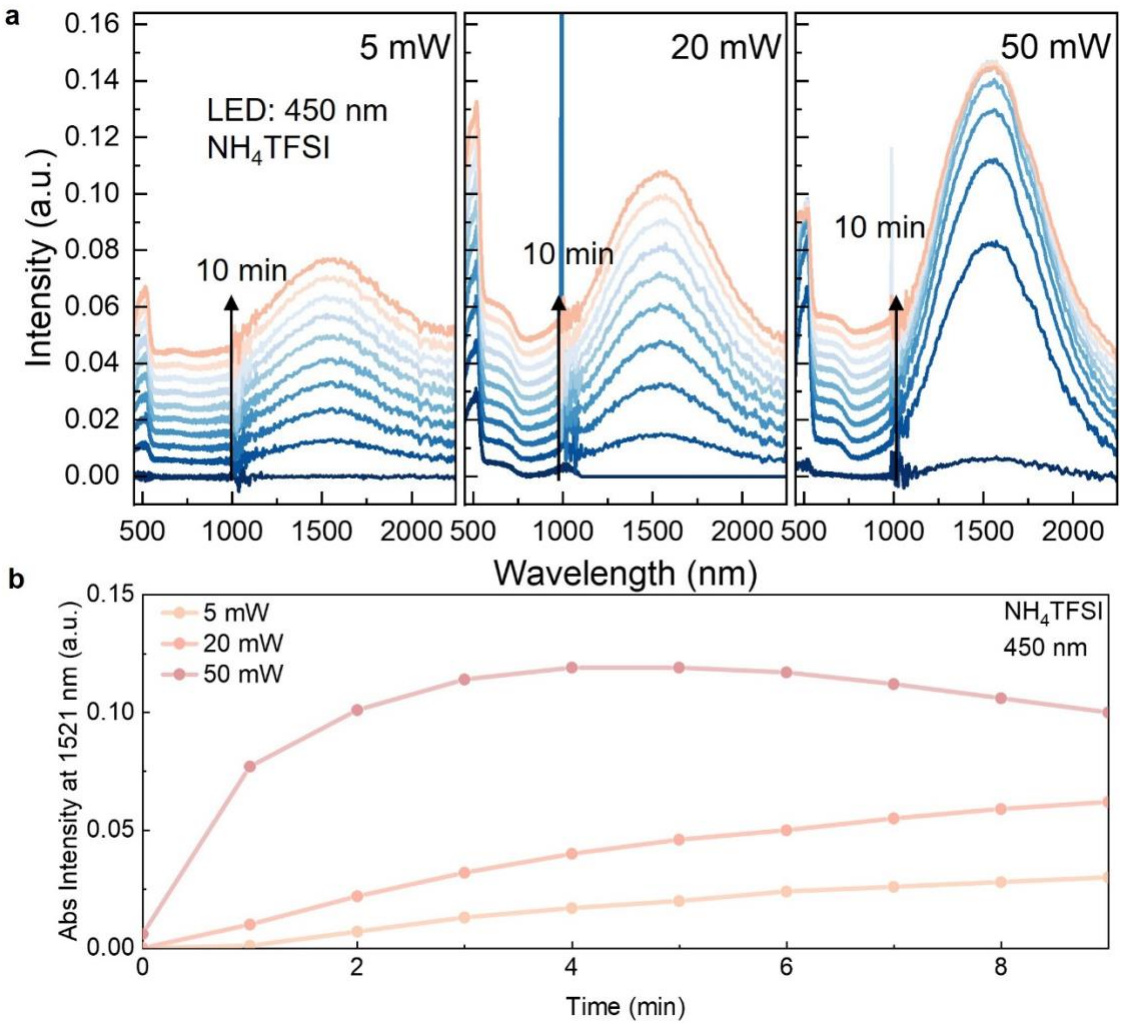

Supplementary Fig. 9. Light intensity dependence of the LODT NH_4TFSI-doped spiro-OMeTAD. a, Absorbance changes of the NH_4TFSI-doped spiro-OMeTAD solution over the same time period under illumination with a 450 nm LED at various power levels (5 mW, 20 mW and 50 mW) in 10 min. **b,** Absorbance intensity changes at 1521 nm by 450 nm light illumination at different light power values.

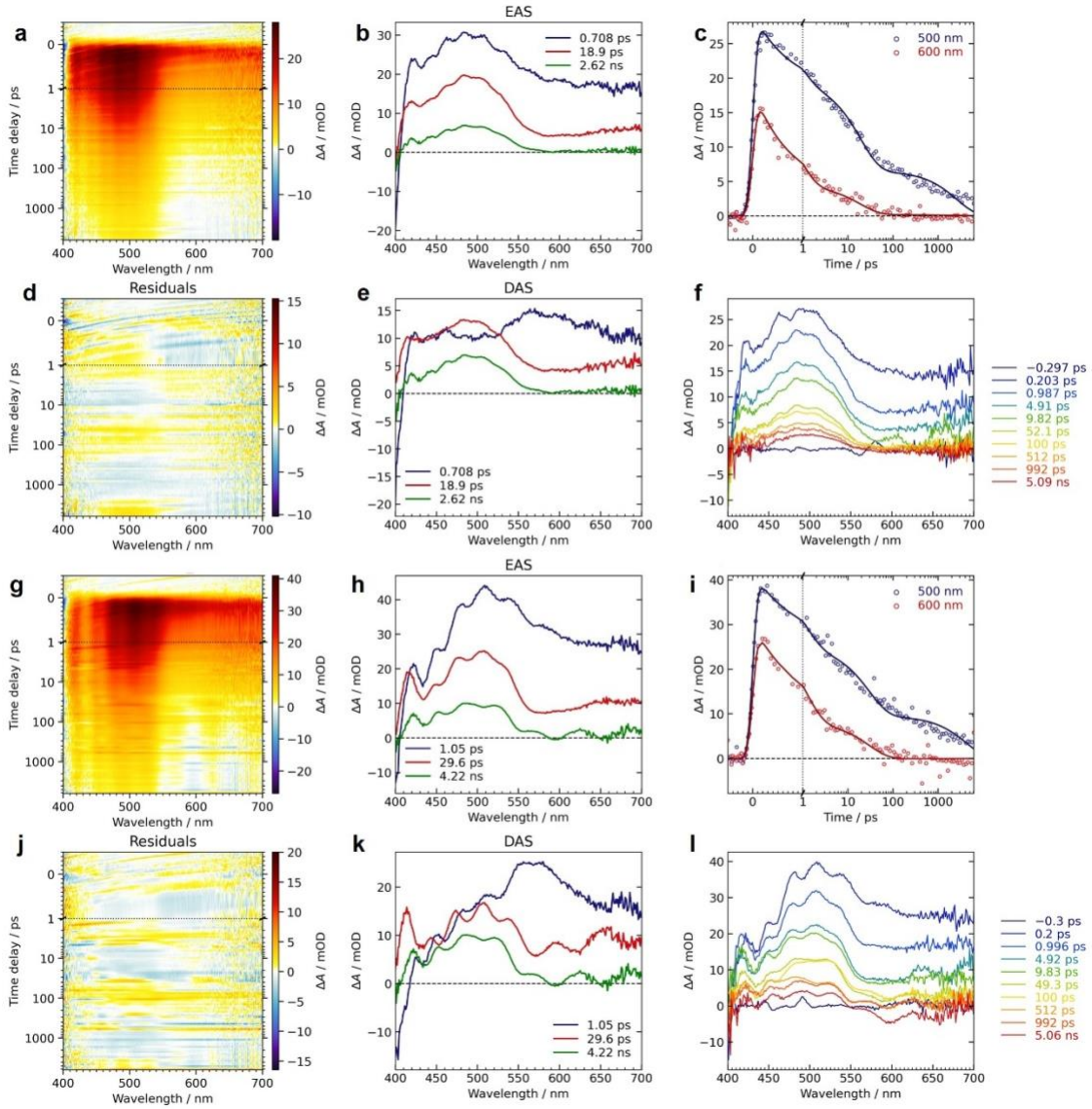

Supplementary Fig. 10. Pump-probe transient absorption spectroscopy (TAS) of pristine and NH_4TFSI-doped spiro-HTL. Comprehensive TA data and global analysis for a pristine spiro-OMeTAD film (**a-f,**) and an NH_4TFSI-doped LODT-HTL film (**g-l,**), following excitation with a 350 nm pump pulse. **a, g,** Chirp-corrected transient absorption data displayed as contour plots. **b, h,** Evolution-associated spectra (EAS). **c, i,** Experimental (circles) and fitted (solid lines) kinetic traces at representative wavelengths. **d, j,** Residual matrix from the global fit. **e, k,** Decay-associated spectra (DAS). **f, l,** Transient absorption spectra at the selected time delays.

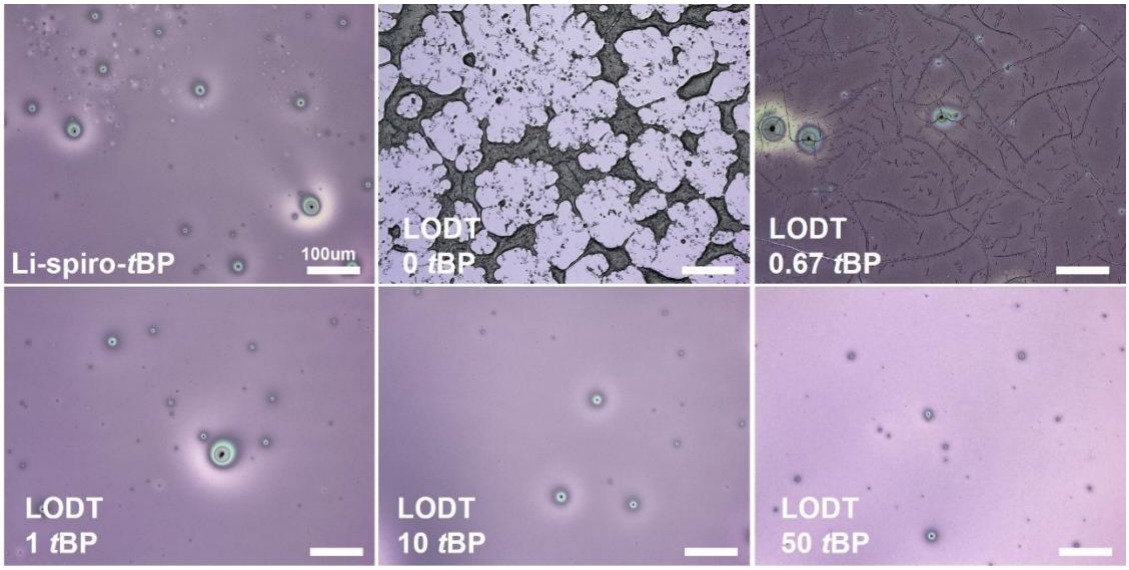

Supplementary Fig. 11. Effect of the *t*BP/THF volume ratio on the film morphology of LODT-HTLs. Optical microscopy images of conventional LiTFSI-doped spiro-HTL and NH_4TFSI-doped LODT-HTL films prepared with varying volume ratios of *t*BP:THF. All scale bars correspond to 100 μm.

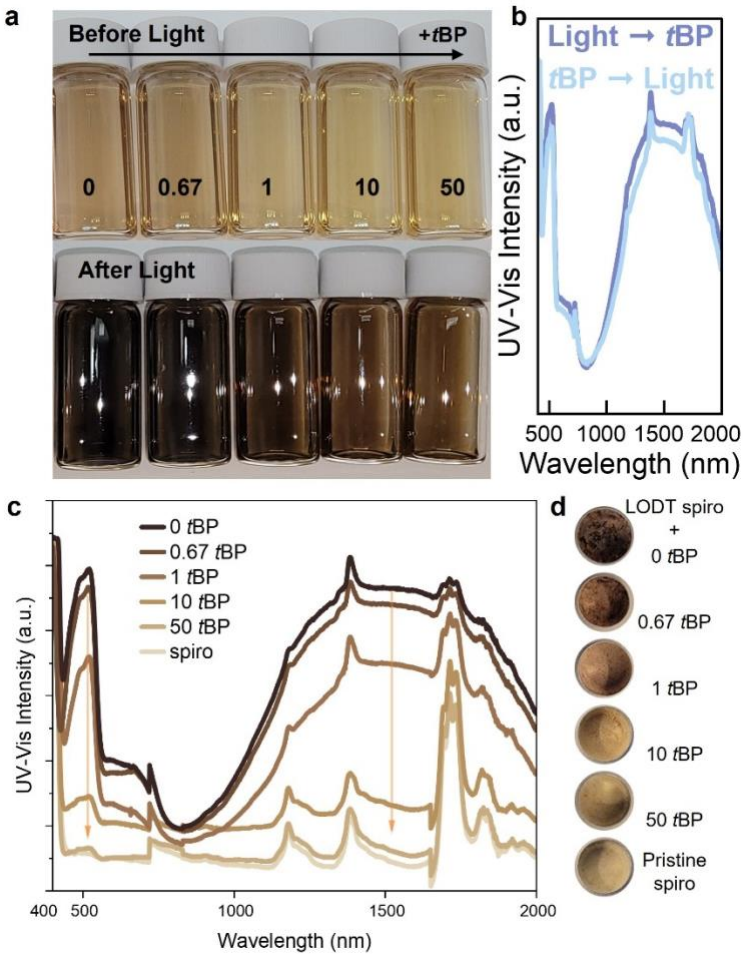

Supplementary Fig. 12. Effect of *t*BP addition on the optical properties of LODT solutions. a, Photos of the spiro solutions prepared with varying amounts of *t*BP added before and after being illuminated with white light. **b,** Comparison of the final solution absorbance resulting from two different process sequences: adding *t*BP before light exposure and adding *t*BP after light exposure. **c,** Corresponding UV-Vis-NIR absorption spectra for the solutions shown in **a. d,** Photos of the solid materials that remained after solvent evaporation. NH_4TFSI was employed as dopants for all LODT-HTL solutions.

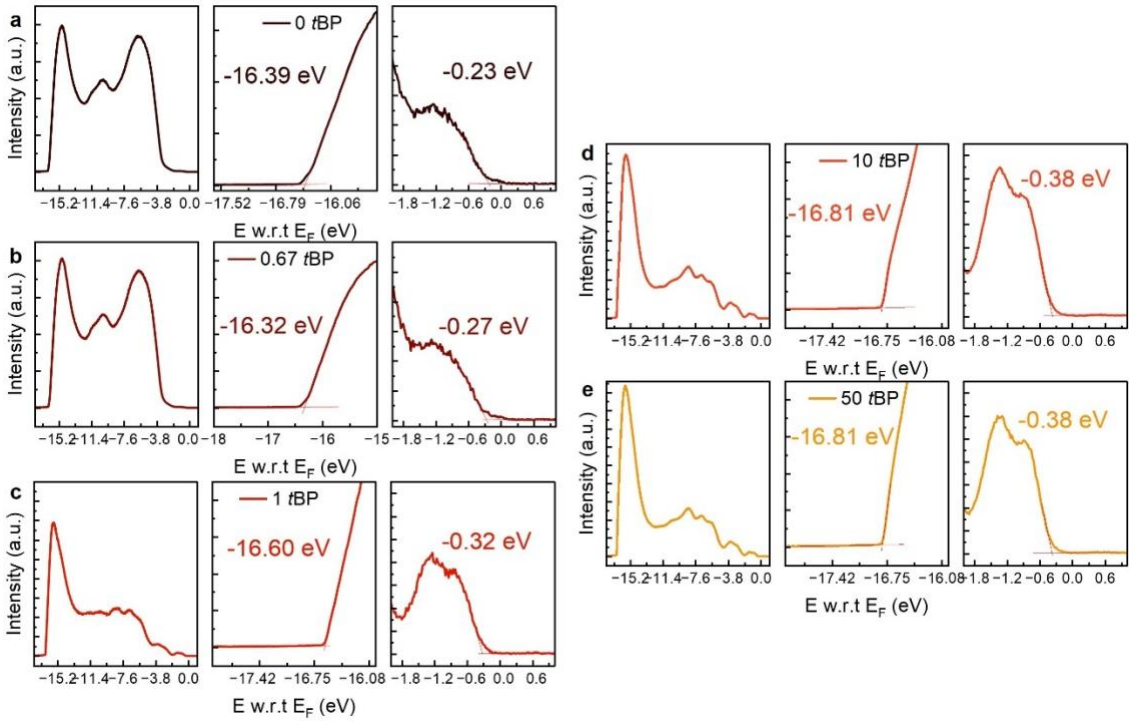

Supplementary Fig. 13. Effect of the *t*BP concentration on the energy levels of the LODT-HTL films, studied by UPS. UPS spectra of the NH_4TFSI-doped LODT-HTL films prepared with varying volume ratios of *t*BP to THF. The *t*BP/THF ratios for the respective panels are: **a,** 0, **b,** 0.67, **c,** 1, **d,** 10, and **e,** 50. More information can be found in **Supplementary Table 2.**

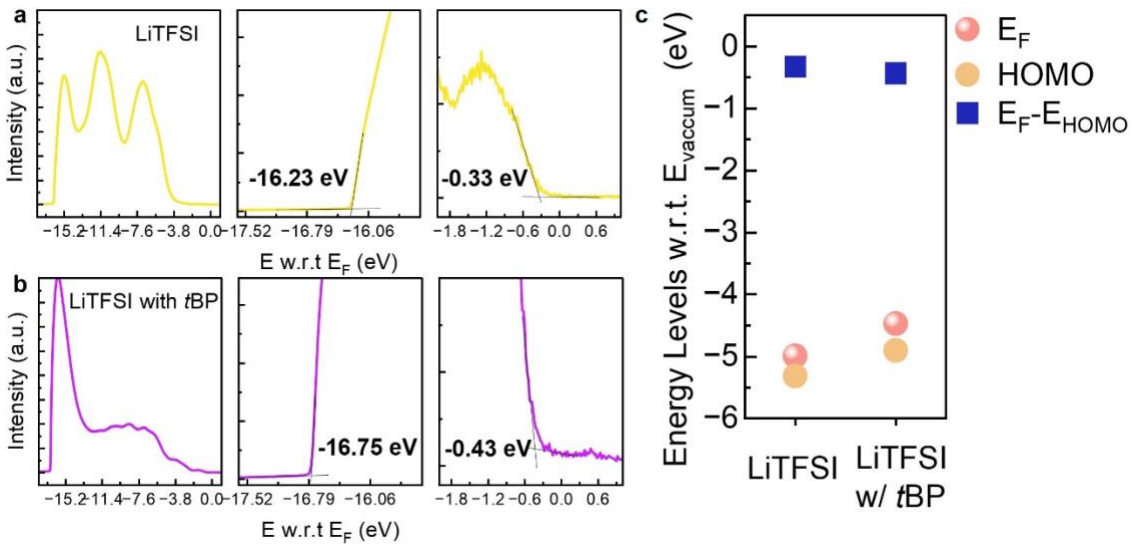

Supplementary Fig. 14. Effect of *t*BP on the energy levels of conventionally LiTFSI-doped spiro-HTL films. a, b, UPS spectra of the LiTFSI-doped spiro-HTL films prepared **a,** without and **b,** with the addition of *t*BP in THF solvent. **c,** Summary and comparison of the corresponding E_F, HOMO position, and their energy differences ($|E_F - E_{HOMO}|$).

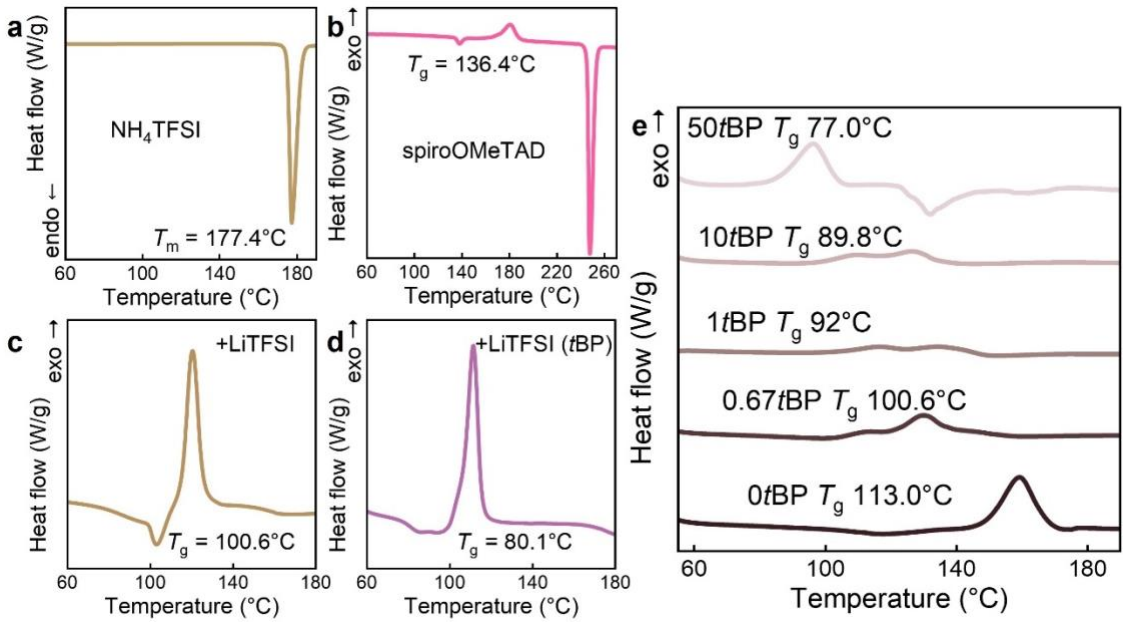

Supplementary Fig. 15. Determination of glass transition temperature (T_g) by differential scanning calorimetry (DSC). a-d, DSC for **a,** pure NH_4TFSI, **b,** pristine spiro-OMeTAD, **c,** spiro-OMeTAD doped with LiTFSI, and **d,** spiro-OMeTAD doped with both LiTFSI and *t*BP in conventional HTL. **e,** DSC showing the changes in T_g for the NH_4TFSI-doped LODT-HTL as a function of *t*BP concentration.

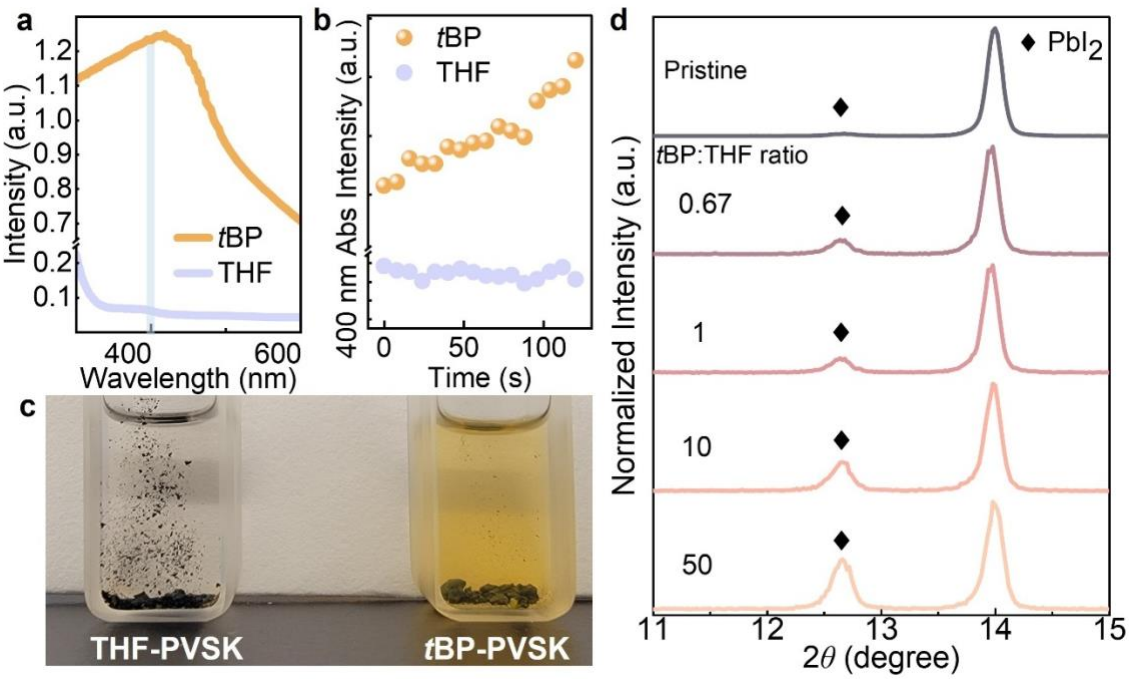

Supplementary Fig. 16. Stability test of the $FAPbI_3$ single crystals in THF and *t*BP solvents. a, UV-Vis spectra of $FAPbI_3$ single crystals immersed in *t*BP and THF. **b,** Time-resolved absorbance for monitoring the dissolution kinetics of $FAPbI_3$ in the two solvents. **c,** Photos of dissolved $FAPbI_3$ in THF and *t*BP. **d,** XRD patterns of the perovskite films after treatment with different concentrations of *t*BP, showing the emergence of the PbI_2 degradation peak ($2\theta = 12.6°$) with respect to the main perovskite peak ($2\theta = 14.1°$).

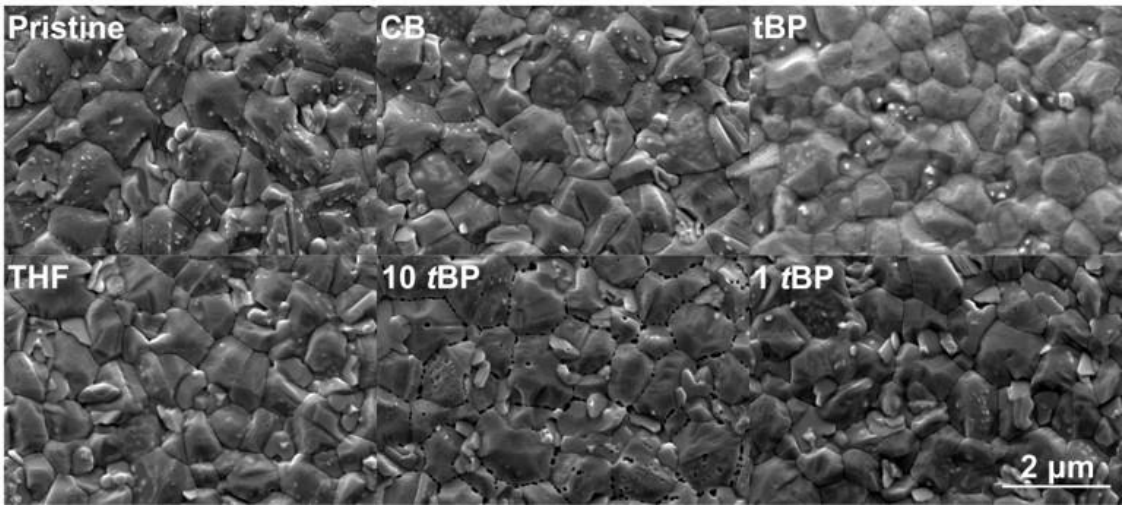

Supplementary Fig. 17. Effect of solvent treatment on the surface morphology of the perovskite films. Top-view SEM images of the perovskite films after being treated with different solvents. All images have the same size, and the scale bar is 2 μm.

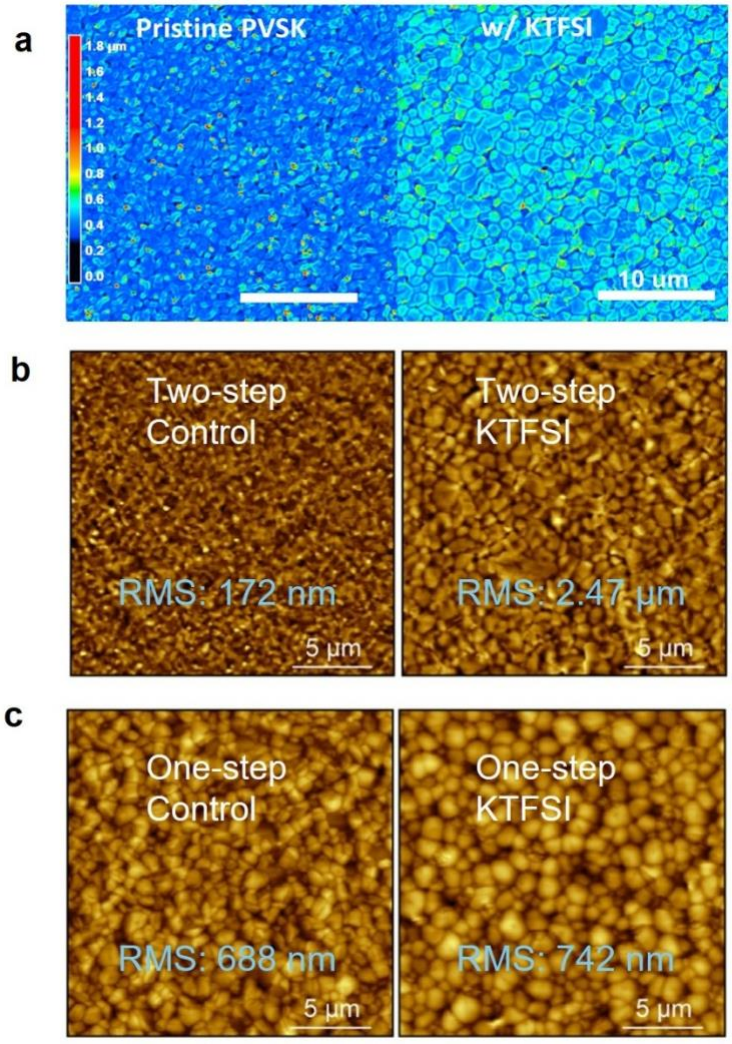

Supplementary Fig. 18. Effect of KTFSI additive on the morphology of perovskite films. a, 3D pseudo-color image from laser scanning microscopy, showing the surface topography of a KTFSI-doped perovskite film prepared *via* the two-step method. **b,** AFM images comparing the pristine (control) and KTFSI-treated perovskite films prepared *via* the two-step method. The root-mean-square (RMS) roughness is 172 nm for the control sample and 2.47 µm for the treated film. **c,** AFM images comparing pristine (control) and KTFSI-treated perovskite films prepared *via* the one-step anti-solvent method. The addition of KTFSI increases the mean grain size from 688 nm for the control sample to 742 nm for the treated film.

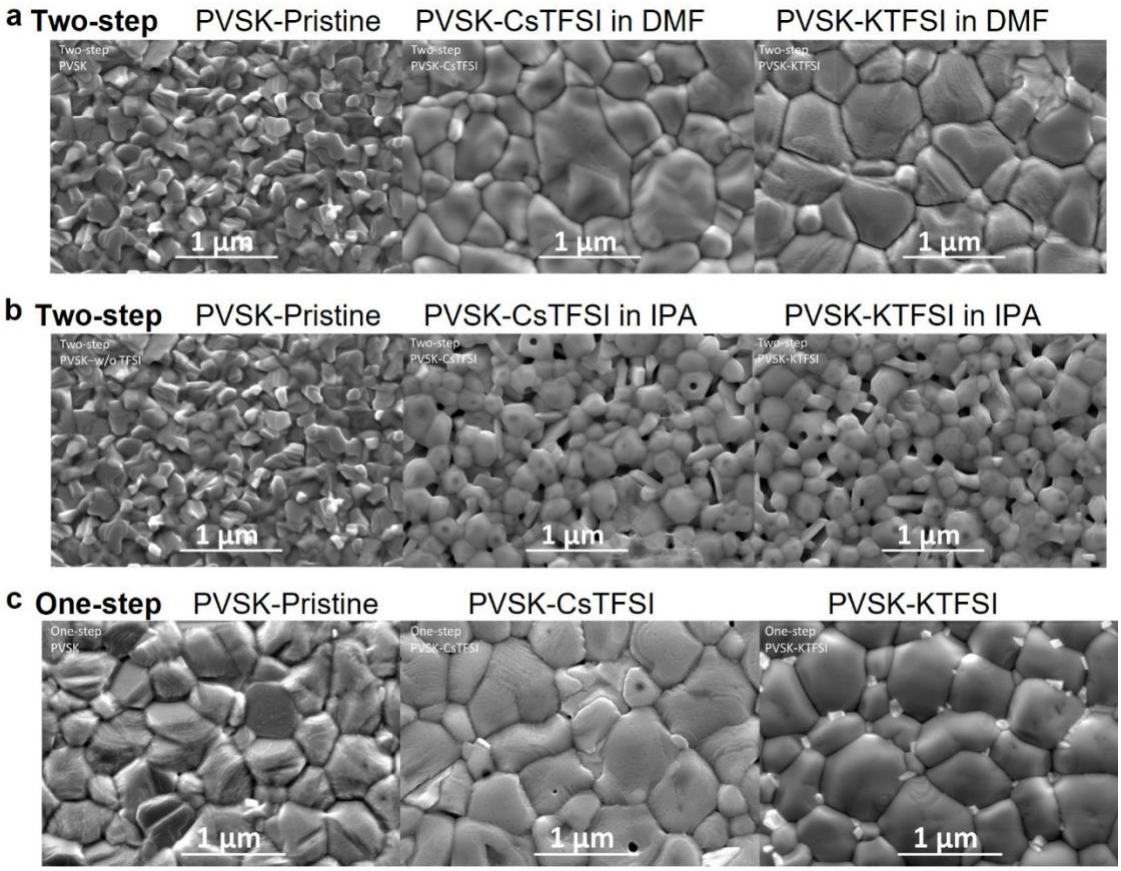

Supplementary Fig. 19. SEM images of the perovskite films doped with TFSI salts. SEM images of the perovskite films prepared with either KTFSI or CsTFSI additives introduced at different stages of the fabrication process. Each row compares a pristine film, a CsTFSI-doped film, and a KTFSI-doped film. **a,** For the two-step method, with the TFSI salt added to the PbI_2 precursor solution. **b,** For the two-step method, with the TFSI salt added to the FAI/IPA solution. **c,** For the one-step method, with the TFSI salt added to the perovskite precursor solution.

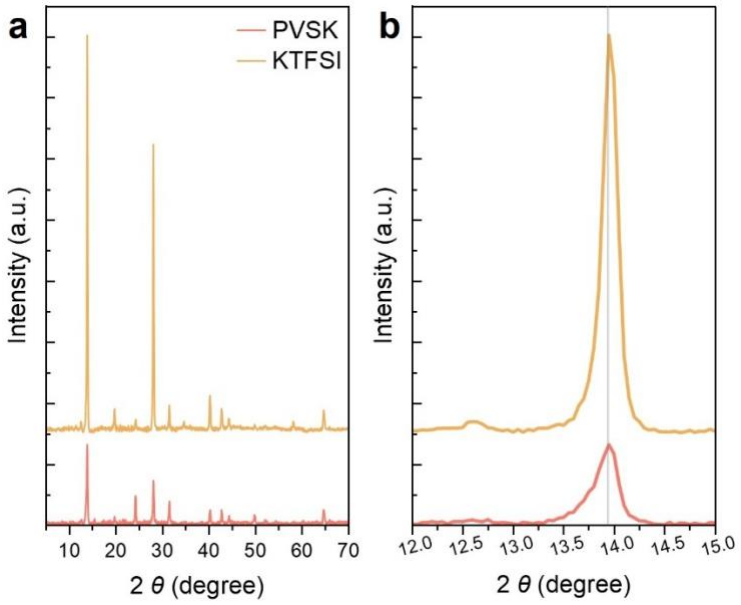

Supplementary Fig. 20. XRD results of the effect of KTFSI on the two-step processed perovskite films. Comparison of the XRD patterns for the pristine (control) and KTFSI-doped perovskite films. **a,** Wide-angle scan over the 2-theta range of 2θ = 5-70°. **b,** Zoomed-in view of the 2θ = 12-15° region, highlighting the main PbI_2 (001) peak (2θ ~ 12.6°) and the perovskite (110) peak (2θ ~ 14.1°).

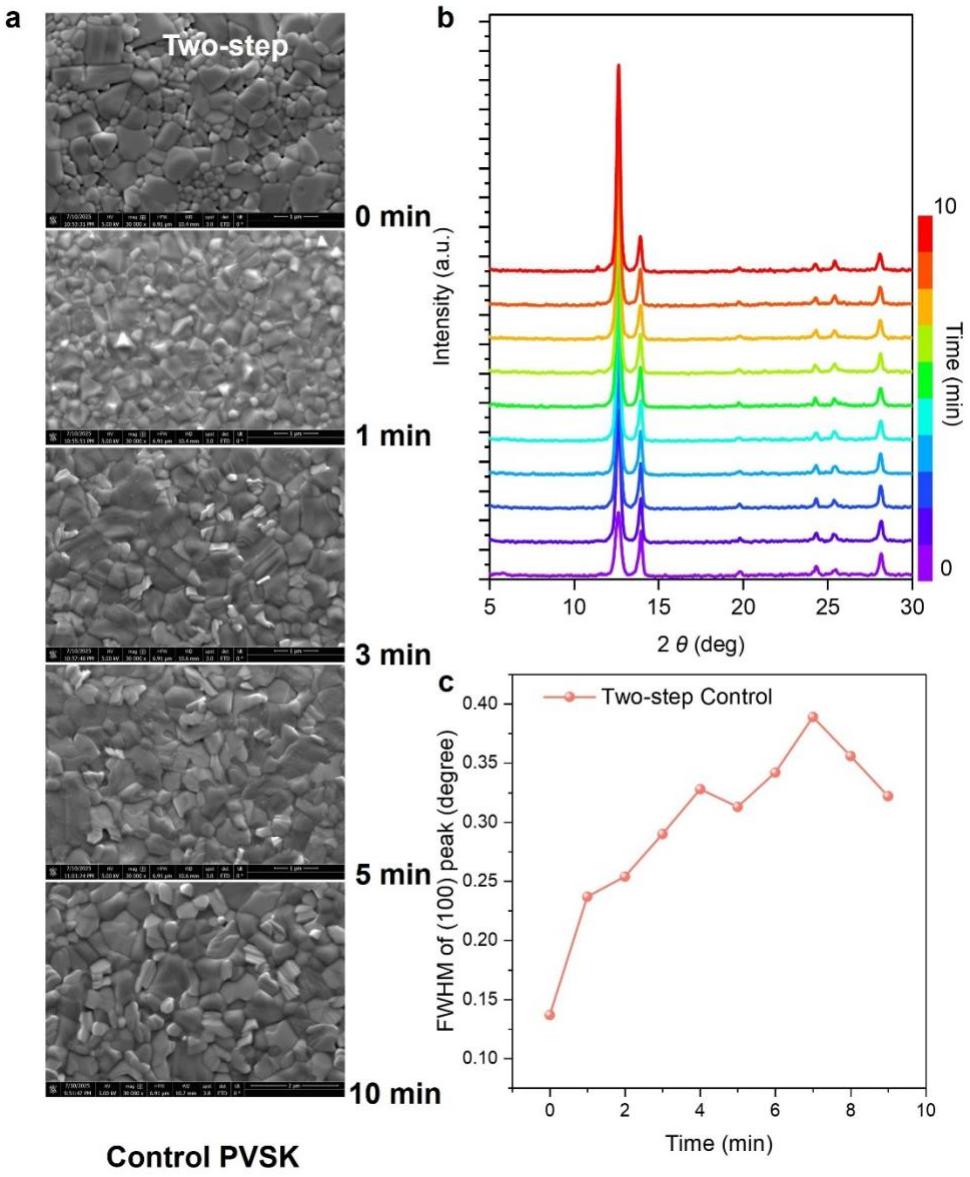

Supplementary Fig. 21. Crystallization evolution of a pristine perovskite film prepared *via* the two-step method. Characterization of the morphological and structural evolution of a pristine (control) perovskite film during thermal annealing. **a,** SEM images showing the film morphology at different annealing times. **b,** Corresponding XRD patterns at different annealing times. **c,** Full width at half maximum (FWHM) of the main perovskite diffraction peak as a function of annealing time, with the values extracted from the data presented in panel **b**.

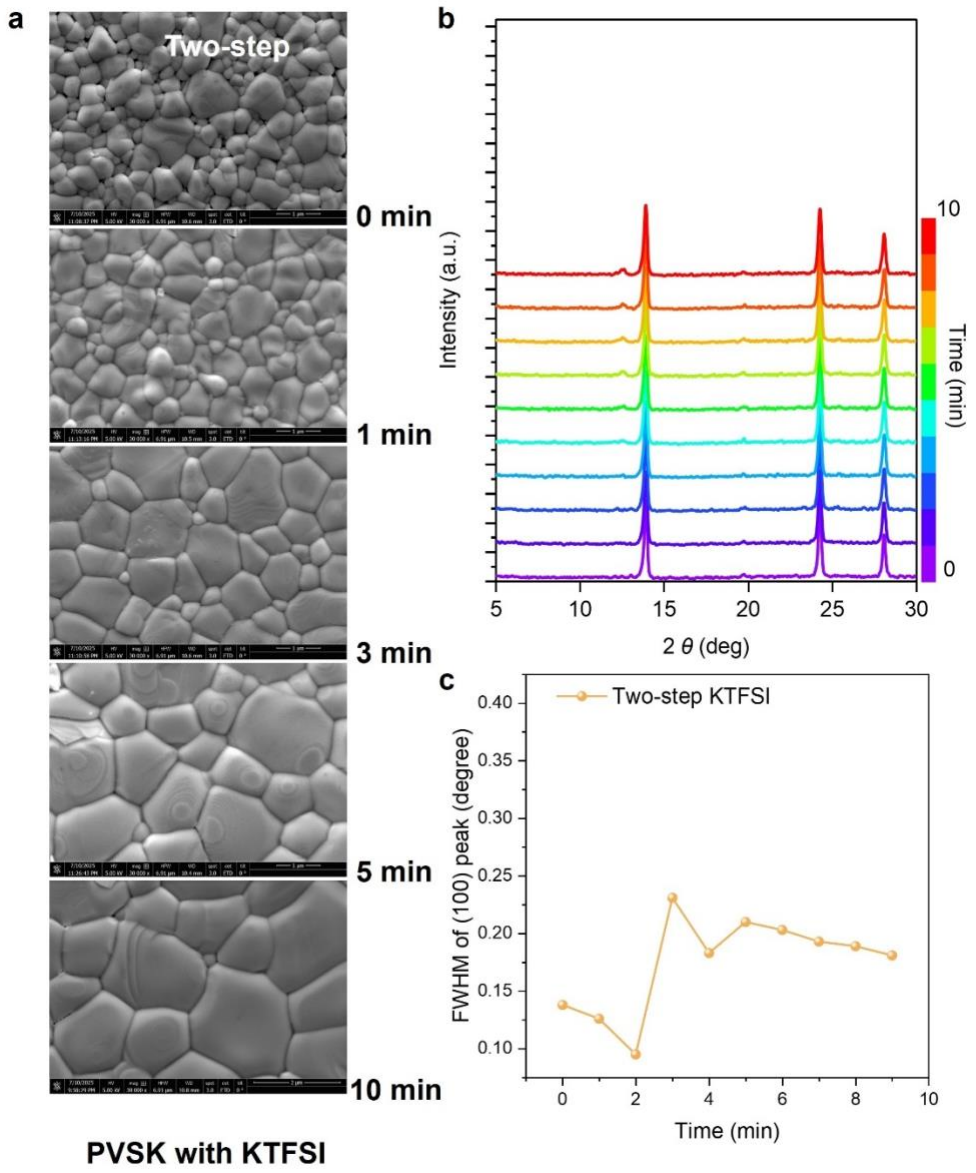

Supplementary Fig. 22. Crystallization evolution of a KTFSI-doped perovskite film prepared *via* the two-step method. Characterization of the morphological and structural evolution of a the KTFSI doped perovskite (PVSK with KTFSI) film during thermal annealing. **a,** SEM images showing the film morphology at different annealing times. **b,** Corresponding XRD patterns at different annealing times. **c,** FWHM of the main perovskite diffraction peak as a function of annealing time, with the values extracted from the data presented in panel **b**.

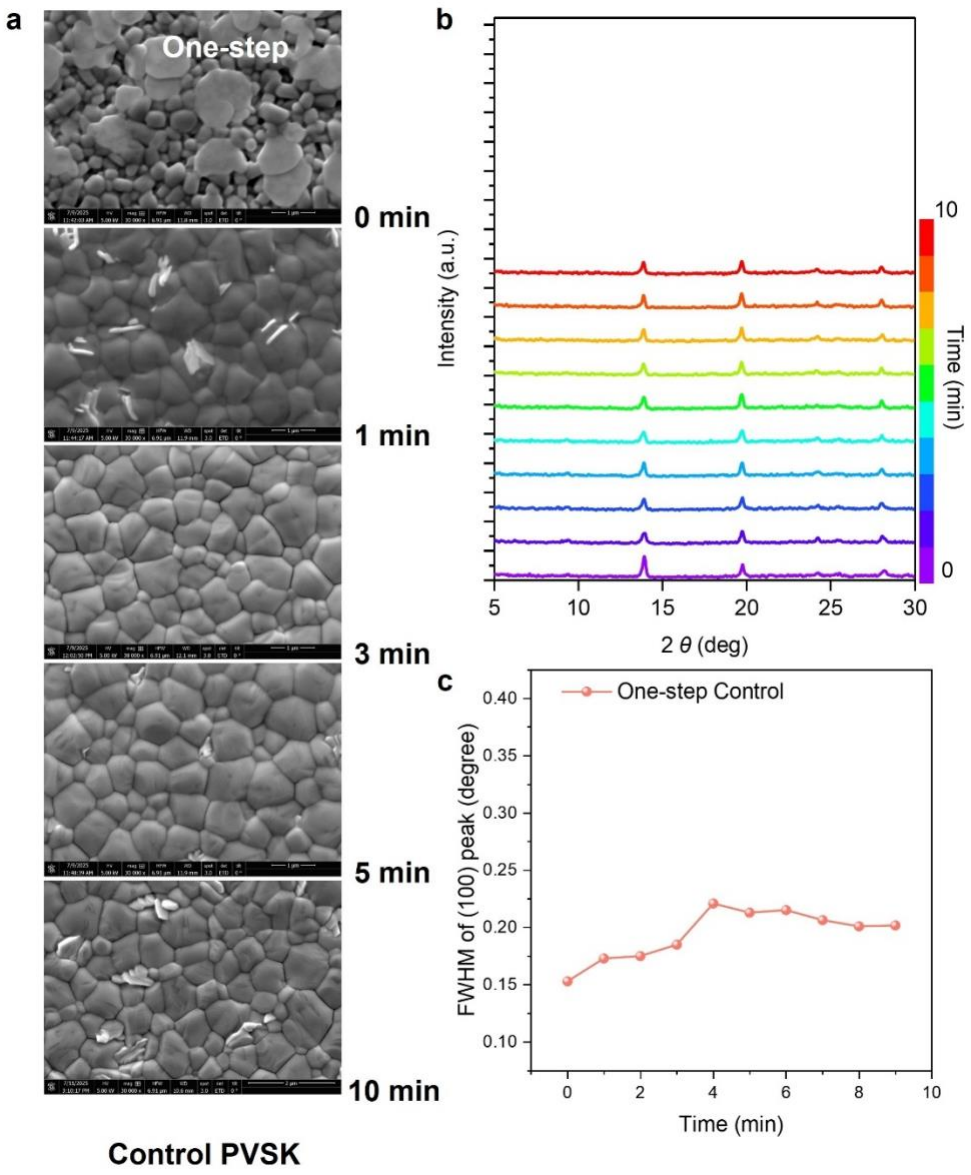

Supplementary Fig. 23. Crystallization evolution of a pristine perovskite film prepared *via* the one-step method. Characterization of the morphological and structural evolution of a pristine (control) perovskite film during thermal annealing. **a,** SEM images showing the film morphology at different annealing times. **b,** Corresponding XRD patterns at different annealing times. **c,** FWHM of the main perovskite diffraction peak as a function of annealing time, with the values extracted from the data presented in panel **b**.

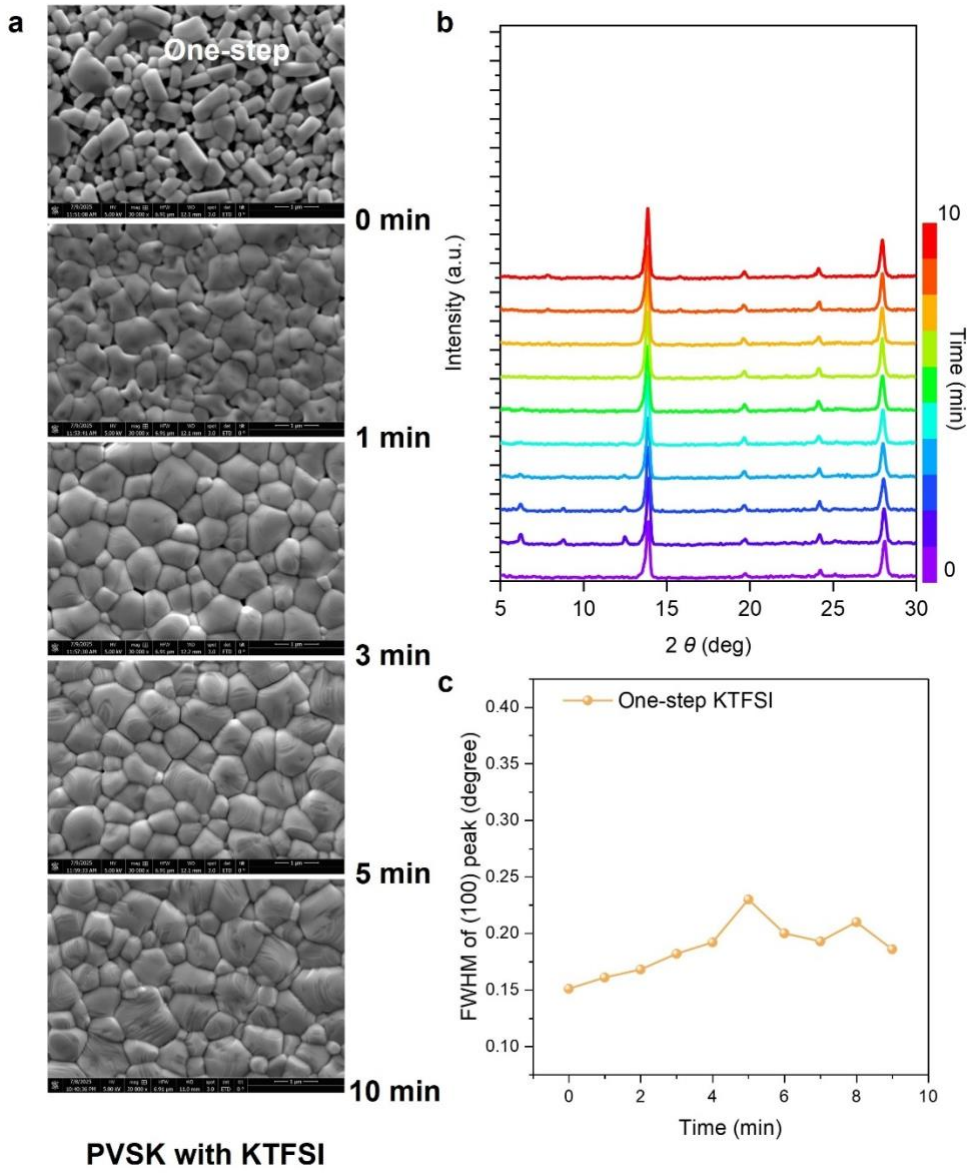

Supplementary Fig. 24. Crystallization evolution of a KTFSI-doped perovskite film prepared *via* the one-step method. Characterization of the morphological and structural evolution of a KTFSI doped perovskite (PVSK with KTFSI) film during thermal annealing. **a,** SEM images showing the film morphology at different annealing times. **b,** Corresponding XRD patterns at different annealing times. **c,** FWHM of the main perovskite diffraction peak as a function of annealing time, with the values extracted from the data presented in panel **b**.

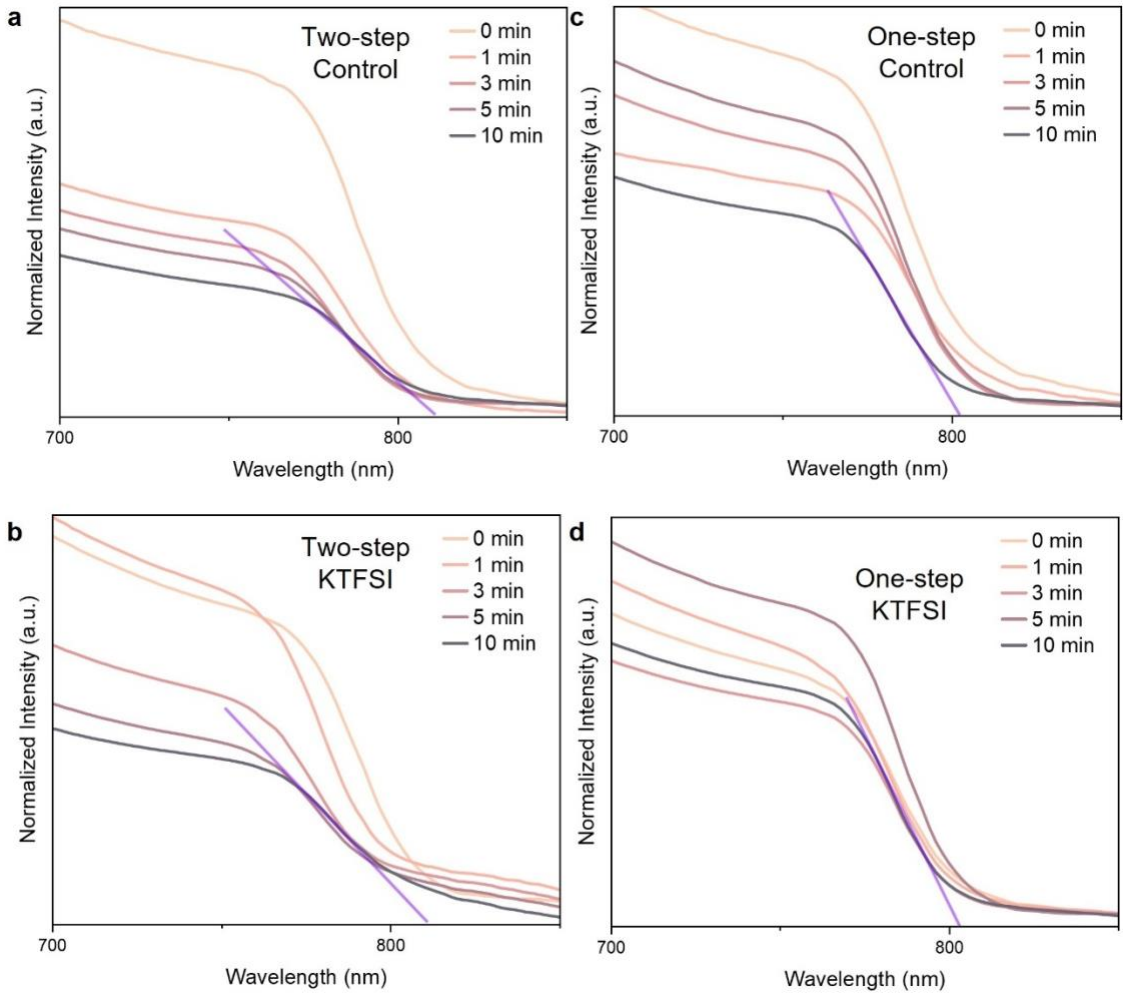

Supplementary Fig. 25. Evolution of UV-Vis absorption spectra for the pristine and KTFSI-doped perovskite films during annealing. Time-resolved UV-Vis absorption spectra of the perovskite films at different stages of annealing at 150 °C, comparing pristine (control) and KTFSI-doped films for both one-step and two-step fabrication methods. **a, b,** Spectral evolution for the films prepared *via* the two-step method: **a,** control film, and **b,** KTFSI-doped film. **c, d,** Spectral evolution for the films prepared *via* the one-step method: **c,** control film, and **d,** KTFSI-doped film. The tangent line indicates that the incorporation of KTFSI does not affect the optical bandgap of the perovskite film. For one-step PVSK: E_g = 1.54 eV. For two-step PVSK: E_g = 1.53 eV.

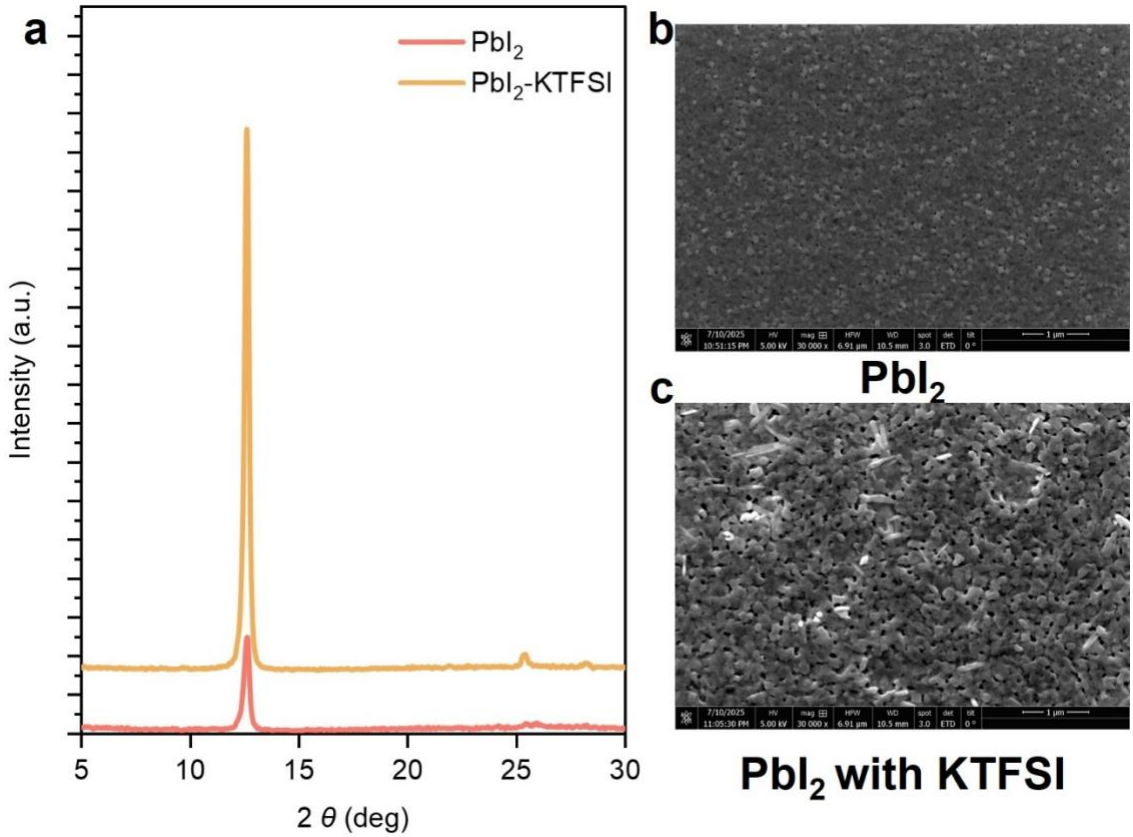

Supplementary Fig. 26. Comparison of the pristine and KTFSI-doped PbI_2 films for the two-step method. a, Comparison of the XRD patterns for the pristine and KTFSI-doped PbI_2 films. **b, c,** Top-view SEM images showing the surface morphology of **b,** a pristine PbI_2 film and **c,** a KTFSI-doped PbI_2 film.

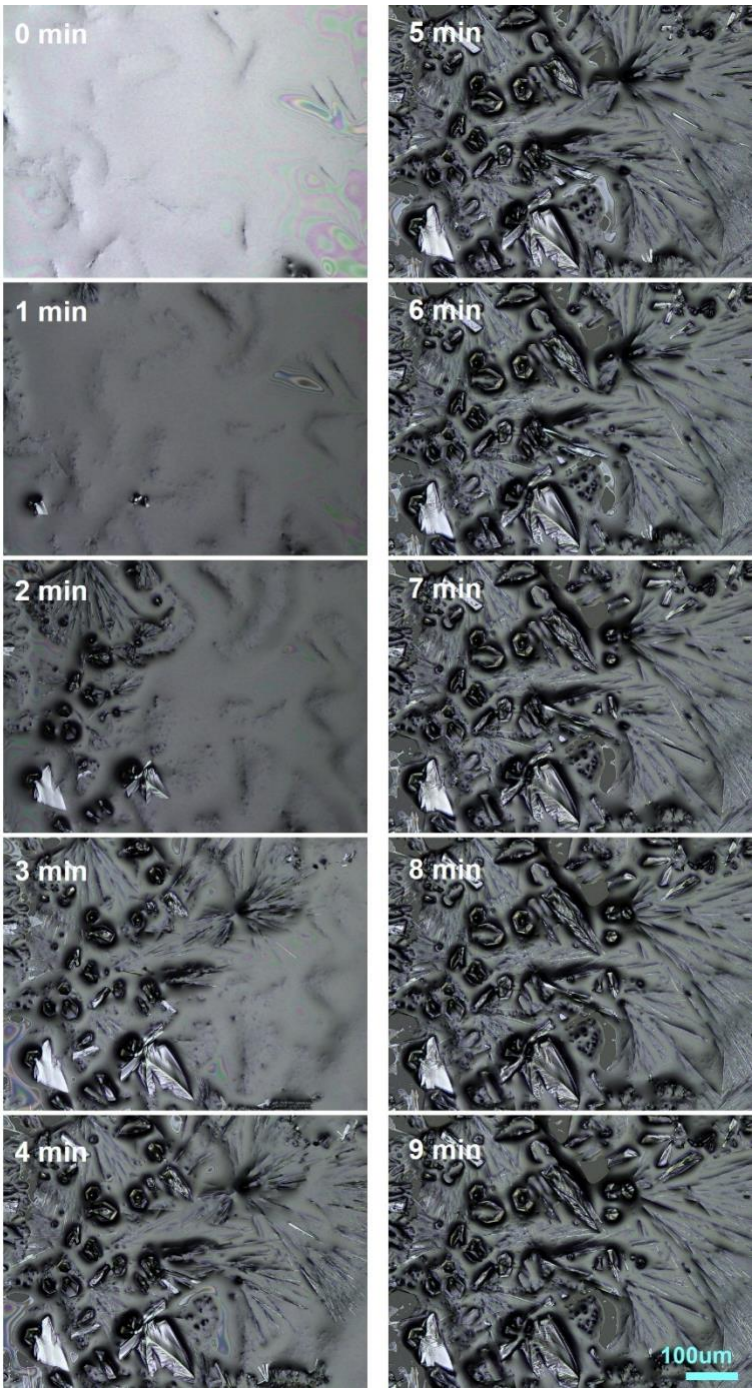

Supplementary Fig. 27. Crystallization of a pristine one-step perovskite solution during solvent evaporation. Optical microscopy images showing the crystallization process of a perovskite film from a one-step precursor solution (DMF/DMSO) as the solvent naturally evaporates for 9 min. The scale bar for all images is 100 μm.

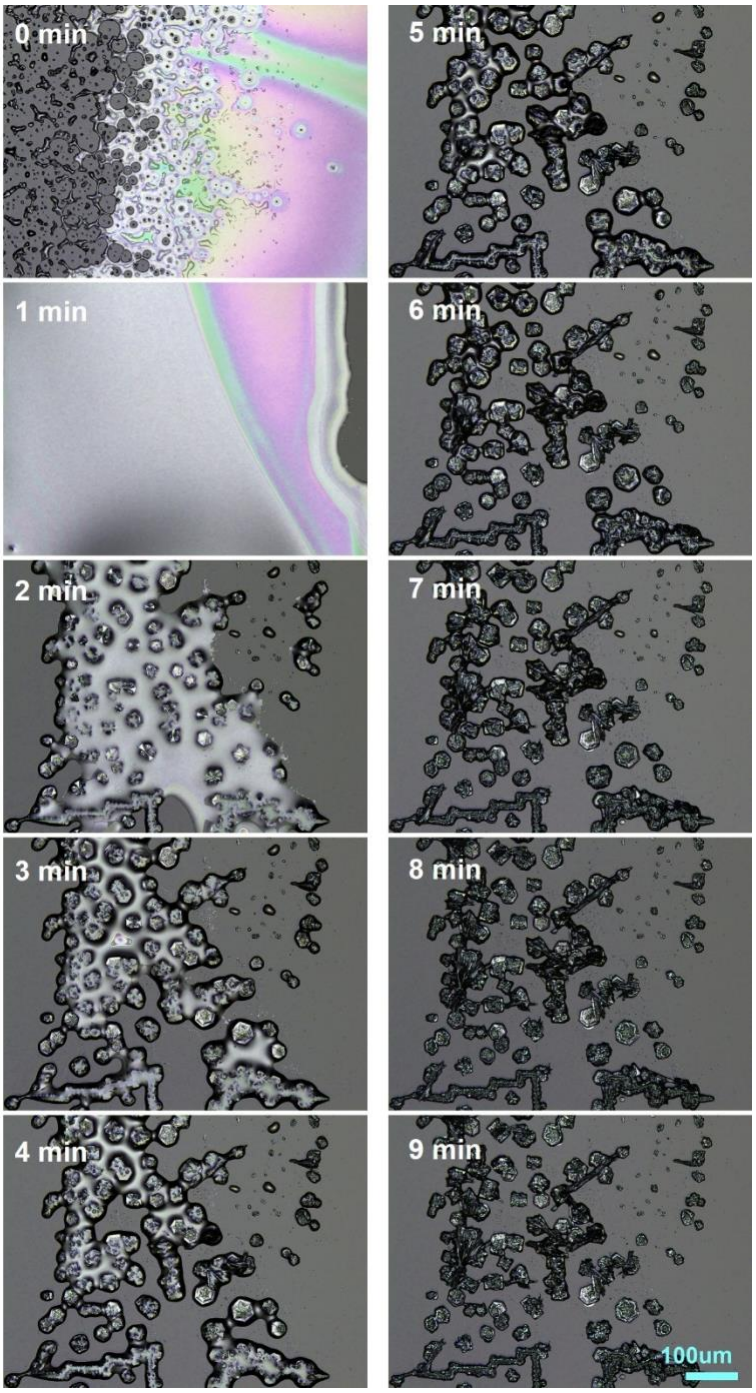

Supplementary Fig. 28. Crystallization of a KTFSI-doped one-step perovskite solution during solvent evaporation. Optical microscopy images showing the crystallization process of a KTFSI-doped perovskite film from a one-step precursor solution (DMF/DMSO) as the solvent naturally evaporates for 9 min. All images have the same size, and the scale bar is 100 μm.

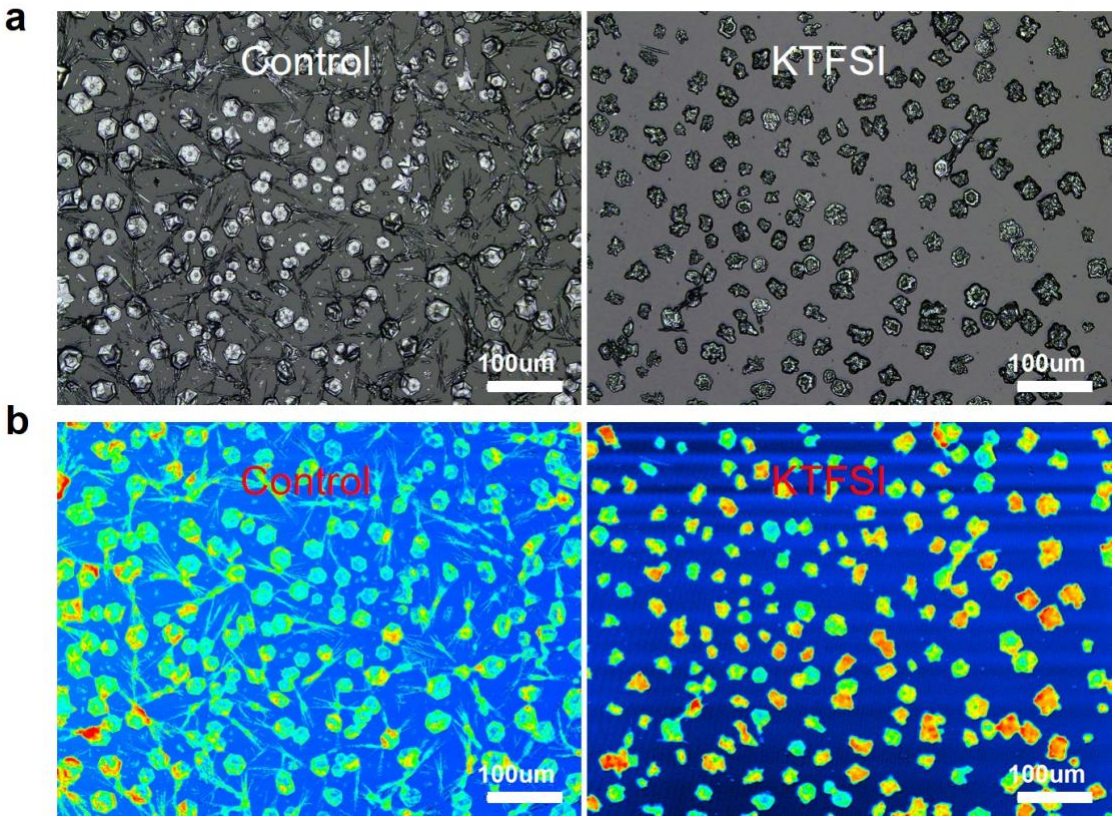

Supplementary Fig. 29. Morphology of the perovskite crystals grown from a DMF/DMSO solution after solvent evaporation. a, Optical microscopy images of the resulting crystals from the control and KTFSI-doped solutions. **b,** Corresponding 3D pseudo-color images from laser scanning microscopy, showing the topography of the crystals.

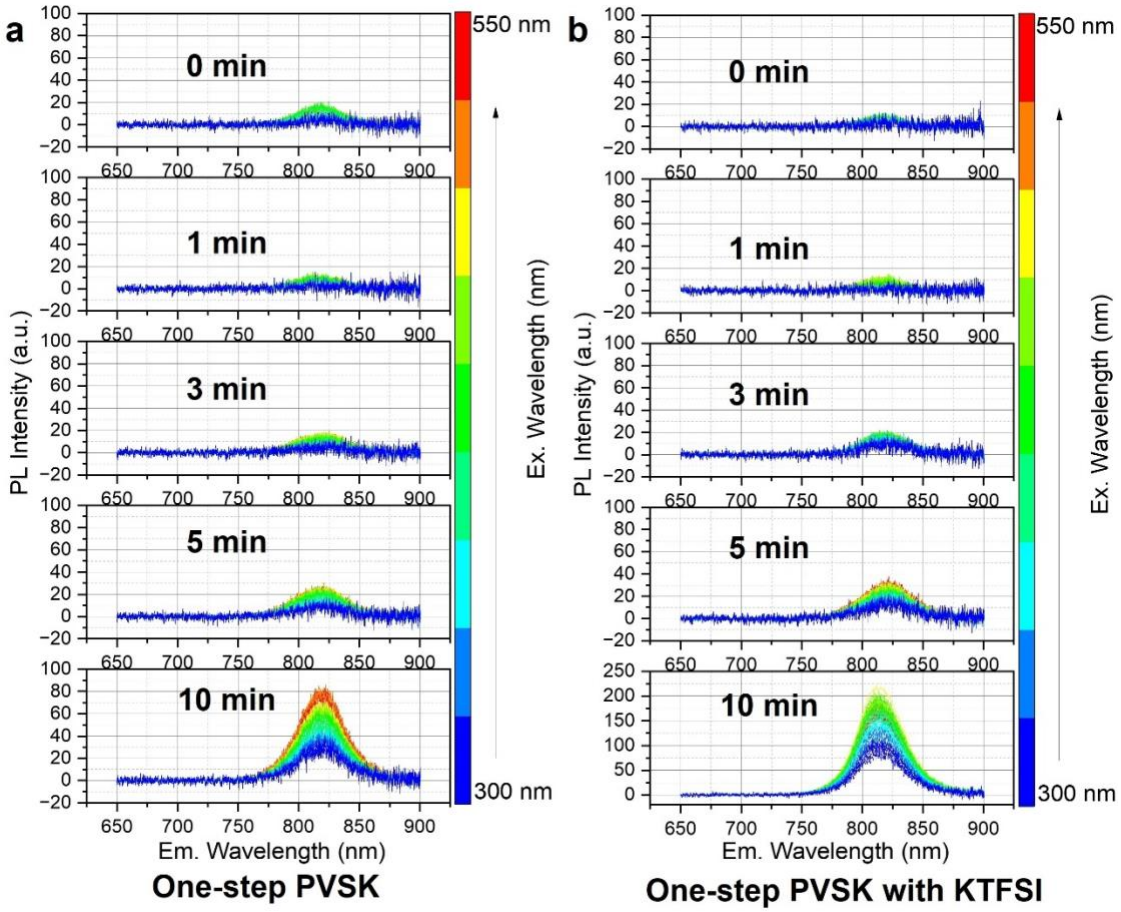

Supplementary Fig. 30. Evolution of the excitation-emission matrix (EEM) fluorescence spectra for one-step perovskite films during annealing. The figure compares the EEM spectra for the pristine (control) and KTFSI-doped films at different annealing times (0, 1, 3, 5, and 10 min). The spectra show the emission intensities in the 650-900 nm range as a function of excitation from 300-500 nm. **a,** Pristine film without KTFSI. **b,** KTFSI-doped film.

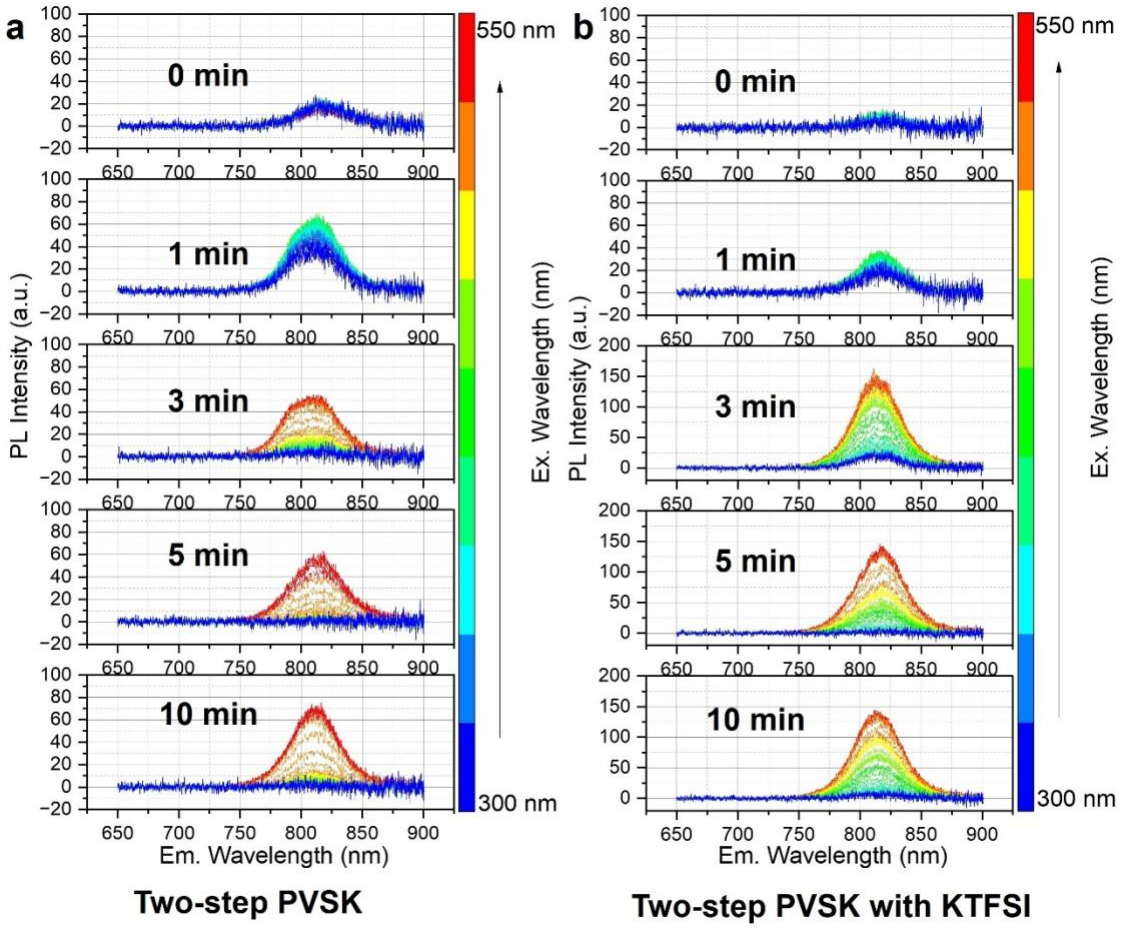

Supplementary Fig. 31. Evolution of the excitation-emission matrix (EEM) fluorescence spectra for two-step perovskite films during annealing. The figure compares the EEM spectra for the pristine (control) and KTFSI-doped films at different annealing times (0, 1, 3, 5, and 10 min). The spectra show the emission intensities in the 650-900 nm range as a function of excitation from 300-500 nm. **a,** Pristine film without KTFSI. **b,** KTFSI-doped film.

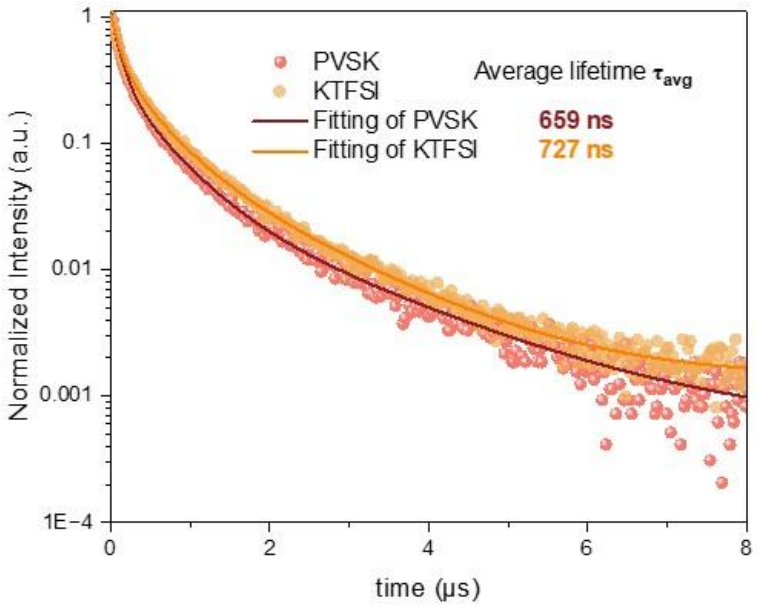

Supplementary Fig. 32. Time-resolved photoluminescence (TRPL) decay of the perovskite films. Comparison of the TRPL decay curves and tri-exponential fits for perovskite films prepared with different potassium salts. The orange dots and fitting line represent the PVSK film treated with potassium iodide (KI), while the red dots and fitting line represent the PVSK film doped with KTFSI (molar equivalent of KI). The calculated average carrier lifetimes (τ_{avg}) are 659 ns and 727 ns for the control and KTFSI-doped films, respectively.

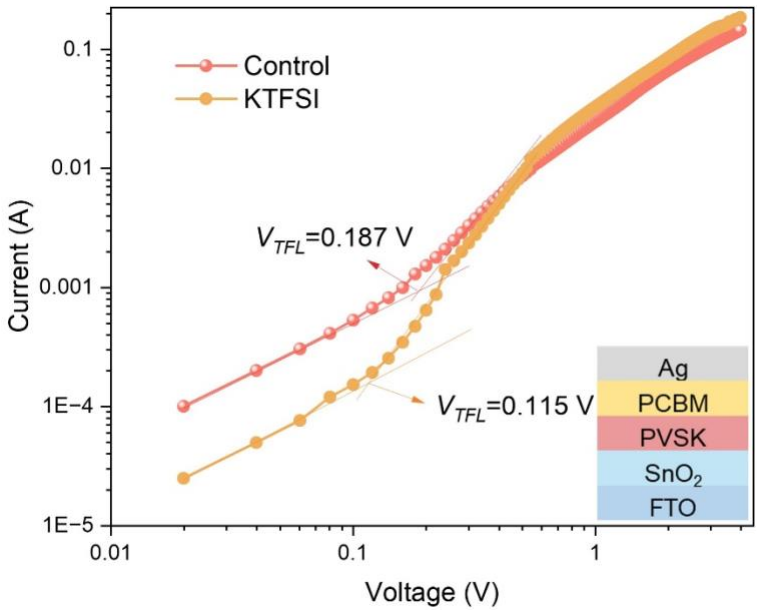

Supplementary Fig. 33. Dark current-voltage (*I-V*) characteristics of the electron-only devices. Dark current-voltage (*I-V*) characteristics of the electron-only devices with the FTO/SnO_2/PVSK/PCBM/Ag configuration employing the perovskite films with KI (Control, red dots) and KTFSI (orange dots). The trap-filled limit voltages (V_{TFL}) are determined to be 0.187 V and 0.115 V for the control and KTFSI-doped films, respectively.

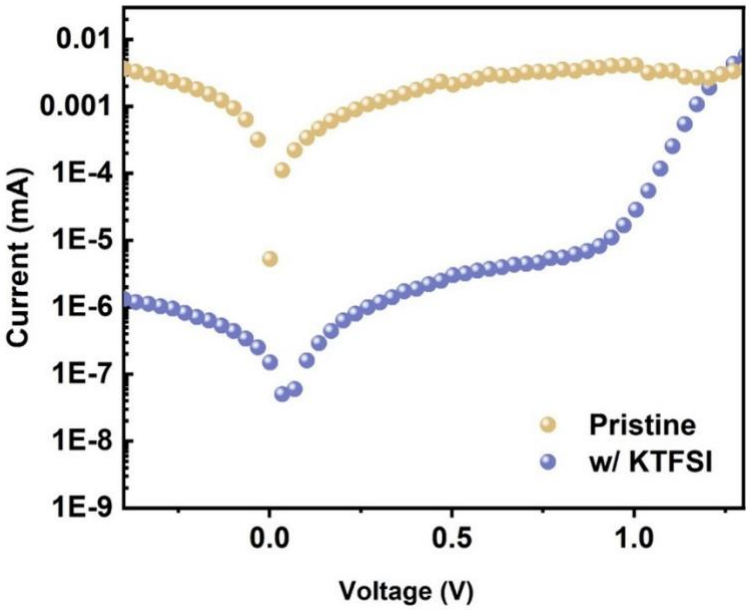

Supplementary Fig. 34. Dark current-voltage (*I-V*) characteristics of the pristine and KTFSI incorporated perovskite films with the configuration of FTO/SnO_2/PVSK/spiro/Au.

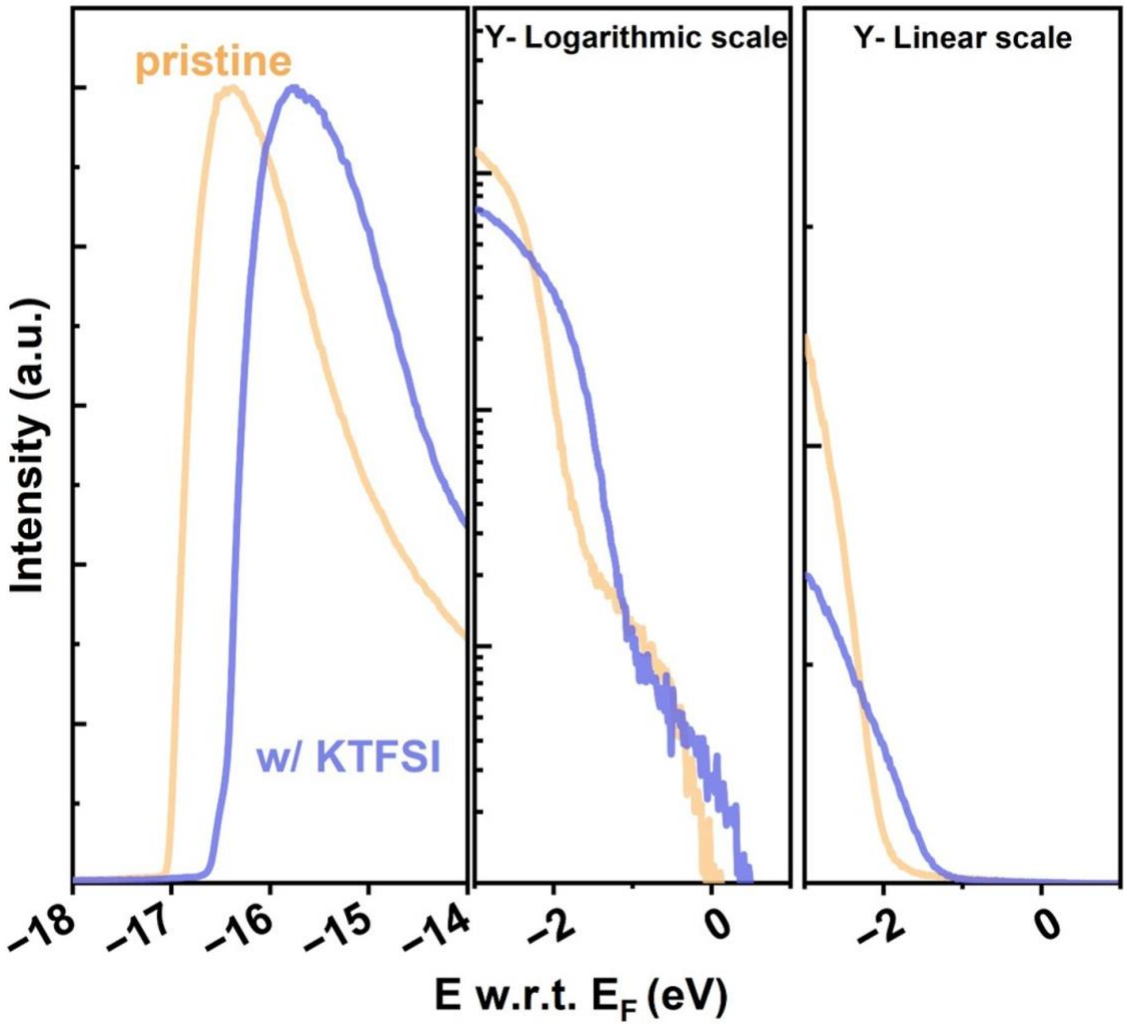

Supplementary Fig. 35. UPS results of the pristine perovskite layer (yellow curves) and KTFSI incorporated perovskite film (blue curves).

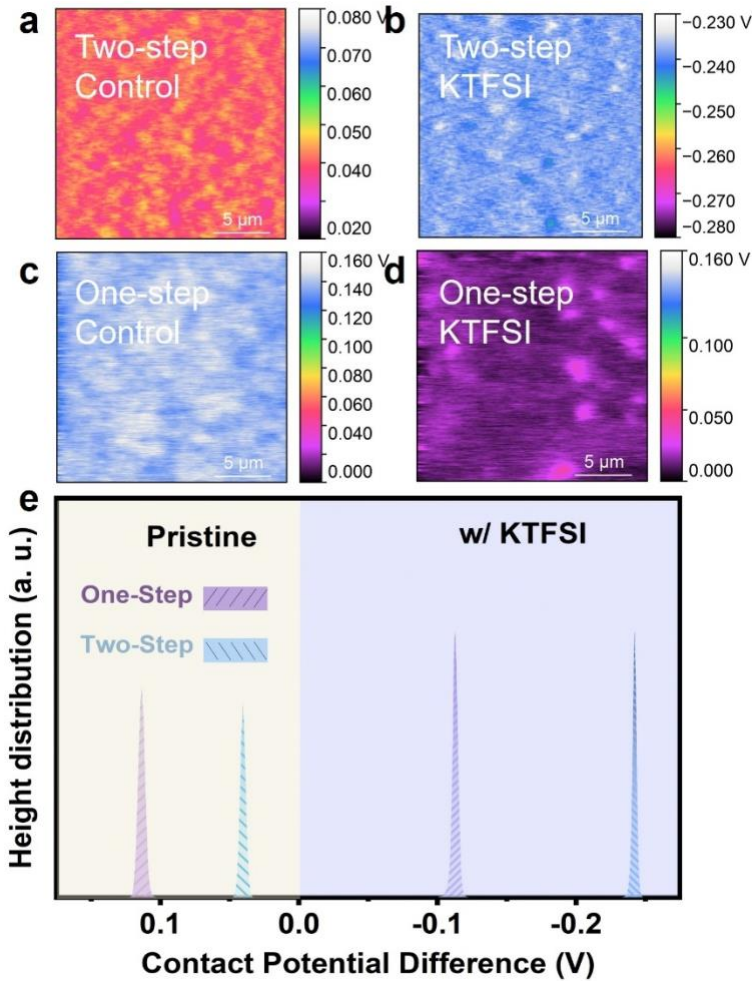

Supplementary Fig. 36. Combined **a,b,c,d,** KPFM images and **e,** CPD variation acquired on the one-step perovskite layer without (Control) and with KTFSI treatment. The CPD variations infer the WF differences comparing both samples. Scale bar in **a** - **d** is 5 µm.

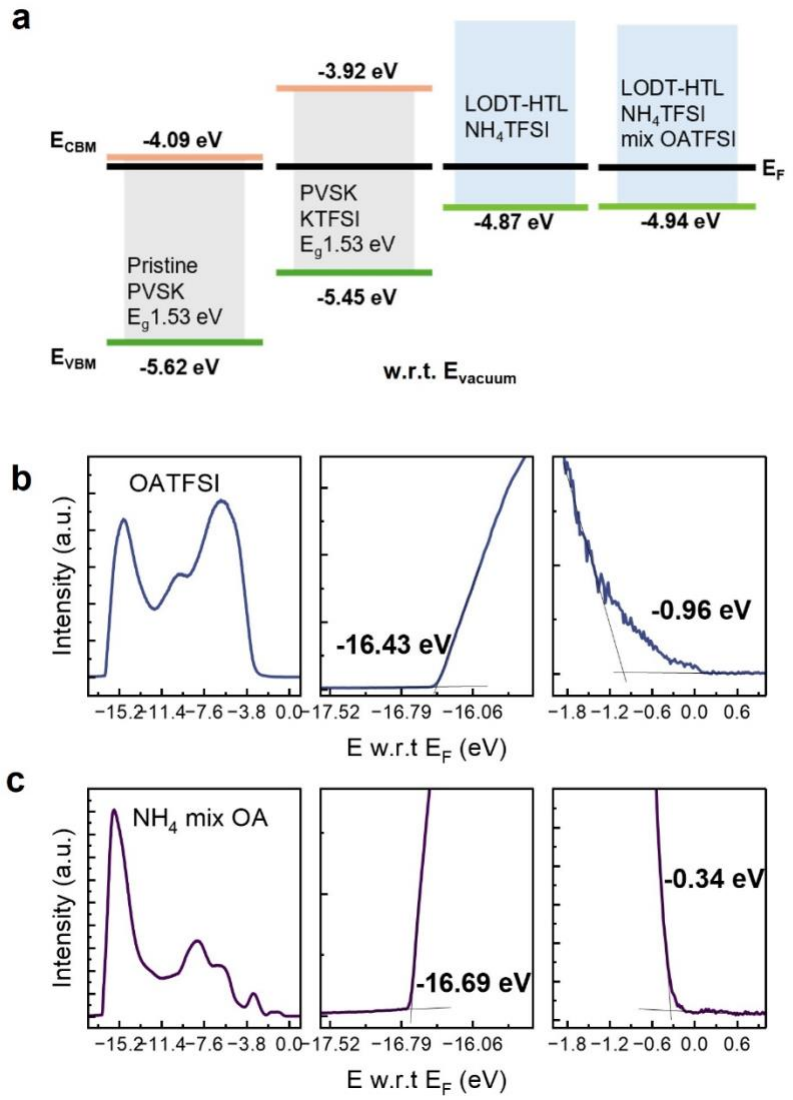

Supplementary Fig. 37. Energy levels of perovskites and HTLs. a, illustration of energy level alignments between perovskites and HTLs. From left to right: pristine perovskite, KTFSI added PVSK, LODT-HTL with NH_4TFSI, and LODT-HTL co-doped with OATFSI (1% mol to spiro); E_{VBM} are determined based on the UPS results and E_{CBM} are determined based on the low energy inverse photoemission spectroscopy (LEIPS) results, with their values represented with respect to the vacuum level (w.r.t. E_{vacuum}). UPS results of **b,** LODT-HTL with OATFSI only and **c,** co-doped with NH_4TFSI and OATFSI in LODT-HTL with respect to the Fermi level, E_F (w.r.t. E_F).

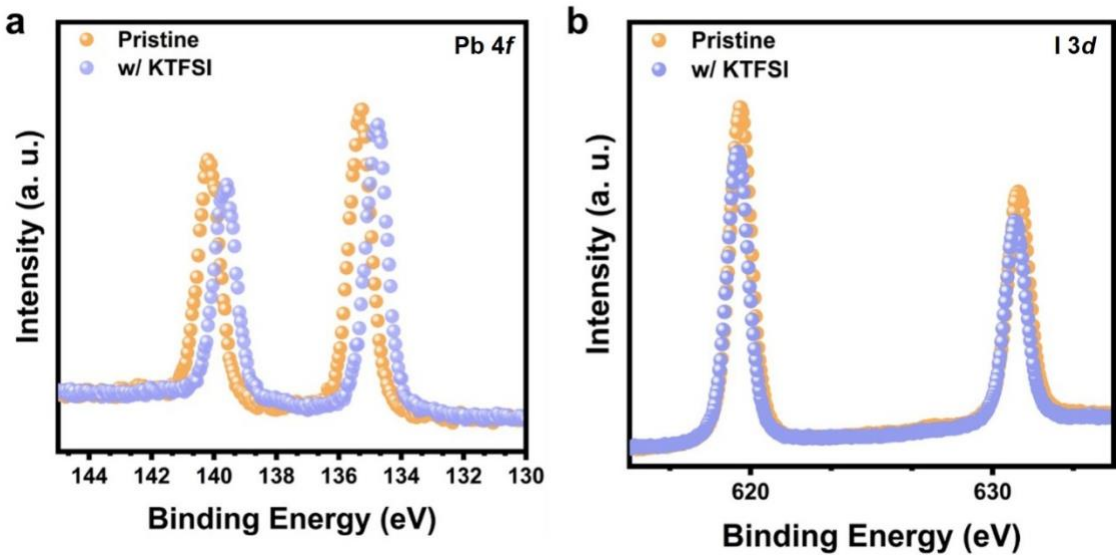

Supplementary Fig. 38. XPS results of **a**, Pb 4*f* and **b**, I 3*d* core levels for the pristine perovskite film and KTFSI treated perovskite.

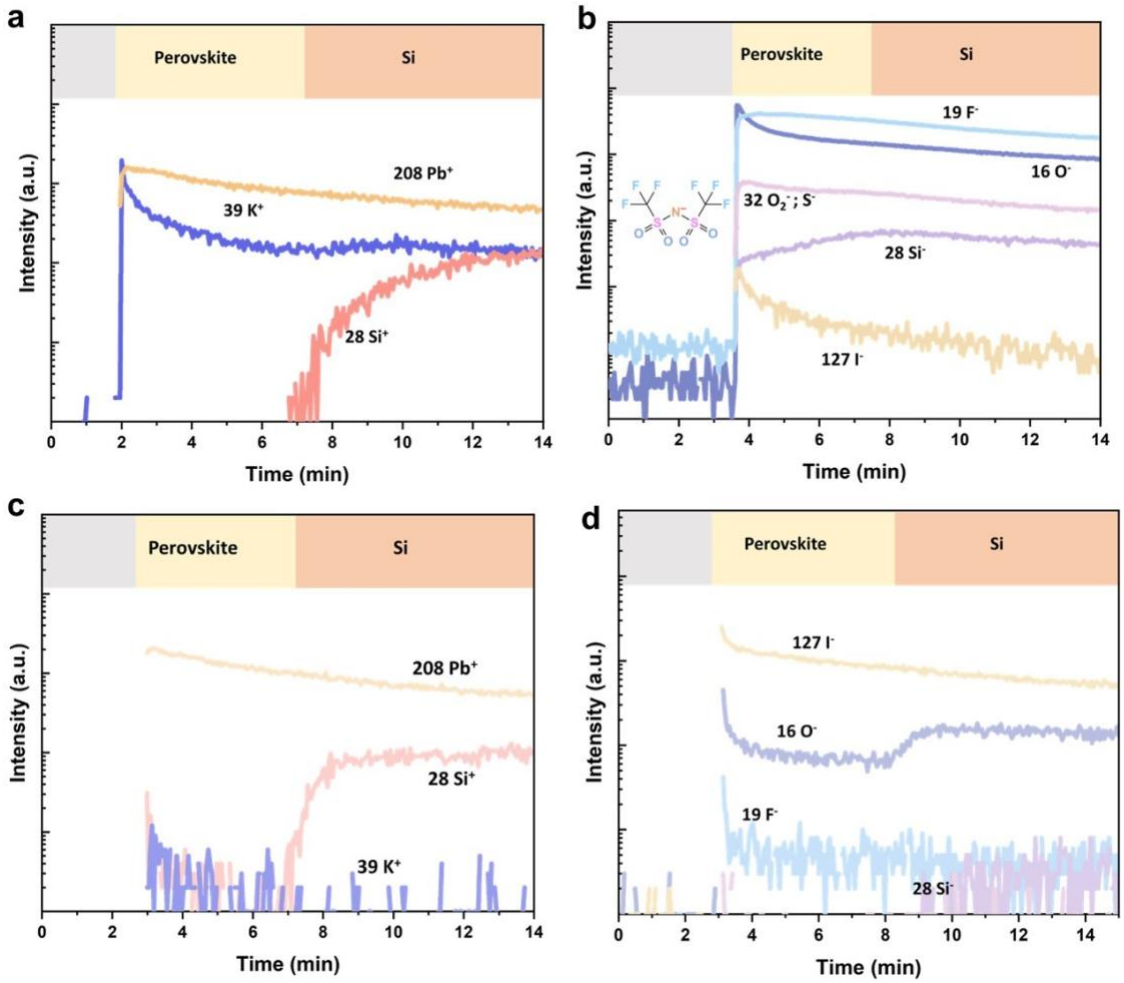

Supplementary Fig. 39. SIMS results of **a**, **b**, the KTFSI treated sample and **c**, **d**, pristine perovskite layer (on Si substrate). Spectra in **a** and **c**, correspond to the positive detection mode, while **b**, and **d**, correspond to the negative mode of SIMS.

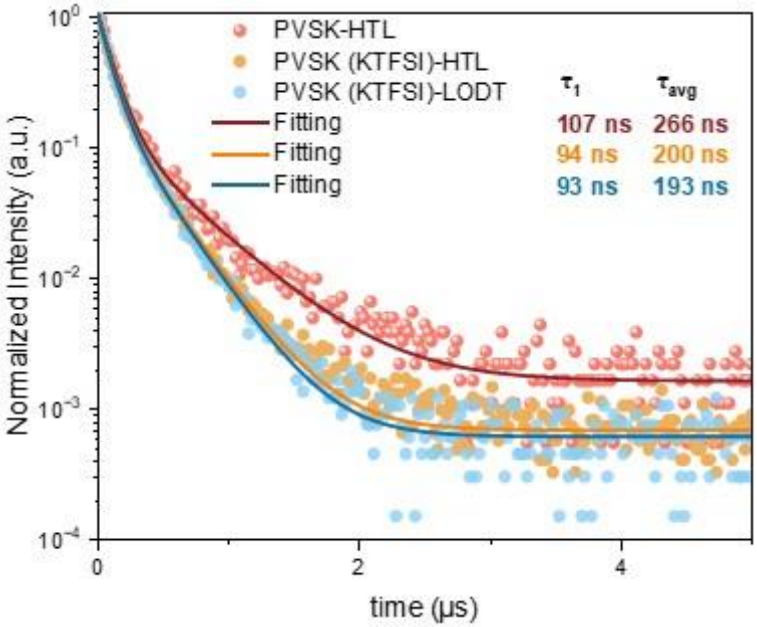

Supplementary Fig. 40. TRPL curves with bi-exponential fits of conventional LiTFSI doped spiro (HTL) on pristine perovskite (PVSK-HTL, red dots), HTL on KTFSI modified perovskite [PVSK(KTFSI)-HTL, orange dots], and LODT-OA (co-doped NH_4TFSI with 1% mol OATFSI) on KTFSI modified perovskite [PVSK(KTFSI)-LODT, blue dots] deposited on quartz substrates, comparing different interfacial carrier dynamics.

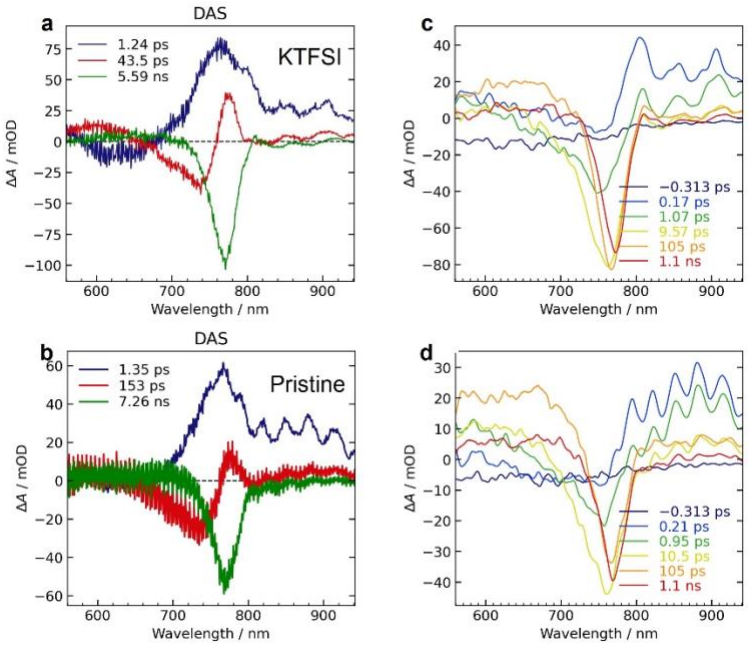

Supplementary Fig. 41. Temporal evolution of the differential absorption signals (DAS) and delay time-dependent transient absorption spectra (TAS) at the pump-probe delay time of 0 –1100 ps TAS **a,c,** KTFSI added perovskite film with LiTFSI-spiro-HTL on quartz and **b,d,** as pristine perovskite with Li-spiro. Signals over a broad spectral range (560–940 nm) and across time delays from sub-picoseconds to nanoseconds. A pronounced negative feature centered around 760-780 nm is observed, corresponding to ground-state bleaching (GSB) of perovskite due to band-edge state filling by photogenerated carriers.

a

b

Lattice Constant	$FAPbI_3$	$FAPbI_3$ + KTFSI
a (Å)	8.66	8.67
b (Å)	8.66	8.67
c (Å)	7.93	7.94
Alpha (°)	90	90
Beta (°)	90	90
Gamma (°)	120	120
Volume ($Å^3$)	515	517
Crystal System	Hexagonal P	Hexagonal P

Supplementary Fig. 42. Photos and lattice constants of a $FAPbI_3$ single crystal. a, Photos of $FAPbI_3$ and KTFSI (3 mg/mL) doped $FAPbI_3$ single crystal grown *via* the inverse temperature crystallization (ITC) method[2] using 2-Methoxyethanol (2-Me) as the solvent. The image shows the black, needle-like crystal in the yellow precursor solution. **b,** Crystallographic data, including the lattice constants, obtained from single-crystal X-ray diffraction analysis.

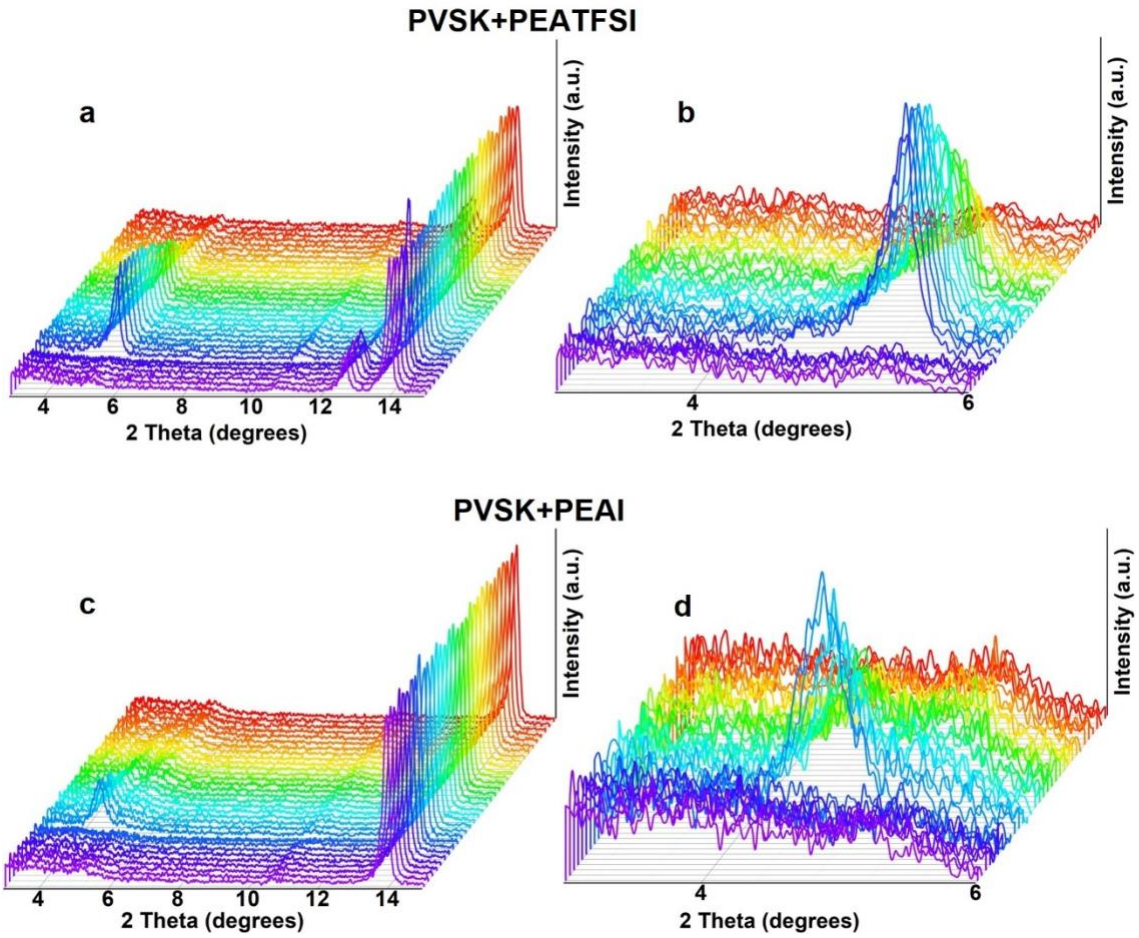

Supplementary Fig. 43. GIXRD (ω = 1°) data employing a heating stage for probing the PVSK thermal stability with **a**, and **b**, PEATFSI and **c**, and **d**, PEAI by keeping the annealing temperature at 70 °C. The acquisition time interval for each spectrum is 1 min. **b**, and **d**, are corresponding zoomed-in plots of PEATFSI and PEAI conditions showing the thermal instabilities of 2D phase. The first recorded plot stands at front (violet color), and each line is sampled every 1 min.

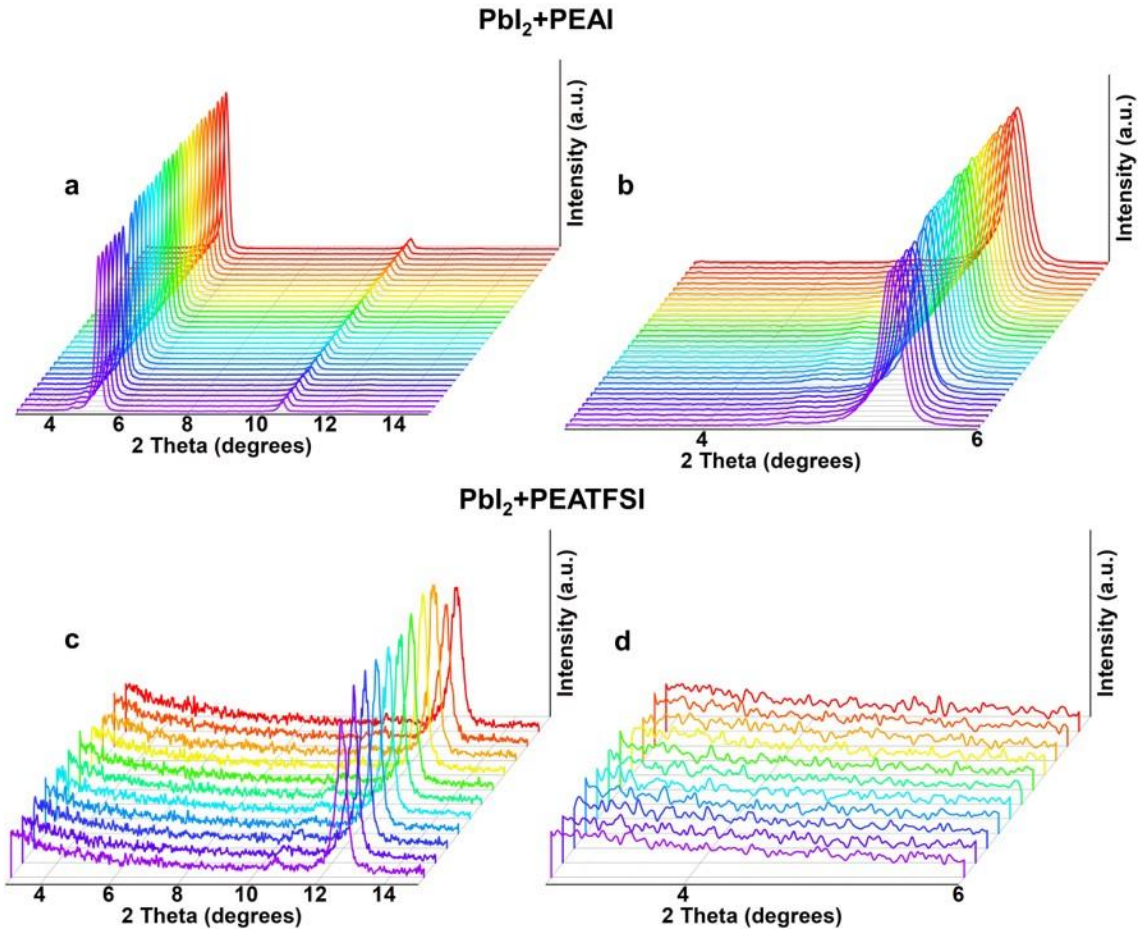

Supplementary Fig. 44 GIXRD (ω = 1°) data employing a heating stage for probing the PbI_2 reaction dynamics with **a**, and **b**, PEATFSI and **c**, and **d**, PEAI by keeping the annealing temperature at 70 °C. The acquisition time interval of each spectrum is 1 min. **b**, and **d**, are corresponding zoomed-in plots showing the thermal behavior of PEATFSI induced 2D phase and PEAI (no 2D phase formation) treated PbI_2 films. The first recorded plot stands at front (violet color), and each line is sampled every 1 min. PbI_2 can react with PEAI to form a stable 2D perovskite, but without the participation of additional iodide ions, PbI_2 cannot react with PEATFSI to form a perovskite phase.

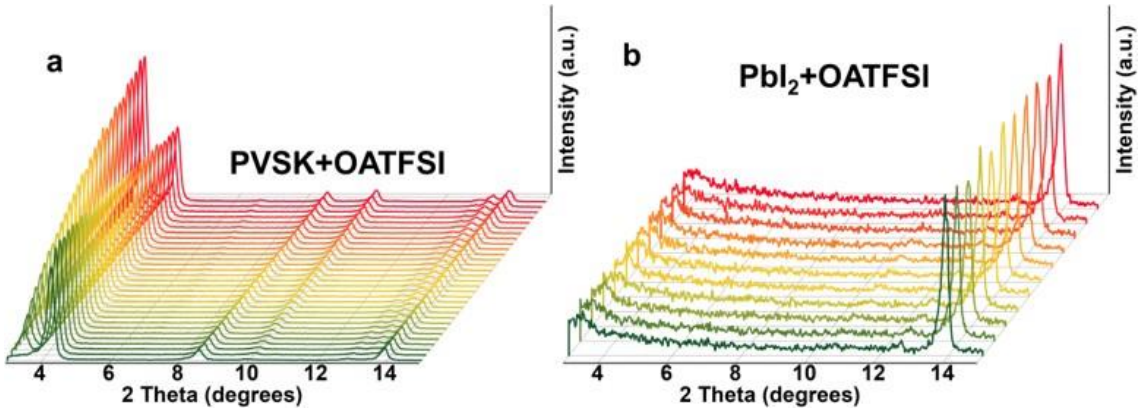

Supplementary Fig. 45 GIXRD (ω = 1°) data employing a heating stage for probing the **a,** PVSK and **b,** PbI_2 thermal stability and reactivity dynamics with OATFSI by keeping the annealing temperature at 70 °C. The acquisition time interval for each GIXRD spectrum is 1 min. The first recorded plot stands at front (green curves), and each line is sampled every 1 min.

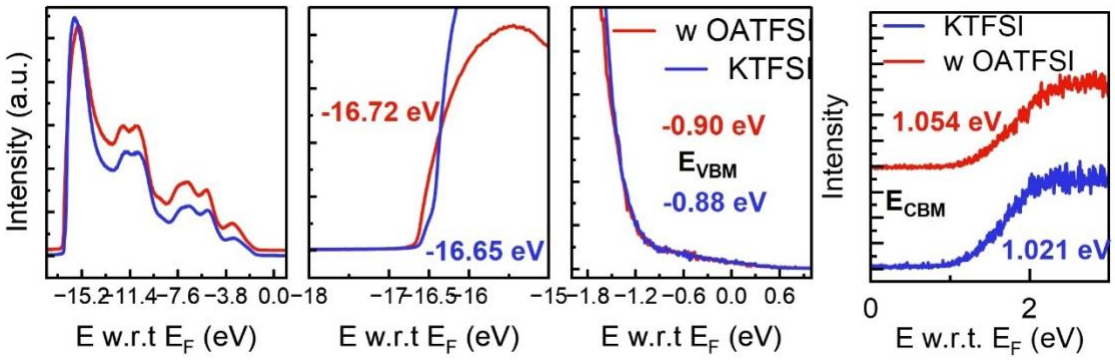

Supplementary Fig. 46. Energy level characterization of the perovskite films using UPS and LEIPS. Combined UPS and LEIPS spectra. The figure compares a KTFSI-doped perovskite film (blue curves) with a KTFSI-doped film with additional post-treatment with OATFSI (red curves).

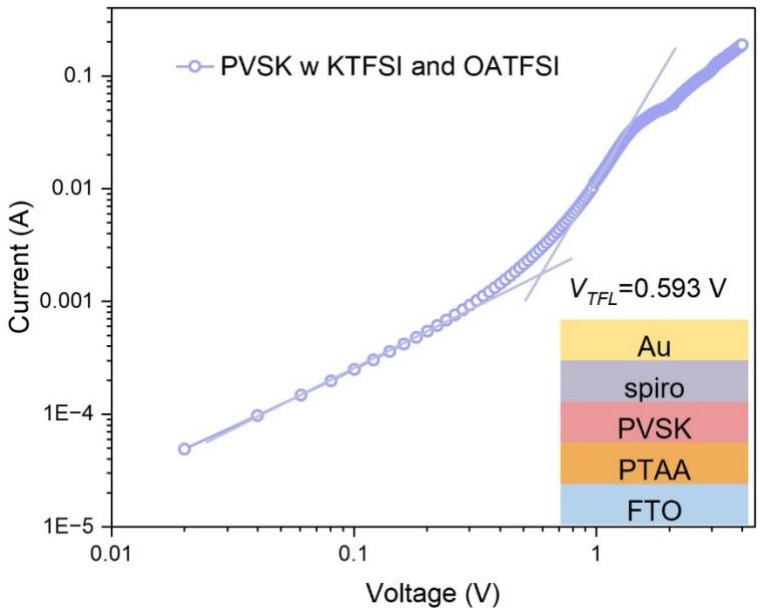

Supplementary Fig. 47. Current-voltage (*I-V*) characteristic of a hole-only device. a, Current-voltage (*I-V*) characteristic of a hole-only device featuring a KTFSI-doped perovskite film with an additional OATFSI post-treatment. The device structure is FTO/PTAA/PVSK/spiro/Au, the perovskite film thickness is 650 nm, and the electrode area is 0.09 cm^2.

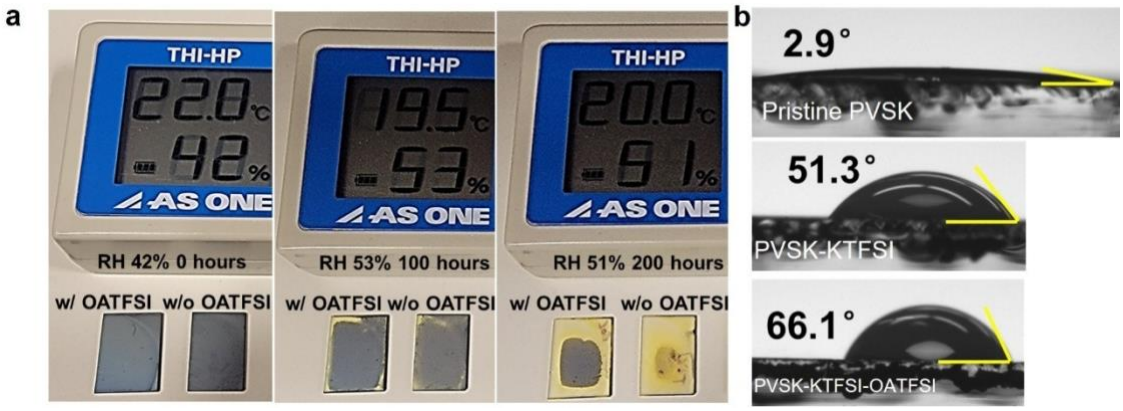

Supplementary Fig. 48. Enhanced hydrophobicity and stability of perovskite films by OATFSI post-treatment. a, Photographs comparing the degradation of an untreated perovskite film and an OATFSI-treated film after storage for 200 h in an ambient environment (25 °C, 42-53% RH). **b,** Water contact angle test on different film surfaces: pristine perovskite (2.9°), KTFSI-doped perovskite (51.3°), and a KTFSI-doped film with an additional OATFSI post-treatment (66.1°).

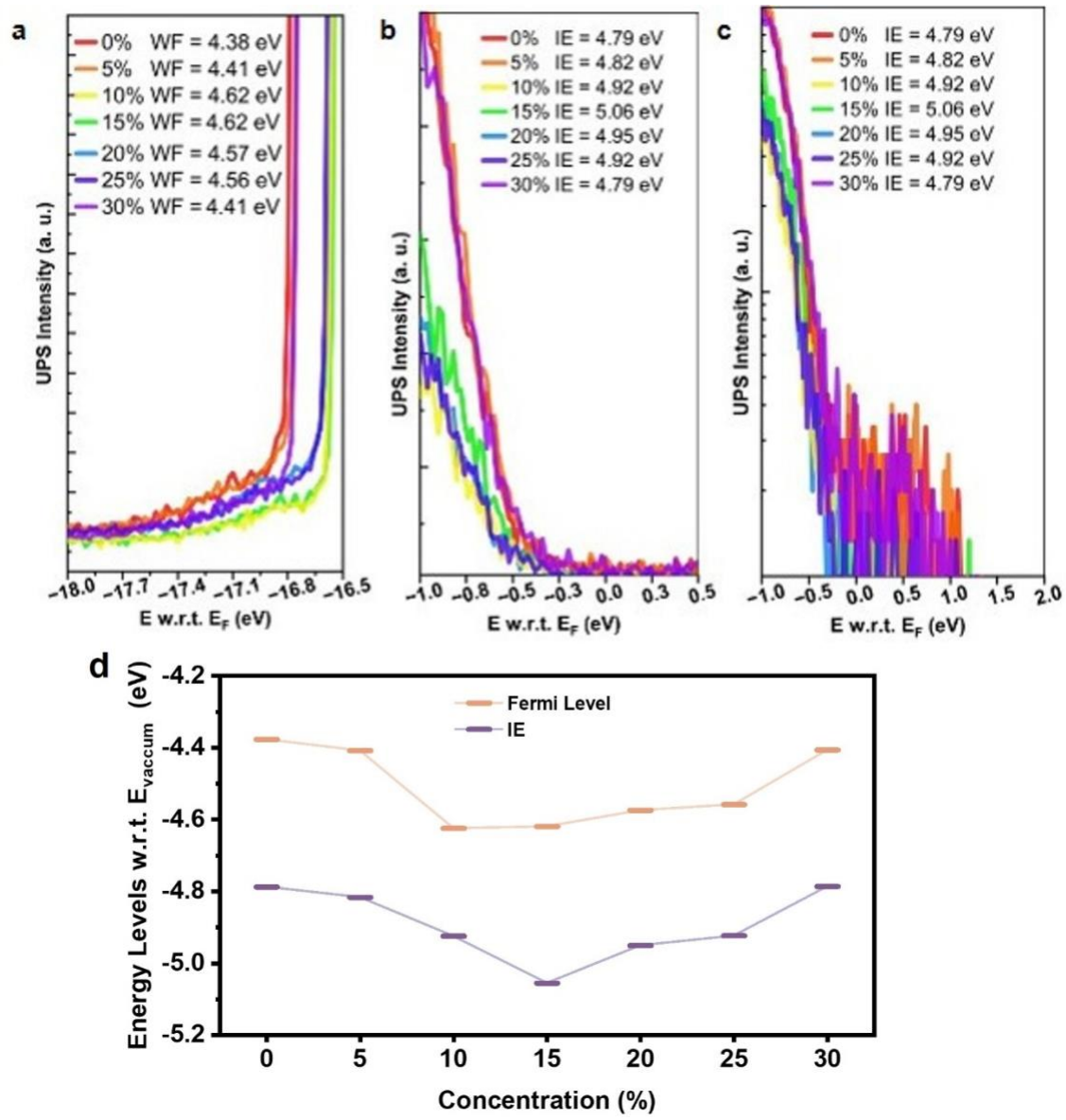

Supplementary Fig. 49. UPS spectra of spiro-HTL with different doping concentrations of NH_4TFSI. UPS (He-Iα = 21.22 eV) spectra showing the changes in the **a,** WF and **b,** (y-axis in linear scale) **c,** (y-axis in logarithmic scale) ionization energy (IE) values upon increasing the NH_4TFSI doping concentration. **d,** Energy level diagram showing the changes in the Fermi level and IE positions upon increasing the NH_4TFSI doping concentration.

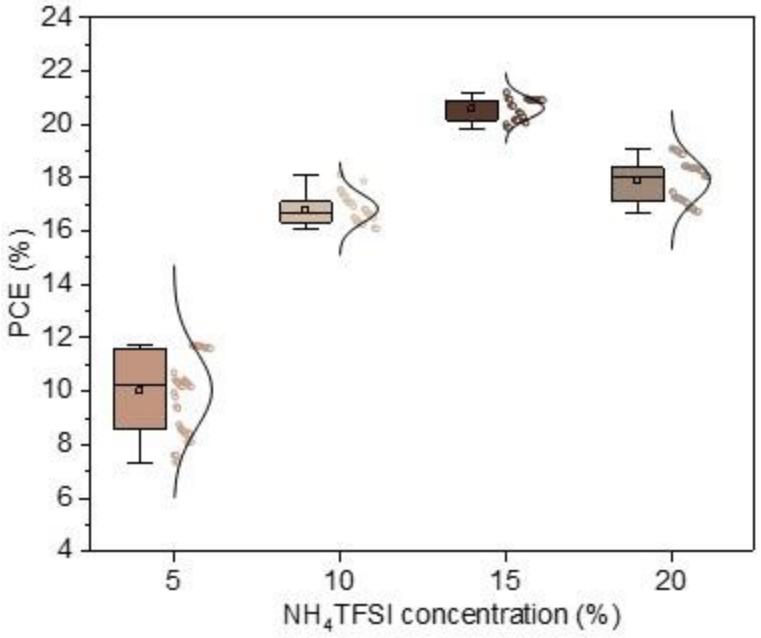

Supplementary Fig. 50. Efficiency optimization with the box chart of the NH_4TFSI concentration in the LODT method applied in PSCs.

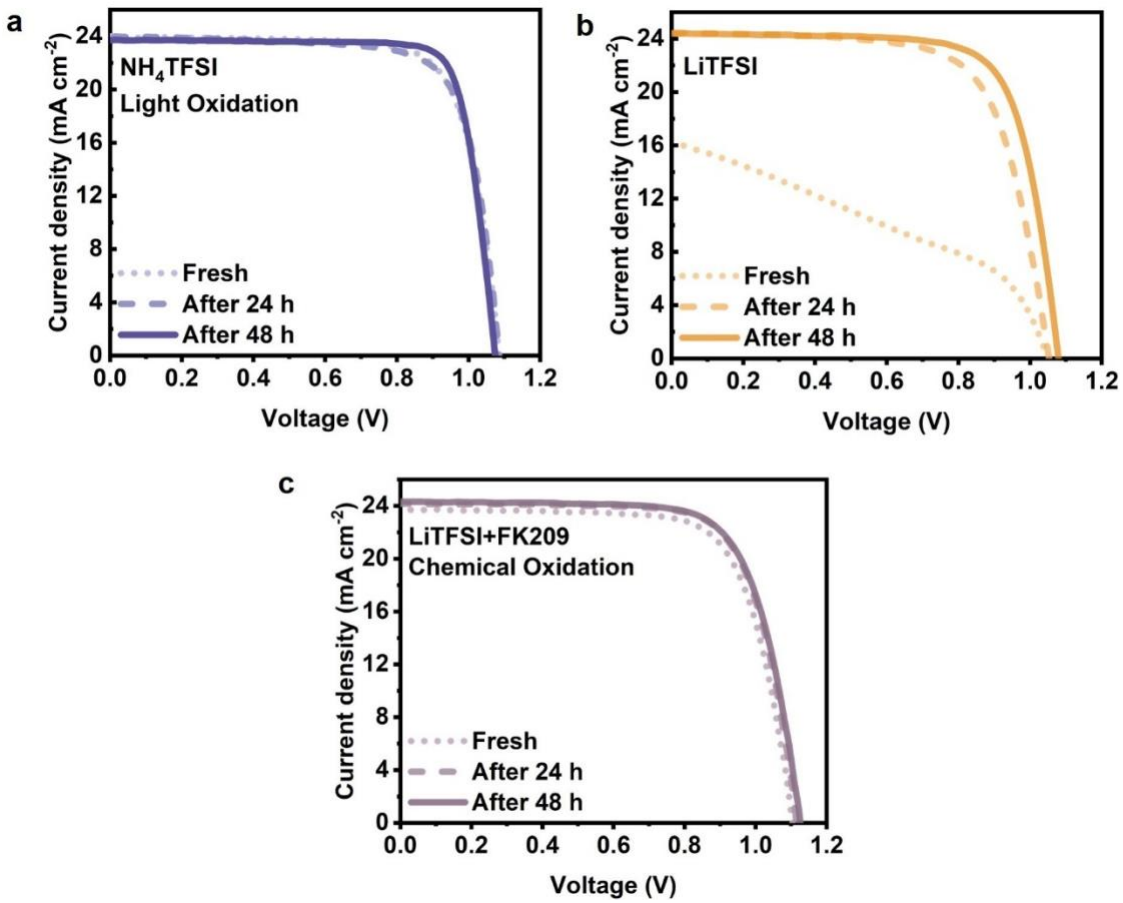

Supplementary Fig. 51. Distinctions between the conventional spiro-HTL and the LODT method. Current density-voltage plots of the PSCs corresponding to **a,** NH_4TFSI as dopant in LODT processed spiro-HTL. **b,** LiTFSI as dopant in conventional spiro-HTL, **c,** LiTFSI and FK209 as dopant in chemically oxidized spiro-HTL.

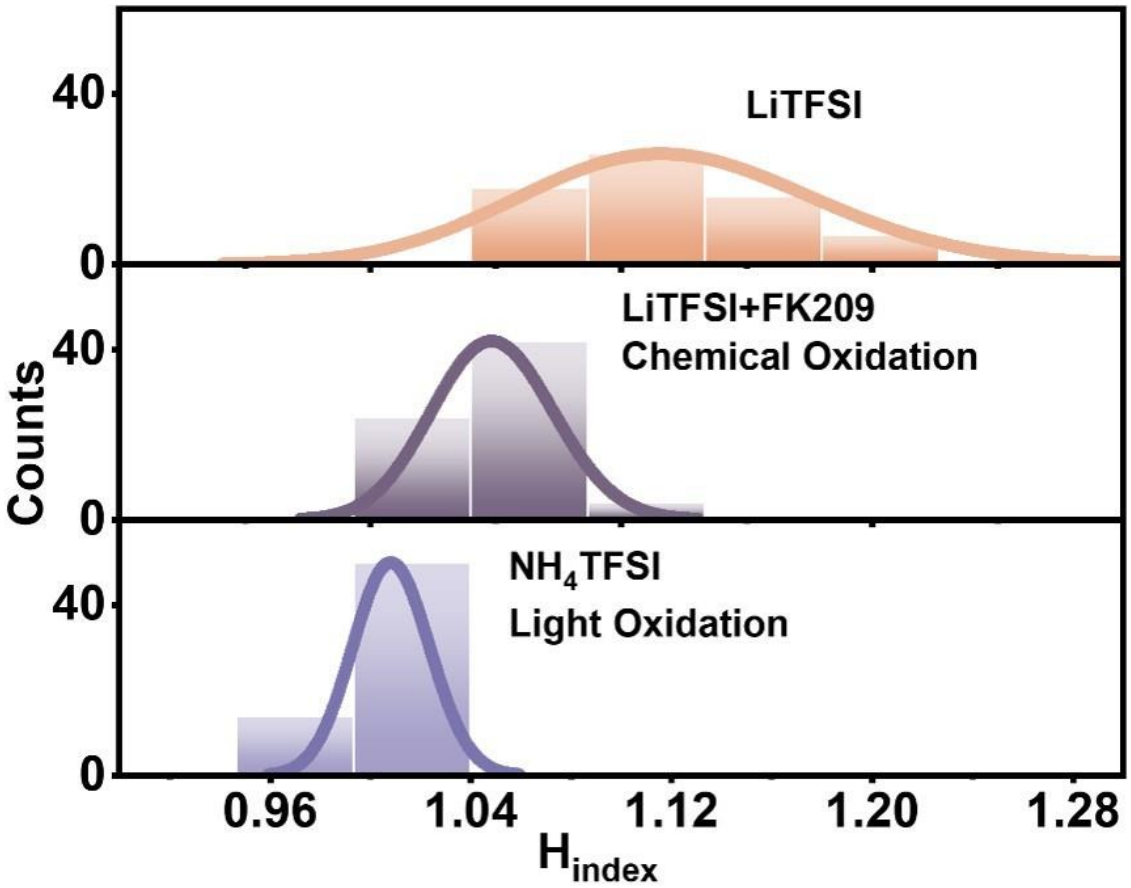

Supplementary Fig. 52. H_{index} based on the devices with different HTLs. Different H_{index} from LiTFSI-based conventional, chemical oxidation, and LODT spiro-HTL methods applied in PSCs.

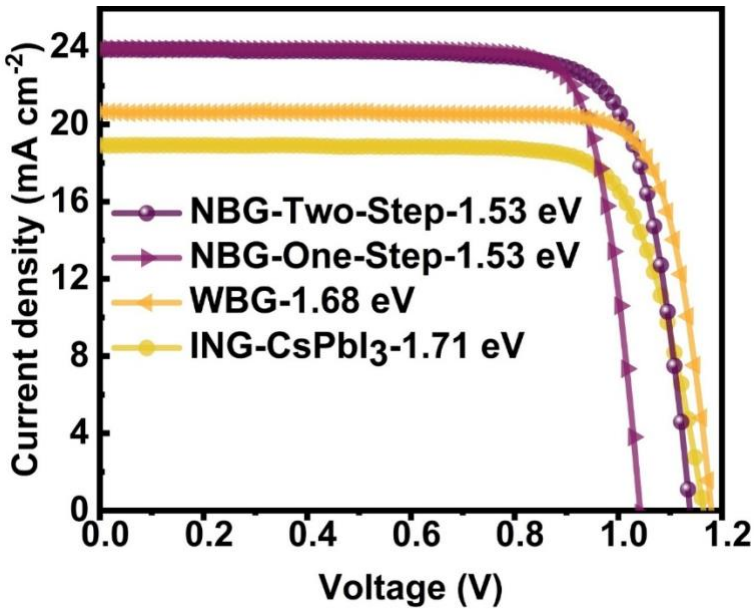

Supplementary Fig. 53. *J-V* plots of the devices corresponding to the optimized LODT conditions applied on different compositions of perovskite layers. Normal bandgap perovskite (NBG) refers to $Cs_{0.1}FA_{0.9}PbI_3$ with E_g = 1.53 eV; Wide bandgap perovskite (WBG) refers to $Cs_{0.125}MA_{0.125}FA_{0.75}Pb(I_{0.833}Br_{0.167})_3$ with E_g = 1.68 eV; Inorganic perovskite solar (ING) refers to $CsPbI_3$ with E_g = 1.71 eV.

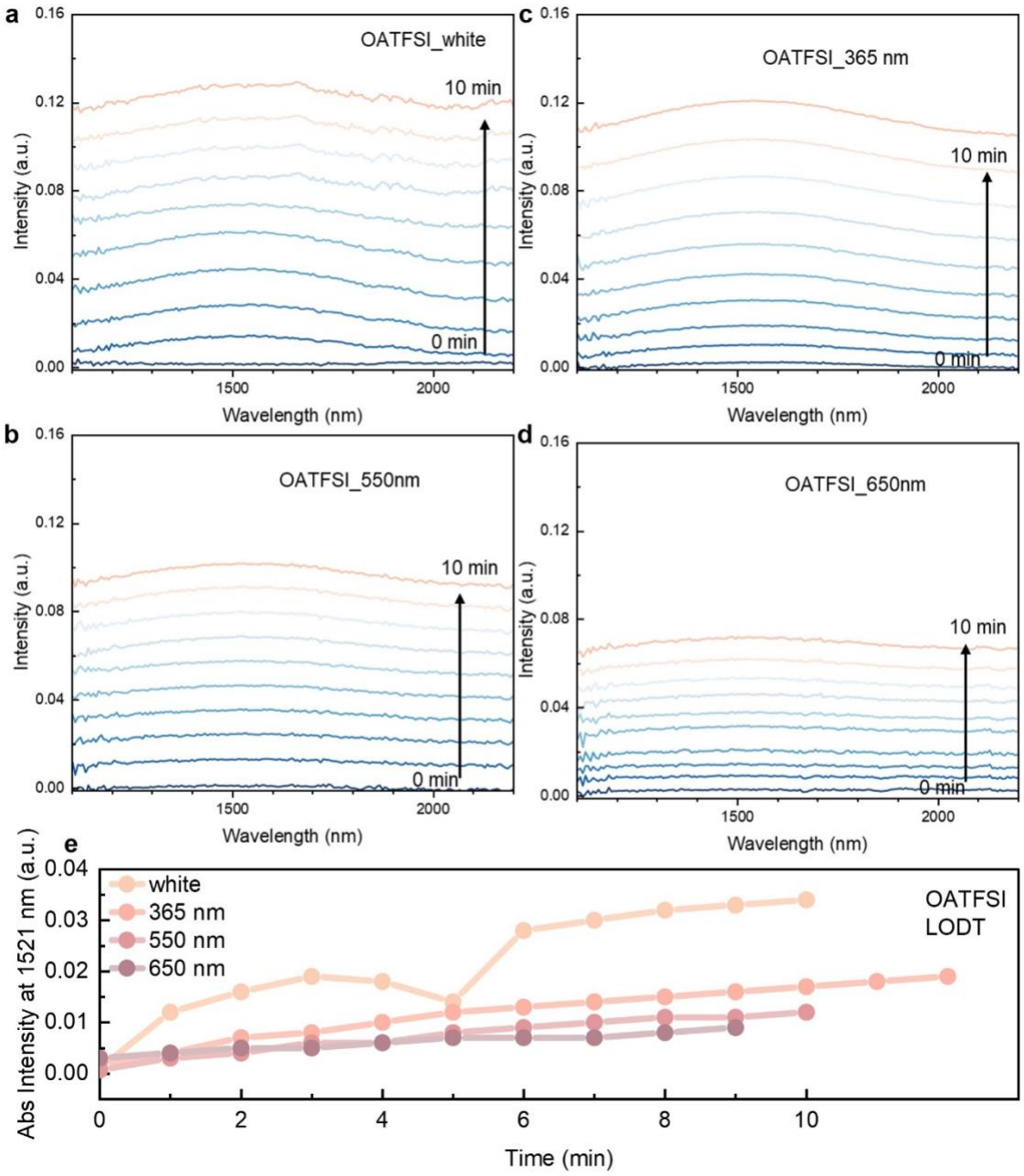

Supplementary Fig. 54. Wavelength-dependent absorbance changes of spiro doped OATFSI. Time-resolved UV-Vis-NIR absorption spectra of the spiro solution doped exclusively with OATFSI, measured under illumination with monochromatic light at various wavelengths of **a,** white, **b,** 365 nm, **c,** 550 nm and **d,** 650 nm. **e,** Absorbance intensity changes at 1521 nm under different light illumination for OATFSI LODT spiro solution.

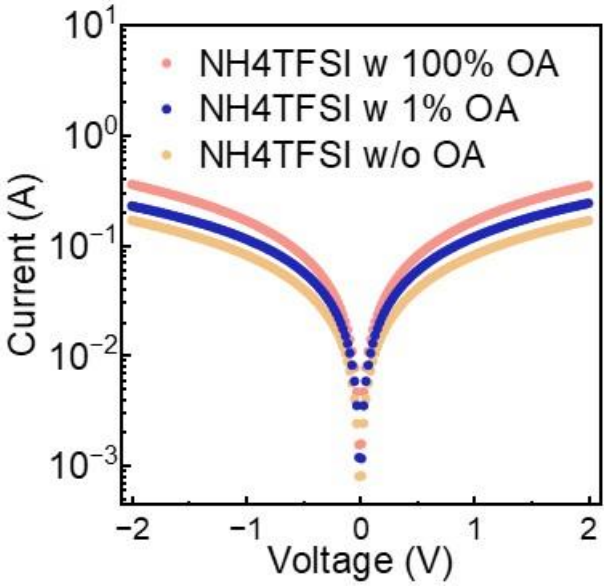

Supplementary Fig. 55. Effect of OATFSI co-doping on the conductivity of LODT-HTL films. Dark current-voltage (*I-V*) characteristics of the LODT-HTL films. The yellow-colored curve represents the control film doped with only NH_4TFSI (w/o OATFSI), while the blue curve represents the film co-doped with both NH_4TFSI and 1% mol OATFSI (w/ 1% OATFSI) and pink for 100% OATFSI doping. Both HTL solutions were prepared in a chlorobenzene solvent with a *t*BP/THF volume ratio of 1. The calculated conductivity is 2.93×10^{-3} S/cm for 1% OATFSI and 3.625×10^{-3} S/cm for 100% OATFSI.

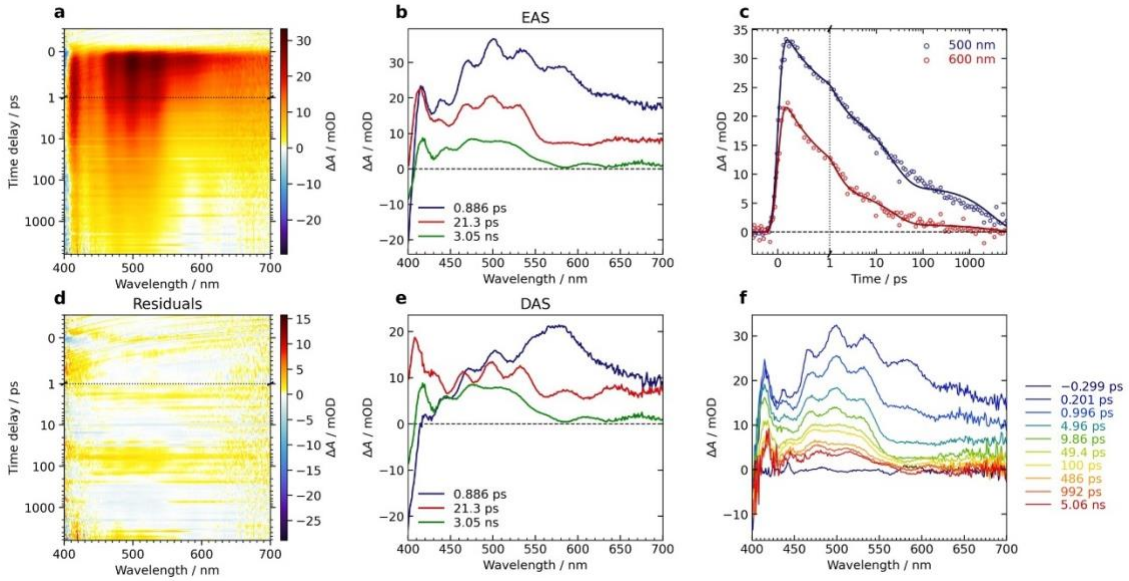

Supplementary Fig. 56. Pump-probe transient absorption spectroscopy (TAS) of co-doped OATFSI in LODT-HTL with NH_4TFSI under excitation with a 350 nm pump pulse. Comprehensive TA data and global analysis for a pristine spiro-OMeTAD film. **a,** Chirp-corrected transient absorption data displayed as contour plots. **b,** Evolution-associated spectra (EAS). **c,** Experimental (circles) and fitted (solid lines) kinetic traces at representative wavelengths. **d,** Residuals matrix from the global fit. **e,** Decay-associated spectra (DAS). **f,** Transient absorption spectra at selected time delays.

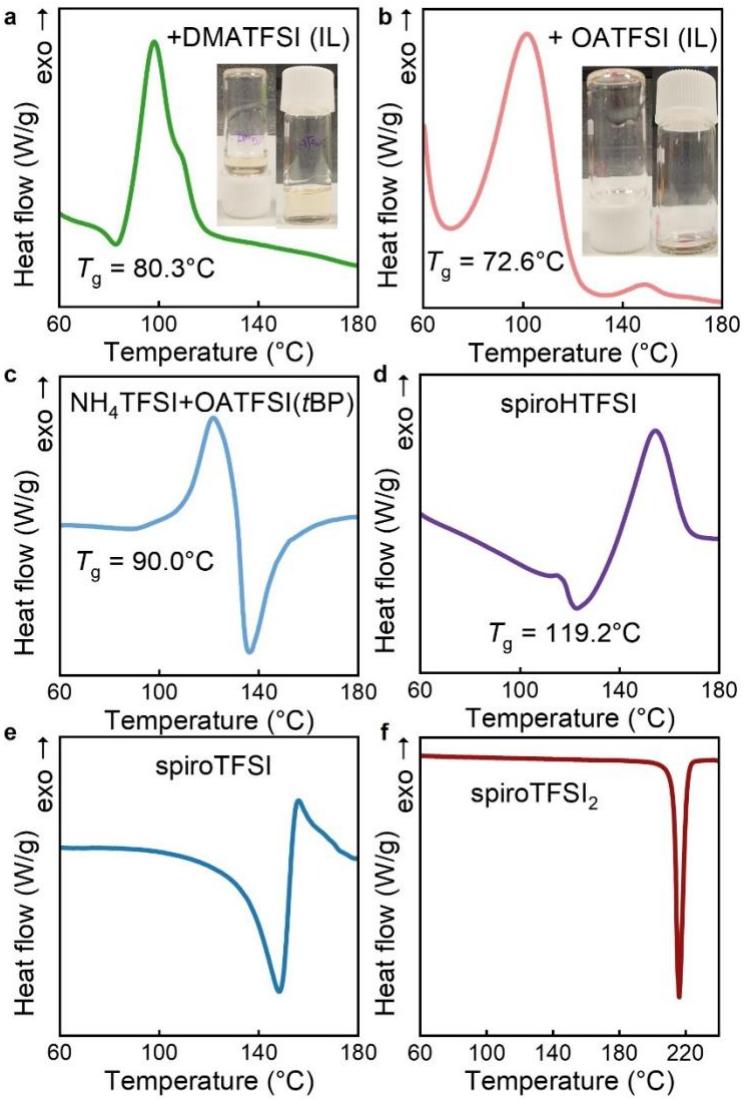

Supplementary Fig. 57. DSC of spiro with various dopants. a, DMATFSI-doped LODT-HTL (T_g = 80.3 °C). The inset shows a photo of liquid DMATFSI. **b,** 100% mol OATFSI-doped LODT-HTL (T_g = 72.6 °C). The inset shows a photo of viscous, oily OATFSI; IL = ionic liquid. **c,** LODT-processed spiro co-doped with NH_4TFSI and 1% mol OATFSI (T_g = 90 °C). **d,** spiro doped with HTFSI (T_g = 119.2 °C). **e,** spiroTFSI, which shows no distinct glass transition. **f,** spiro(TFSI)$_2$, which shows no distinct glass transition or crystallization-induced exothermic features.

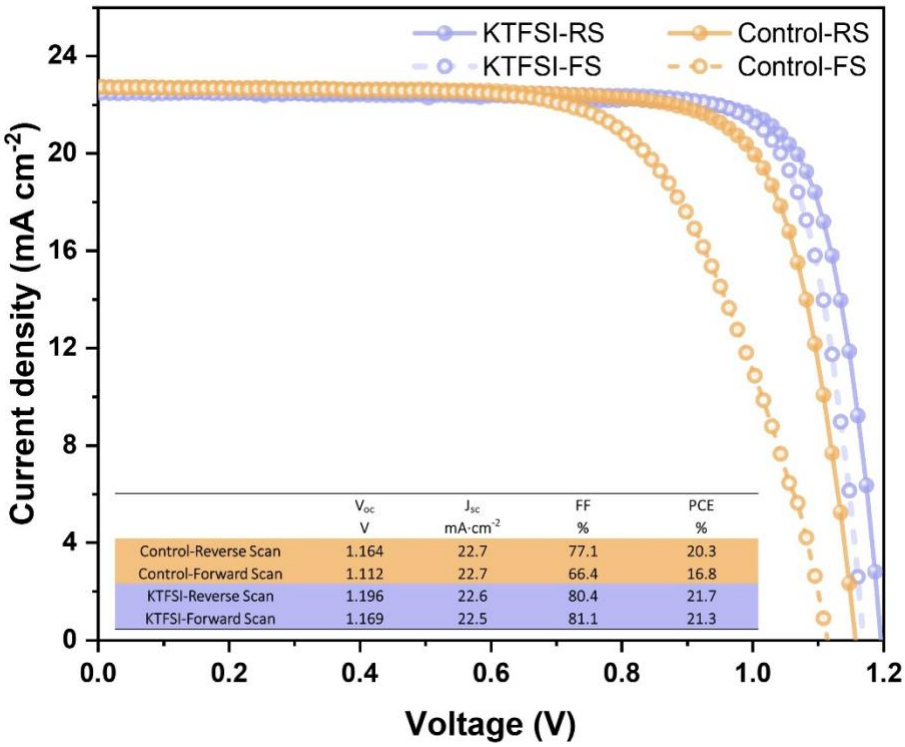

	V_{oc} V	J_{sc} mA·cm^{-2}	FF %	PCE %
Control-Reverse Scan	1.164	22.7	77.1	20.3
Control-Forward Scan	1.112	22.7	66.4	16.8
KTFSI-Reverse Scan	1.196	22.6	80.4	21.7
KTFSI-Forward Scan	1.169	22.5	81.1	21.3

Supplementary Fig. 58. Forward- and reverse-scan *J-V* plots of the best control and KTFSI treated PSCs highlighting the differences in V_{oc} and hysteresis.

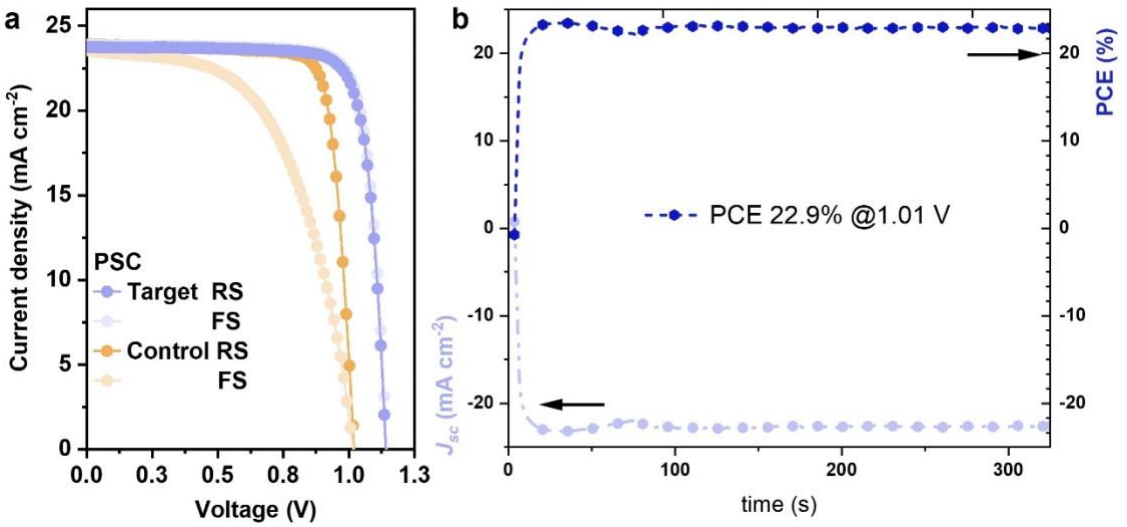

Supplementary Fig. 59. a, *J-V* plots of the champion devices corresponding to the devices based on 0.16 cm^2 PSCs. b, Steady-state power output (SPO) PCE and J_{sc} of the champion device at a bias of 1.01 V for a duration of 320 s.

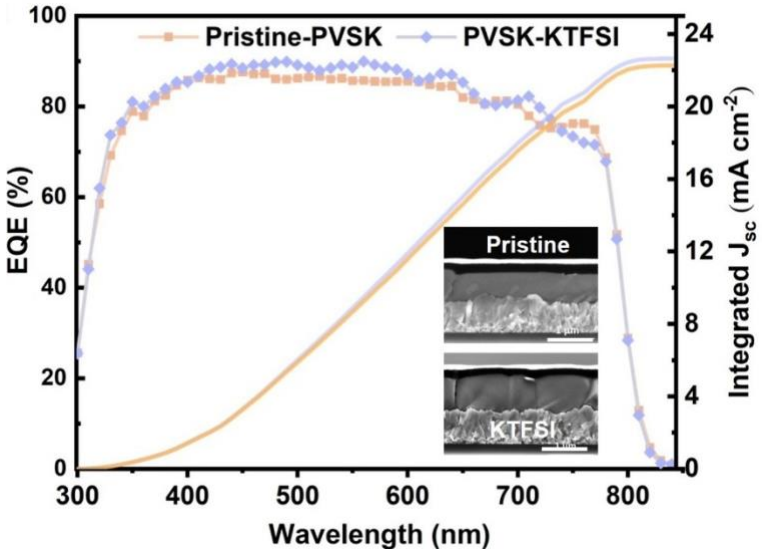

Supplementary Fig. 60. EQE spectra of the perovskite solar cells incorporating the pristine (Control) and KTFSI-PVSK (Target) films. Inset: cross-section view SEM images of the devices from control (top) and KTFSI (bottom) incorporated perovskite films within the FTO/SnO_2/PVSK/spiro-LODT HTL/Au solar cell structure. Scale bar is 1μm.

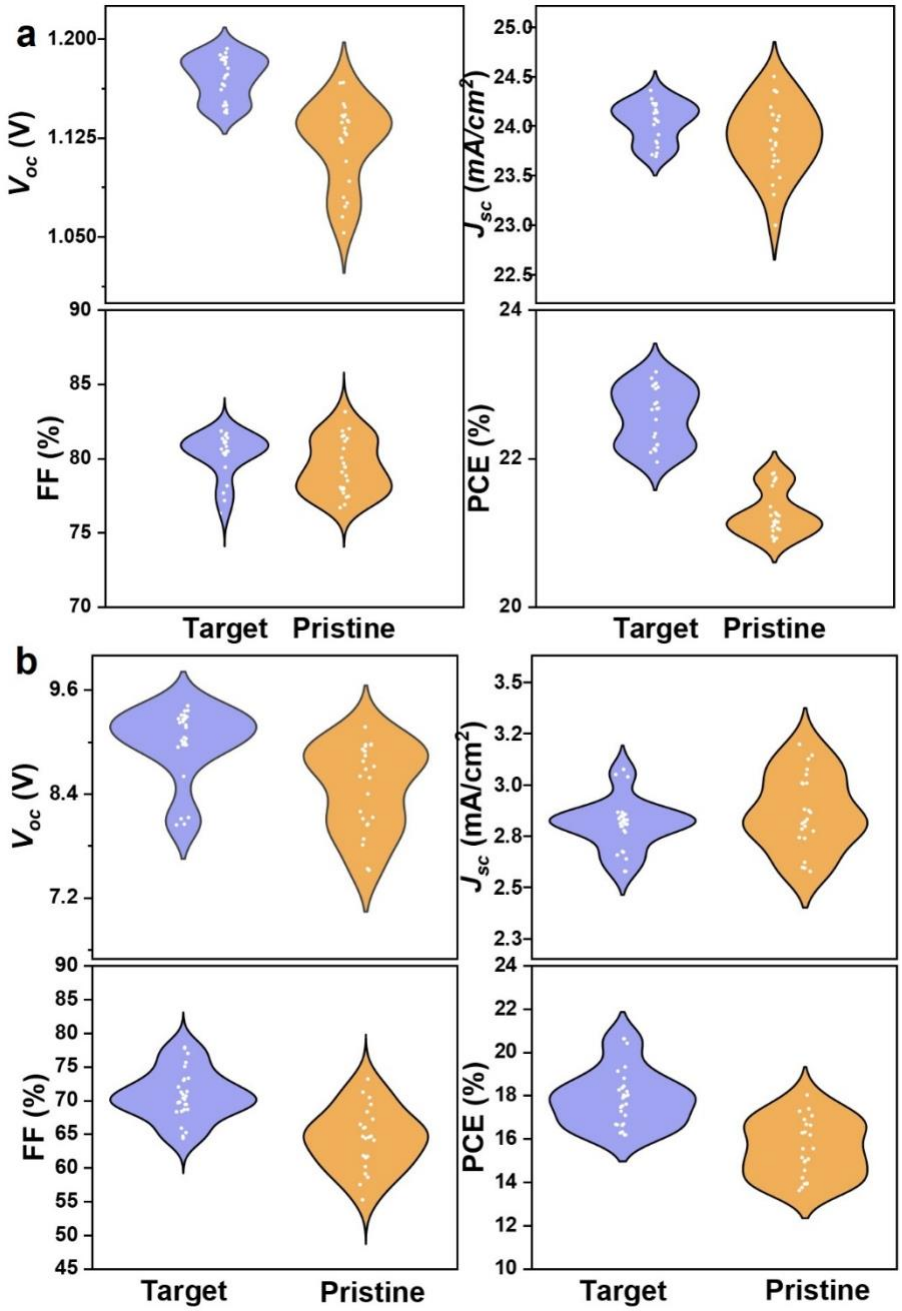

Supplementary Fig. 61. Statistical distribution of FF, PCE, J_{sc} and V_{oc} comparing the target and control PSCs on **a,** 0.16cm^2 active area, **b,** PSM with and an aperture area of 22.08 cm^2.

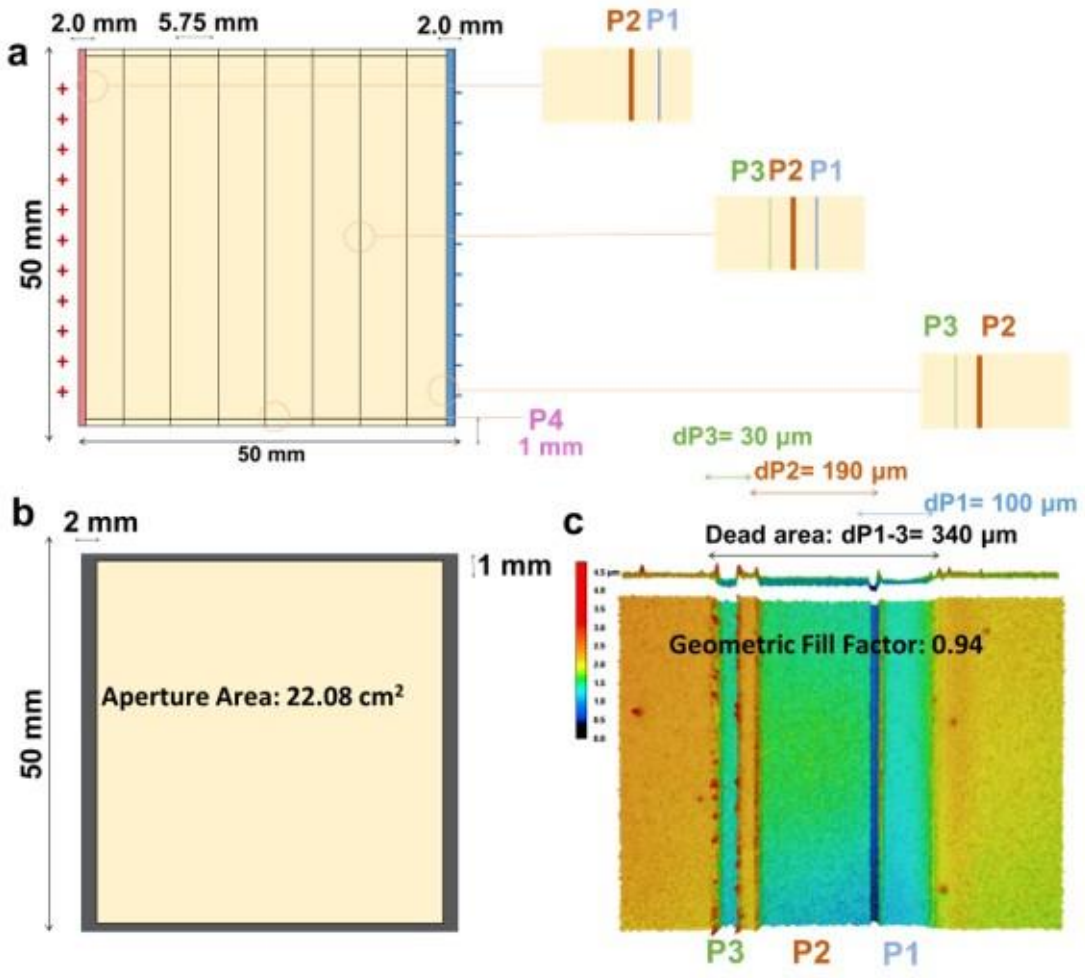

Supplementary Fig. 62. Design, layout, and characterization of the 5 cm × 5 cm PSM. **a,** Schematic of the PSM layout on a 5 cm × 5 cm substrate. The positive and negative electrodes are 2 mm wide, each sub-cell has a width of 5.75 mm, and a 1 mm wide P4 scribe is used for edge isolation after Au deposition. **b,** Diagram of the aperture mask used for device characterization. The frame dimensions correspond to the electrode and P4 scribe widths, defining a final aperture area of 22.08 cm². **c,** 3D pseudo-color image from laser scanning microscopy used to determine the dimensions of the P1, P2, and P3 scribe lines, with color representing surface topography. The total interconnect distance (P1 to P3) is 340 µm, resulting in a calculated geometric fill factor (GFF) of approximately 0.94.

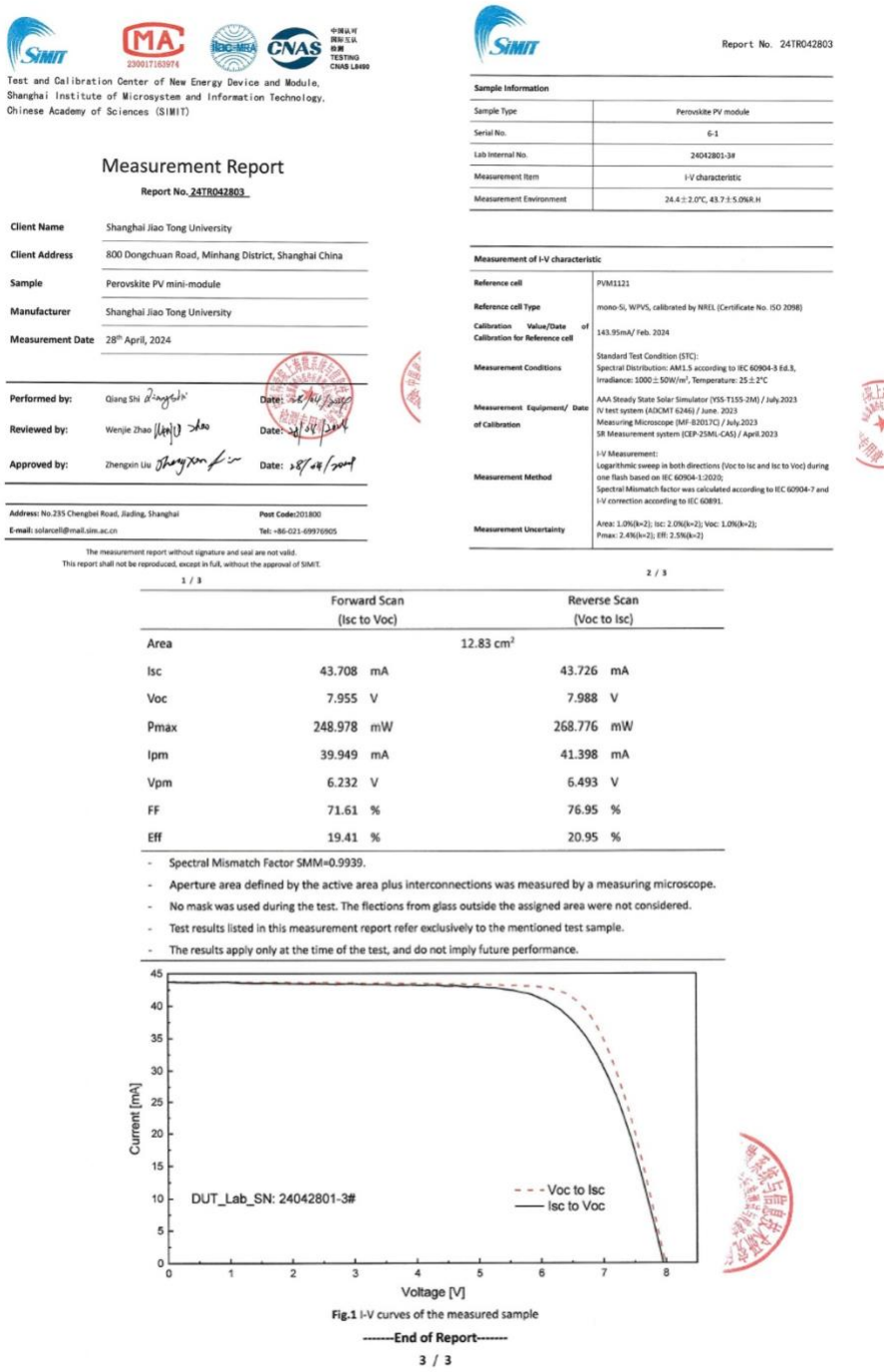

Test and Calibration Center of New Energy Device and Module,
Shanghai Institute of Microsystem and Information Technology,
Chinese Academy of Sciences (SIMIT)

Measurement Report

Report No. 24TR042803

Client Name	Shanghai Jiao Tong University
Client Address	800 Dongchuan Road, Minhang District, Shanghai China
Sample	Perovskite PV mini-module
Manufacturer	Shanghai Jiao Tong University
Measurement Date	28th April, 2024

Performed by:	Qiang Shi	Date:
Reviewed by:	Wenjie Zhao	Date:
Approved by:	Zhengxin Liu	Date:

Address: No.235 Chengbei Road, Jiading, Shanghai Post Code:201800
E-mail: solarcell@mail.sim.ac.cn Tel: +86-021-69976905

The measurement report without signature and seal are not valid.
This report shall not be reproduced, except in full, without the approval of SIMIT.

1 / 3

Report No. 24TR042803

Sample Information

Sample Type	Perovskite PV module
Serial No.	6-1
Lab Internal No.	24042801-3#
Measurement Item	I-V characteristic
Measurement Environment	24.4±2.0℃, 43.7±5.0%R.H

Measurement of I-V characteristic

Reference cell	PVM1121
Reference cell Type	mono-Si, WPVS, calibrated by NREL (Certificate No. ISO 2098)
Calibration Value/Date of Calibration for Reference cell	143.95mA/ Feb. 2024
Measurement Conditions	Standard Test Condition (STC): Spectral Distribution: AM1.5 according to IEC 60904-3 Ed.3, Irradiance: 1000±50W/m², Temperature: 25±2℃
Measurement Equipment/ Date of Calibration	AAA Steady State Solar Simulator (YSS-T15S-2M) / July.2023 IV test system (ADCMT 6246) / June. 2023 Measuring Microscope (MF-B2017C) / July.2023 SR Measurement system (CEP-25ML-CAS) / April.2023
Measurement Method	I-V Measurement: Logarithmic sweep in both directions (Voc to Isc and Isc to Voc) during one flash based on IEC 60904-1:2020; Spectral Mismatch factor was calculated according to IEC 60904-7 and I-V correction according to IEC 60891.
Measurement Uncertainty	Area: 1.0%(k=2); Isc: 2.0%(k=2); Voc: 1.0%(k=2); Pmax: 2.4%(k=2); Eff: 2.5%(k=2)

2 / 3

	Forward Scan (Isc to Voc)		Reverse Scan (Voc to Isc)	
Area	12.83 cm²			
Isc	43.708	mA	43.726	mA
Voc	7.955	V	7.988	V
Pmax	248.978	mW	268.776	mW
Ipm	39.949	mA	41.398	mA
Vpm	6.232	V	6.493	V
FF	71.61	%	76.95	%
Eff	19.41	%	20.95	%

- Spectral Mismatch Factor SMM=0.9939.
- Aperture area defined by the active area plus interconnections was measured by a measuring microscope.
- No mask was used during the test. The flections from glass outside the assigned area were not considered.
- Test results listed in this measurement report refer exclusively to the mentioned test sample.
- The results apply only at the time of the test, and do not imply future performance.

Fig.1 I-V curves of the measured sample

-------End of Report-------

3 / 3

Supplementary Fig. 63. The certification report of PSM with an aperture area of 12.83 cm^2 issued from a third-party independent certification center (Shanghai Institute of Microsystem and Information Technology (SIMIT)). Note: No mask was used for the test, and the aperture area is defined by the active area with P1 and P4 plus interconnections measured by an optical microscope.

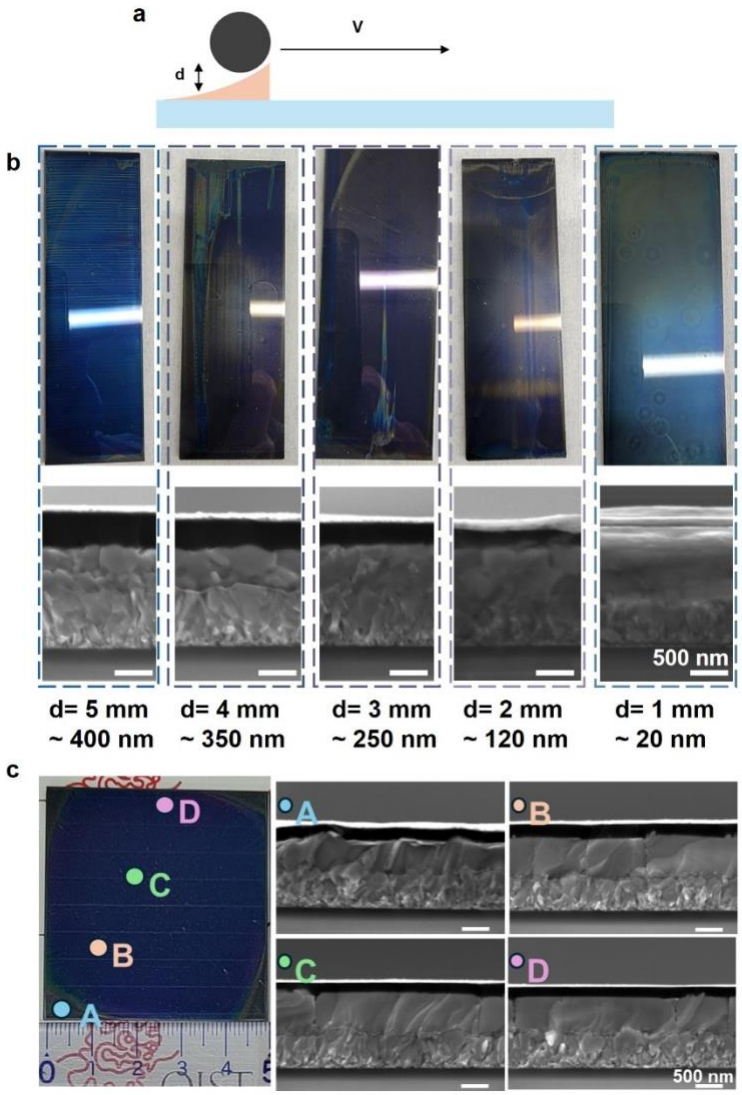

Supplementary Fig. 64. Control of LODT-HTL layer thickness using D-bar coating. **a,** Schematic of the D-bar coating deposition process. The film thickness is controlled by varying the gap distance (*d*) between the blade and the substrate, while the coating speed (*V*) is kept constant at 12 mm/s. **b,** Optical photographs (top row) and cross-sectional SEM images (bottom row) showing the spiro-OMeTAD film thickness as a function of *d*. A gap of 2 mm yields a thickness of ~250 nm, comparable to that from spin-coating (240 nm). **c,** Uniformity assessment of the D-bar coated HTL. Cross-sectional SEM images taken at different points (A, B, C, D) on a 5 cm × 5 cm substrate demonstrate similar film thicknesses. The color variation at the corners of the PSM originates from thickness inhomogeneity caused by the two-step spin-coating deposition of the perovskite layer.

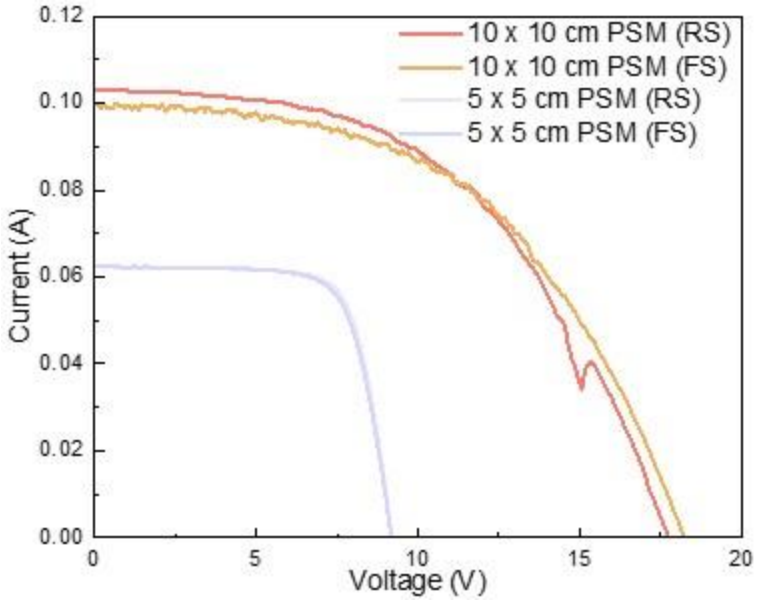

Supplementary Fig. 65. *I-V* curves of the champion devices fabricated *via* D-bar coated PSM. *I-V* characteristics under reverse (RS) and forward (FS) scans for the champion PSM fabricated on 5×5 cm^2 and 10×10 cm^2 substrates, where the HTL was deposited by the D-bar coating method. The aperture areas are 22.08 cm^2 and 82.8 cm^2 for the 5×5 cm^2 and 10×10 cm^2 substrates, respectively.

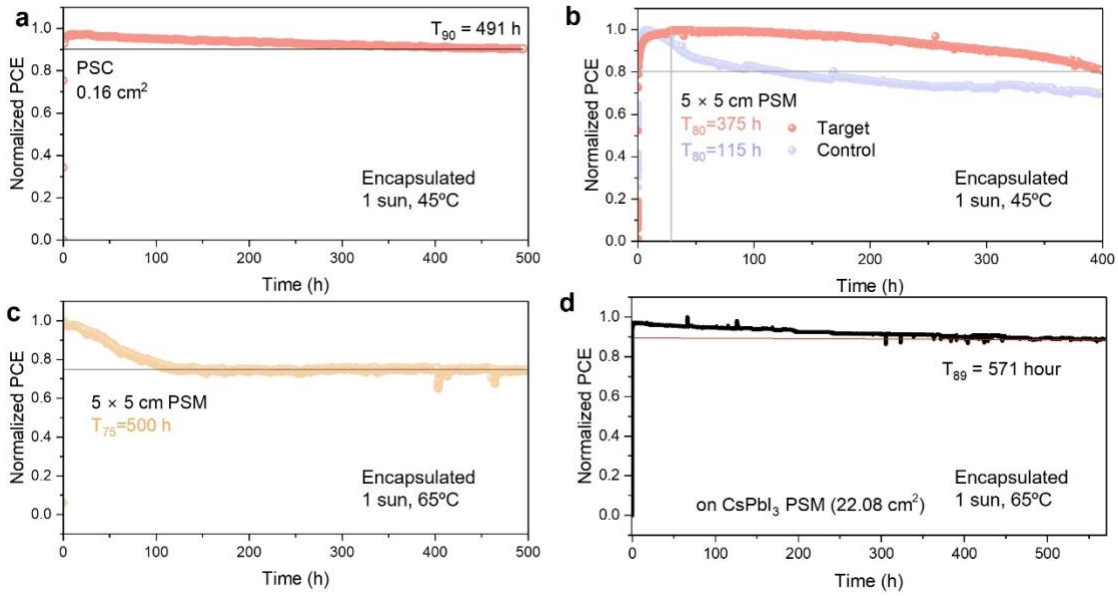

Supplementary Fig. 66. Thermal stability of the perovskite solar cells and module. a, Higher temperature stability of a small-area PSC (encapsulated by UV glue with top glass) under continuous 1-sun illumination at 45 °C. The T_{90} lifetime is 491 hours. **b,** Thermal stability comparison of PSM, control and target from the holistic strategy, tested at 45 °C. The T_{80} lifetimes are 375 hours and 115 hours for the target and control devices, respectively. **c,** Thermal stability of PSM under 65 °C with encapsulation. With T_{75} of 500 hours. **d,** Thermal stability of an encapsulated inorganic $CsPbI_3$-based PSM employing the LODT-HTL, tested at 65 °C. The device exhibits a T_{89} lifetime of 571 hours.

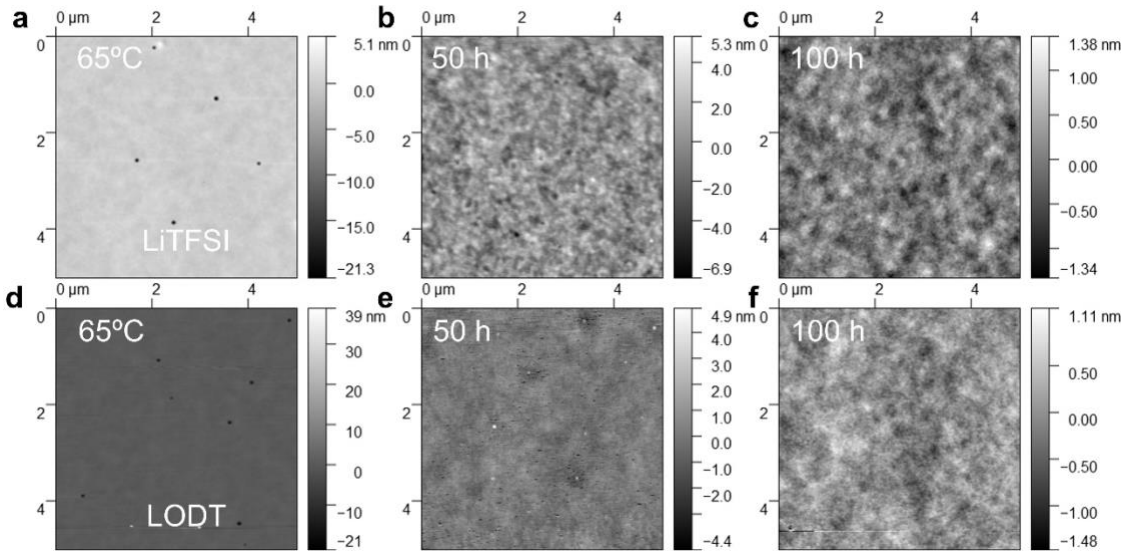

Supplementary Fig. 67. Morphological evolution of the LiTFSI-spiro and LODT-HTL films during thermal aging at 65 °C in air. a,b,c Surface morphology of the LiTFSI-spiro film **a,** before, **b,** after 50 hours annealing and **c,** after 100 hours annealing in air at 65 ºC. The aged film exhibits notable aggregation. **d,e,f,** Surface morphology of the LODT-HTL **d,** before, **e,** after 50 hours annealing and **f,** after 100 hours annealing in air at 65 ºC, showing no significant aggregation of films. Formation of pinholes on the fresh LiTFSI-spiro films have been previously reported.[3]

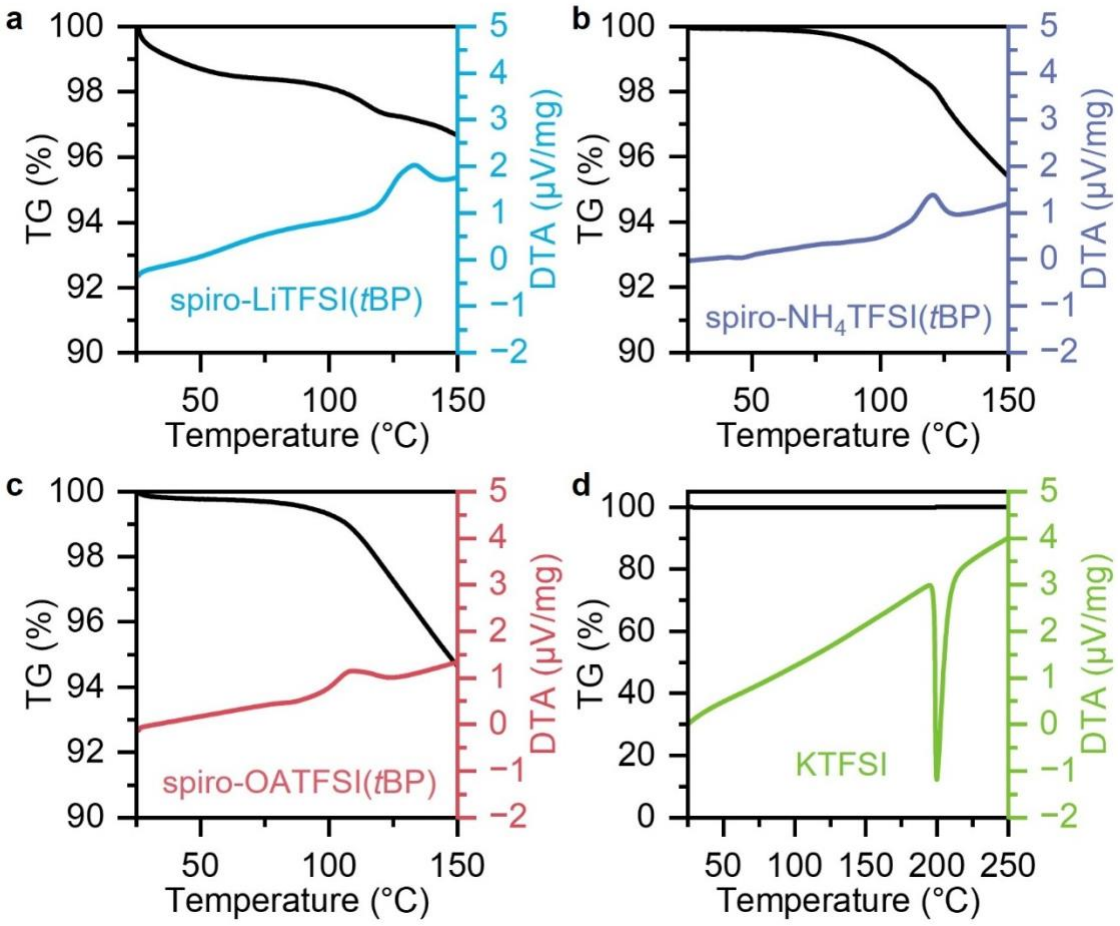

Supplementary Fig. 68. Thermogravimetric and Differential Thermal Analysis (TG-DTA) of various materials. a-c, TG-DTA curves for the spiro-OMeTAD films doped with **a,** LiTFSI + *t*BP, **b,** NH_4TFSI + *t*BP, and **c,** OATFSI + *t*BP. **d,** TG-DTA curve for the KTFSI salt used as the perovskite additive.

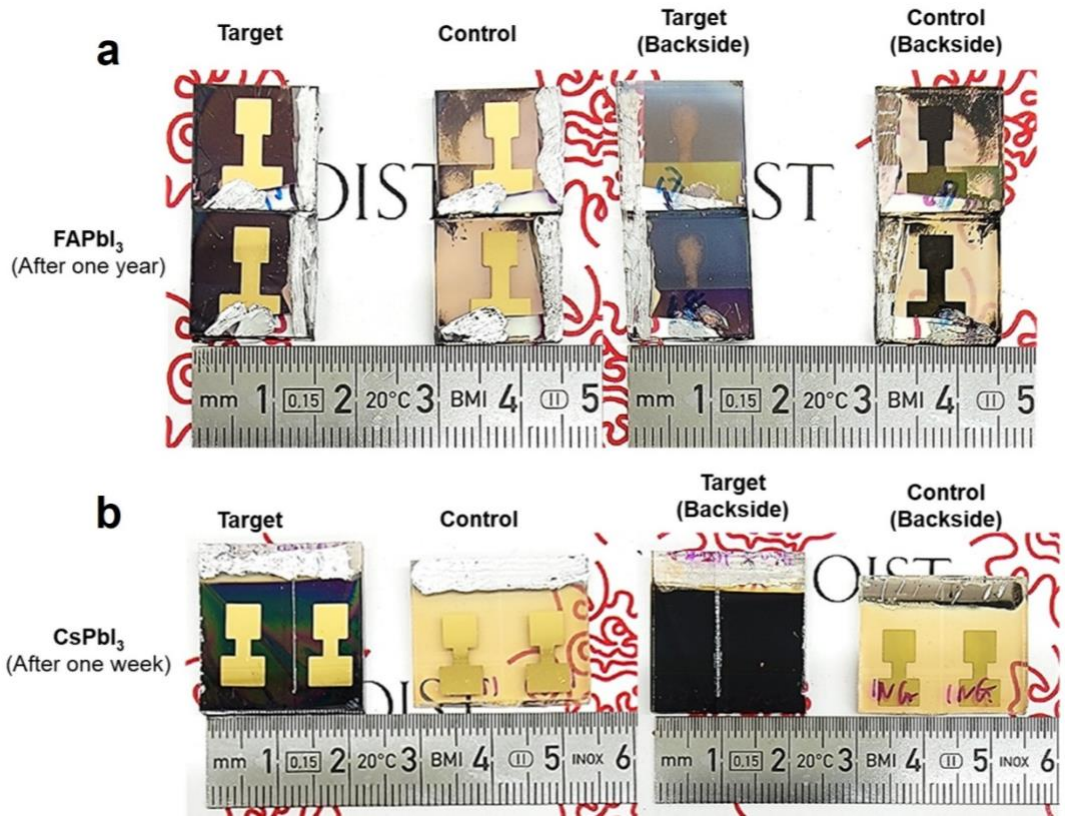

Supplementary Figure 69. Visual comparison of the long-term shelf-life stability of perovskite solar cells. Protective functionality of the OATFSI co-doped spiro-HTL of **a,** $FAPbI_3$ and **b,** $CsPbI_3$ perovskite devices stored for 1 year and 1 week in humid condition (40-50% RH, 25 °C).

Supplementary Table 1. Summary of the Fermi level (E_F), HOMO (E_{HOMO}) level, and energy difference (| E_F–E_{HOMO} |) (w.r.t. E_{vacuum} = 0) for the spiro-HTL films doped with various ATFSI salts.

Condition	E_F (eV) (w.r.t. E_{vacuum})	E_{HOMO} (eV) (w.r.t. E_{vacuum})	| E_F-E_{HOMO} | (eV)
spiro	-3.91	-4.87	0.96
With NH_4TFSI	-4.83	-5.06	0.23
With MATFSI	-4.77	-4.99	0.22
With DMATFSI	-4.43	-4.67	0.24
With TMATFSI	-3.88	-5.34	1.46
With TeMATFSI	-4.95	-6.45	1.50

Supplementary Table 2. Summary of the Fermi level (E_F), HOMO (E_{HOMO}) level, and energy difference (| E_F–E_{HOMO} |) (w.r.t. E_{vacuum} = 0 eV) for the spiro-HTL films doped with various *t*BP ratios in NH_4TFSI doped LODT-HTL.

Condition	E_F (eV) (w.r.t. E_{vacuum})	E_{HOMO} (eV) (w.r.t. E_{vacuum})	| E_F-E_{HOMO} | (eV)
0 *t*BP	-4.83	-5.06	0.23
0.67 *t*BP	-4.90	-5.17	0.27
1 *t*BP	-4.62	-4.94	0.32
10 *t*BP	-4.41	-4.79	0.38
50 *t*BP	-4.41	-4.79	0.38

Supplementary Table 3. Conductivity of the NH_4TFSI-doped LODT-HTL films with different *t*BP concentration. The measurements were conducted on the devices with the structure of FTO/PEDOT:PSS/spiro-OMeTAD/Au. The thickness of the spiro-OMeTAD film was 240 nm, and the electrode area was 0.09 cm^2.

Film	Conductivity ($\times 10^{-3}$ S/cm)
spiro	2.384×10^{-4}
0 *t*BP	1.879
0.67 *t*BP	2.270
1 *t*BP	2.674
10 *t*BP	3.447
50 *t*BP	4.679

Supplementary Table 4. Sheet resistance (R_{sq}) of the NH_4TFSI-doped LODT-HTL films with different *t*BP concentration. The measurements were performed using the four-point probe method on samples with an ITO/spiro-OMeTAD structure. The thicknesses of the spiro-OMeTAD and ITO layers were 240 nm and 60 nm, respectively.

Film	R_{sq} (Ω/□)
ITO	11.947 ± 0.028970
0.67 *t*BP	10963 ± 22.021
1 *t*BP	10936 ± 22.630
10 *t*BP	10881 ± 4.8099
50 *t*BP	10822 ± 19.599

Supplementary Table 5. Comparison of the XRD peak parameters for the pristine and KTFSI-doped perovskite films corresponding to PbI_2 (001) and $FAPbI_3$ (110). The table summarizes the peak intensity, peak area, and FWHM values for the diffraction peaks corresponding to the PbI_2 and the main perovskite phases.

Sample	2-Theta (degree)	Area	FWHM (degree)
Pristine perovskite	12.643	34.5	0.354
	13.945	802.6	0.31
With KTFSI	12.611	71.2	0.214
	13.957	2858.9	0.187

Supplementary Table 6. Fitting parameters for the time-resolved photoluminescence (TRPL) decay curves of different samples. The table lists the fast and slow components (time constants, τ_i, and relative amplitudes, A_i, from the TRPL decay curves). A tri-exponential function[4],[5] was used to fit the decays for perovskite films, while a bi-exponential function was used for the perovskite/HTL.

Sample	A_1	τ_1 (ns)	A_2	τ_2 (ns)	A_3	τ_3 (ns)	τ_{avg} (ns)
PVSK with KI	0.724	113	0.279	423	0.048	1601	659
PVSK with KTFSI	0.582	107	0.344	437	0.106	1317	727
PVSK-KI/Li-HTL	0.93	107	0.158	476	-	-	266
PVSK-KTFSI/Li-HTL	0.813	94	0.227	313	-	-	200
PVSK-KTFSI /mix OATFSI-HTL	0.807	93	0.236	299	-	-	193

Supplementary Table 7. XPS binding energy position of the Pb 4*f* and I 3*d* core levels by different treatments for the pristine perovskite layer.

Sample	Binding Energy (eV)			
	Pb $4f_{5/2}$	Pb $4f_{7/2}$	I $3d_{5/2}$	I $3d_{3/2}$
Pristine	140.2	135.2	619.6	631.06
w/ KTFSI	139.5	134.7	619.46	631
w/ OATFSI	139.6	134.7	619.52	631.01

Supplementary Table 8. Statistical summary of the photovoltaic parameters for devices with varying KTFSI additive concentrations. This table presents a statistical analysis of the open-circuit voltage (V_{OC}), short-circuit current density (J_{SC}), fill factor (FF), and power conversion efficiency (PCE) based on at least 15 devices for each KTFSI concentration. HTL: LiTFSI-spiro.

Concentration	V_{OC} (V)	J_{SC} (mA/cm^2)	FF (%)	PCE (%)
0 mg/mL	1.04±0.03	23.6±0.3	63.8±5.9	16.2±1.7
1 mg/mL	1.13±0.02	23.8±0.4	70.1±4.3	16.8±1.5
3 mg/mL	1.16±0.01	23.9±0.3	80.5±1.1	19.9±1.3
5 mg/mL	1.14±0.01	23.8±0.4	76.7±1.2	17.9±1.3

Supplementary Table 9. Photovoltaic parameters of the champion devices.

Champion Devices	Condition	Scan	V_{OC} (V)	J_{SC} (mA/cm^2)	FF (%)	PCE (%)	PCE H_{index} (RS/FS)
0.16 cm^2 PSC	Target	RS	1.19	23.9	81.1	23	1.009
		FS	1.19	23.7	80.1	22.8	
	Control	RS	1.06	23.9	80.7	20.5	1.454
		FS	1.05	23.6	56.4	14.1	
25 cm^{2}PSM	Target	RS	9.36	2.84	77.8	20.6	1.009
		FS	9.36	2.83	77.0	20.4	
	Control	RS	8.84	2.75	71.7	17.4	1.581
		FS	8.83	2.81	44.0	11	
25 cm^2 PSM (D-bar coating)		RS	9.18	2.82	74.5	19.3	1.021
		FS	9.17	2.83	73.0	18.9	
100 cm^2 PSM (D-bar coating)		RS	18.20	1.13	51.5	12.15	1.038
		FS	17.73	1.17	50.6	11.7	

Supplementary Table 10. Summary of the statistical data of photovoltaic parameters from PSC and PSM devices.

Device	Condition	Scan	V_{OC} (V)	J_{SC} (mA/cm^2)	FF (%)	PCE (%)	PCE H_{index} (RS/FS)
PSC	Target	RS	1.18±0.01	23.6±0.8	79.7±2.4	21.9±0.9	1.017
		FS	1.18±0.01	23.63±0.8	79.7±2.4	21.4±0.8	
	Control	RS	1.07±0.02	23.4±0.7	73.9±4.9	18.8±1.0	1.383
		FS	1.07±0.04	23.4±0.6	52.9±6.2	13.6±1.5	
PSM	Target	RS	9.06±0.44	2.81±0.1	72.6±4.2	18.6±1.5	1.054
		FS	8.96±0.40	2.81±0.1	70.2±3.7	17.7±1.2	
	Control	RS	8.51±0.41	2.82±0.2	67.8±3.0	16.8±0.7	1.558
		FS	8.48±0.59	2.81±0.2	45.6±2.9	10.8±0.5	

Supplementary Table 11. Summary of the recently reported high-performance perovskite solar modules employing LiTFSI-free spiro-OMeTAD modifications. The PCE loss is defined by the equation: PCE Loss=(PCE_{PSM}−PCE_{PSC})/($Area_{PSM}$−$Area_{PSC}$).

Materials	PSC efficiency (certification*)	PSM efficiency (certification*)	PCE Loss (%/cm^2)	PSM Deposition
PI-TFSI	24.85% * 0.062 cm^2	20.71% 15.03 cm^2	-0.277	Sequential deposition[6]
EC	25.51% * 0.080 cm	22.97% * 25 cm^2	-0.0919	Anti-solvent[7]
		21.02% * 100 cm^2	-0.0337	
$FcPF_6$	24.08% * 0.547 cm^2	22.13% 18 cm^2	-0.112	Vacuum-flash[8]
		20.27% 56 cm^2	-0.0687	
$Eu(TFSI)_2$	25.45% 0.05 cm^2	20.35% 18 cm^2	-0.284	Vacuum-flash[9]
NH_4TFSI	23.0% 0.16 cm^2	20.6% 22.08 cm^2	-0.109	Sequential deposition **(This work)**
		20.95% * 12.83 cm^2	-0.161	

Supplementary Table 12. Effect of different additives on the hygroscopicity of solid spiro-OMeTAD. The table summarizes the mass increase of solid spiro-OMeTAD materials, doped with various additives, after 1 hour of exposure to ambient air at room temperature. Relative humidity condition, RH 53%.

Condition: RH 53% 23 °C	LiTFSI	NH_4TFSI	MATFSI	DMATFSI	TriMATFSI	TeMATFSI	OATFSI
Initial Weight (mg)	6.581	8.635	8.231	9.687	7.325	12.412	10.478
After 1 hour (mg)	7.862	8.638	8.237	9.696	7.334	12.418	10.485
Differential (mg)	1.281	0.003	0.006	0.009	0.009	0.006	0.007

Supplementary Table 13. Photovoltaic parameters of the inorganic $CsPbI_3$ PSM fabricated with the LODT-HTL with an aperture area of 22.08 cm^2 in reverse scan.

22.08 cm^2 PSM	Number	V_{OC} (V)	J_{SC} (mA/cm^2)	FF (%)	PCE (%)
LODT-HTL PVSK: $CsPbI_3$	1	9.78	2.31	81.9	18.4
	2	9.43	2.49	78.5	18.4
	3	8.64	2.34	24.0	4.8
	4	9.74	2.32	79.3	17.9
	5	9.62	2.33	79.0	17.7
	6	9.72	2.31	79.4	17.9
	7	9.65	2.29	80.2	17.8
	8	9.73	2.39	79.9	18.6
	9	9.77	2.37	80.3	18.6

Supplementary Table 14. Summary of the recent studies on the use of ATFSI salts as dopants for spiro-OMeTAD hole transport layers. The use of TMATFSI as a dopant has not been previously reported to the best of our knowledge. LODT: Light oxidation doping treatment.

ATFSI additive	LODT	Composition of HTL	Reference
MATFSI	No	6 mg MATFSI/36 μL *t*BP 91.4 mg spiro-OMeTAD	[10]
DMATFSI	No	2% DMATFSI/9.1 mg LiTFSI/28.8 μL *t*BP 75 mg spiro-OMeTAD	[11]
TMATFSI	-	-	-
TeMATFSI	No	6.42 mg TeMATFSI/17 μL *t*BP 43.4 mg spiro-OMeTAD	[12]
OATFSI	No	24 mM OACl/24 mM LiTFSI 70 mM spiro-OMeTAD	[13]

Supplementary Table 15. Cost assessment for the LODT-HTL strategy. The cost analysis is based on publicly available prices for the precursor materials from major commercial chemical suppliers (Tokyo Chemical Industry Co., and Sigma-Aldrich).

Material	Amount	Price (USD/mol)
spiro-OMeTAD	1 mol	199505
NH_4TFSI	15% mol	283
OATFSI	1% mol	361
HTFSI	16% mol	281
NH_4OH	15% mol	2
OA	1%mol	80
*t*BP+THF	10% mol	1914
Total price: 2645 USD/mol or 2 USD/g (If all additives are 100% mol)		

Supplementary Note 1.

In the early stages, the understanding of H^+ induced doping involved the use of HTFSI as additives in the process of spiro oxidation. For example, Snaith and co-workers[14] were the first to describe the doping mechanism of H^+ between the N atom on spiro and the N atom on $TFSI^-$. Because of the strong acidity of HTFSI, $[spiroH]^+TFSI^-$ cannot exist in the solution. H^+ are easily reduced by spiro molecules, leaving 1/2 H_2 and $spiro^+$. Finally, HTFSI are consumed by spiro to become $TFSI^-$ anions and H_2 escaping as gas. The oxidized $spiro^+$ is stabilized by $TFSI^-$ in the end, leading to spiro-TFSI formation. This process needs to be thermally activated. A different scenario exists such that the solution contains free protons, but the concentration of H^+ is not as high as in the strong HTFSI solution. For example, Zhu and co-workers[15], verified that under weak acid conditions, such as in H_3PO_4, HCl, H_2SO_4 and so on, the system cannot provide enough protons during the doping process when reacting with spiro. The observed dark-brownish spiro solution was explained to the H^+ acting as a connecting bridge between the N atom on spiro and the N atom on $TFSI^-$. The new structure is similar to a hydrogen-bond formed in spiro solution. This work is based on the previous studies showing that free protons can initially react with spiro in an acid-based reaction. The source of protons plays a decisive role in determining the stability of HTL. The choice of ATFSIs stems from the fact that the ammonium cation serves as a reservoir of protons, while the dissociated amines can be removed through volatilization or heating.[10] Once spiro binds with proton, the ammonium cation can no longer release additional protons unless the amines are removed from the system or the concentration of spiroHTFSI is reduced. Critically, because spiroHTFSI requires external energy to abstract an electron from spiro-OMeTAD and then be oxidized, light irradiation (as the energy source for excitation) becomes indispensable in this work. Furthermore, the UV-Vis-NIR setup inside the glovebox confirmed that this light-induced oxidation strategy of spiro does not require oxygen, water or *t*BP, underscoring the broader significance of this work.[16] Meanwhile, this study provides light irradiation as a convenient and practical approach for future investigations employing proton-containing ammonium cations as dopants for spiro or other related triarylamine-based p-type materials as listed in **Supplementary Table 14**.

Supplementary References

1 Fantacci, S., De Angelis, F., Nazeeruddin, M. K. & Grätzel, M. Electronic and Optical Properties of the Spiro-Meotad Hole Conductor in Its Neutral and Oxidized Forms: A DFT/TDDFT Investigation. *Journal of Physical Chemistry C* **115**, 23126-23133 (2011) https://doi.org:10.1021/jp207968b

2 Liu, Y., Yang, Z. & Liu, S. F. Recent Progress in Single-Crystalline Perovskite Research Including Crystal Preparation, Property Evaluation, and Applications. *Advanced Science* **5**, 1700471 (2018) https://doi.org:10.1002/advs.201700471

3 Hawash, Z., Ono, L. K., Raga, S. R., Lee, M. V. & Qi, Y. B. Air-Exposure Induced Dopant Redistribution and Energy Level Shifts in Spin-Coated Spiro-Meotad Films. *Chemistry of Materials* **27**, 562-569 (2015) https://doi.org:10.1021/cm504022q

4 Lee, J. H., Kim, T., Song, S. et al. Enhanced Band-Filling Effect in Halide Perovskites Via Hydrophobic Conductive Linkers. *Cell Reports Physical Science* **3**, 2666-3864(2022) https://doi.org:10.1016/j.xcrp.2022.100800

5 Chen, W., Pham, N. D., Wang, H., Jia, B. & Wen, X. Spectroscopic Insight into Efficient and Stable Hole Transfer at the Perovskite/spiro-OMeTAD Interface with Alternative Additives. *ACS Applied Materials & Interfaces* **13**, 5752-5761 (2021) https://doi.org:10.1021/acsami.0c19111

6 Yang, H., Xu, T., Chen, W. et al. Iodonium Initiators: Paving the Air-Free Oxidation of spiro-OMeTAD for Efficient and Stable Perovskite Solar Cells. *Angewandte Chemie International Edition* **63**, e202316183 (2024) https://doi.org:10.1002/anie.202316183

7 Shin, Y. S., Lee, J., Lee, D. G. et al. Damp-Heat Stable and Efficient Perovskite Solar Cells and Mini-Modules with a *t*BP-Free Hole-Transporting Layer. *Energy & Environmental Science* **18**, 3269-3277 (2025) https://doi.org:10.1039/d4ee05699j

8 Chang, Q., Yun, Y., Cao, K. et al. Highly Efficient and Stable Perovskite Solar Modules Based on Fcpf6 Engineered spiro-OMeTAD Hole Transporting Layer. *Advanced Materials* **36**, e2406296 (2024) https://doi.org:10.1002/adma.202406296

9 Ye, L., Wu, J., Catalan-Gomez, S. et al. Superoxide Radical Derived Metal-Free spiro-OMeTAD for Highly Stable Perovskite Solar Cells. *Nature Communications* **15**, 7889 (2024) https://doi.org:10.1038/s41467-024-52199-4

10 Zhao, J. Z., Cao, J. P., Dong, J. J. et al. Impact of Lithium Dopants in Hole-Transporting Layers on Perovskite Solar Cell Stability under Day-Night Cycling. *Nature Energy* (2025) https://doi.org:10.1038/s41560-025-01856-z

11 Cao, F., Zhu, Z., Zhang, C. et al. Synergistic Ionic Liquid in Hole Transport Layers for Highly Stable and Efficient Perovskite Solar Cells. *Small* **19**, e2207784 (2023) https://doi.org:10.1002/smll.202207784

12 Jung, S. K., Park, K., Lee, J. H. et al. Exploiting an Interfacial Reaction in Perovskite Solar Cells: Quaternary Alkylammonium Ionic Salt Dopants for spiro-OMeTAD. *Advanced Energy Materials* **15** (2025) https://doi.org:10.1002/aenm.202402144

13 Nishimura, N., Kanda, H. & Murakami, T. N. Direct Ion-Exchange Method for Preparing a Solution Allowing Spontaneous Perovskite Passivation via Hole Transport Material Deposition. *ACS Applied Energy Materials* **7**, 7687-7692 (2024) https://doi.org:10.1021/acsaem.4c01314

14 Abate, A., Hollman, D. J., Teuscher, J. et al. Protic Ionic Liquids as P-Dopant for Organic Hole Transporting Materials and Their Application in High Efficiency Hybrid Solar Cells. *Journal of the American Chemical Society* **135**, 13538-13548 (2013) https://doi.org:10.1021/ja406230f

15 Li, Z., Tinkham, J., Schulz, P. et al. Acid Additives Enhancing the Conductivity of spiro-OMeTAD toward High-Efficiency and Hysteresis-Less Planar Perovskite Solar Cells. *Advanced Energy Materials* **7**, 1601451 (2017) https://doi.org:10.1002/aenm.201601451

16 Shin, Y. S., Song, J. W., Lee, D. G. et al. De-Doping Engineering for Efficient and Heat-Stable Perovskite Solar Cells. *Joule* **9**, 2542-4351 (2025) https://doi.org/10.1016/j.joule.2024.10.011